Kinematic Clues to the Formation and Evolution of Galaxies

A thesis presented

by

Sheila Jane Kannappan

to

The Department of Physics

in partial fulfillment of the requirements
for the degree of
Doctor of Philosophy
in the subject of
Physics

Harvard University
Cambridge, Massachusetts

May 2001

© 2001 by Sheila Kannappan

All Rights Reserved

To my mother, for her love of science and the curiosity she awakened in me

Kinematic Clues to the Formation and Evolution of Galaxies

Advisor: Daniel Fabricant

Author: Sheila Jane Kannappan

Abstract

This work investigates clues to galaxy evolution in the internal gas and stellar kinematics of ∼200 nearby galaxies, representing all morphological types and spanning luminosities from $M_B = -23$ to -15. The frequency and morphology distribution of galaxies with counterrotating gas and stars provides fossil evidence for past interactions and mergers in the E/S0 galaxy population. The abundance of faint S0 counterrotators and the possible detection of a Magellanic irregular counterrotator suggest that disk galaxies may sometimes arise from mergers between dwarf galaxies. Large rotation curve asymmetries are also common for dwarf E/S0 and dwarf late-type galaxies. Both gas-stellar counterrotation and large rotation curve asymmetries are rare for spiral galaxies.

Residuals from the Tully-Fisher (TF) relation in optical wavelength bands correlate with the evolutionary states of galaxies. For spirals brighter than $M_R^i = -18$, strong correlations between TF residuals and both $B-R$ color and Hα emission line strength make it possible to reduce the scatter in the TF relation to approximately the level of measurement errors. Sa galaxies and spirals with morphological peculiarities drive the extremes of these correlations, although they are continuous for all spirals. The slope of the color-TF residual correlation is steeper than expected from quiescently evolving disk galaxy models, which may indicate that large starbursts, e.g. those driven by interactions or minor mergers, play a significant role in the star formation histories of some spiral galaxies. Dwarf galaxies do not follow the same TF residual correlations. However, dwarfs with positive and negative TF residuals have distinct physical properties. Relatively overluminous dwarfs appear disturbed, with high rotation curve asymmetry and short gas consumption timescale, while underluminous dwarfs appear to be passively evolving. Due to this split in properties, the slope of the TF relation at low luminosities varies as a function of sample selection and environment.

Finally, a recalibration of the intermediate-redshift Tully-Fisher relation indicates only modest, if any, luminosity evolution relative to the present epoch. A better analysis will require a statistically representative intermediate-redshift sample analogous to the low-redshift survey presented here.

Contents

Abstract v

Acknowledgements xi

Preface xiii

1 Introduction **1**

1.1 The Nearby Field Galaxy Survey 2

1.2 The Kinematic Data 3

1.3 Research Approach 5

1.4 Summary of Results 6

1.5 Future Work 7

2 Counterrotating Gas and Stars **9**

2.1 Introduction 10

2.2 Data & Methods 11

2.2.1 Sample 11

2.2.2 Observations & Data Reduction 13

2.2.3 Identification of Gas-Stellar Counterrotators 14

2.3 Results & Discussion 16

2.3.1 Individual Counterrotators 16

2.3.2 Statistics 18

2.3.3 Formation Mechanisms 21

2.4 Conclusions 25
2.5 Appendix: Frequency of Gas-Stellar Counterrotation 27
2.5.1 Abstract 27
2.5.2 Sample 27
2.5.3 Results 27
2.5.4 Discussion 27

3 Rotation Curve Asymmetries **31**
3.1 Introduction 32
3.2 Asymmetry Measurement Technique 32
3.3 Results 33

4 Physical Sources of Scatter in the Tully-Fisher Relation **39**
4.1 Introduction 40
4.2 The Nearby Field Galaxy Survey 42
4.3 Velocity Width Data 44
4.3.1 Optical Rotation Curve Observations 44
4.3.2 Rotation Curve Asymmetry Measurements 47
4.3.3 Velocity Width Definitions & Optical-To-Radio Conversions . 48
4.3.4 Velocity Width Corrections & Errors 52
4.4 Luminosity Data 53
4.4.1 Absolute Magnitudes 54
4.4.2 Internal Extinction Corrections 54
4.5 Fitting Technique 55
4.6 The Spiral TFR 1: Basic Calibration & Literature Comparison 57
4.6.1 Field Galaxy Samples 57
4.6.2 Cluster Samples 61
4.7 The Spiral TFR 2: Sa & Peculiar Galaxies 64

4.7.1 An Sa Galaxy Offset 64
4.7.2 Galaxy Peculiarity and Sample Pruning 66
4.8 The Spiral TFR 3: Third Parameters & Physical Sources of Scatter . 69
4.8.1 Third Parameter Analysis Technique 69
4.8.2 Third Parameter Test Results 73
4.8.3 What Causes Offsets from the Spiral TFR? 81
4.9 The TFR for the General Galaxy Population 84
4.9.1 Physical Sources of Scatter in a Morphology-Blind TFR: The Trouble with Emission-Line S0's 87
4.9.2 Physical Sources of Scatter in the Dwarf Extension of the TFR 89
4.9.3 Two Dwarf Galaxy Populations and the Slope of the TFR . . 94
4.10 Conclusions 98

5 Calibrating Evolution in the Tully-Fisher Relation 101
5.1 Introduction 102
5.2 Recalibrating the Intermediate-Redshift TFR 103
5.2.1 The Vogt et al. Sample 105
5.2.2 The Simard & Pritchet Sample 106
5.3 A Low-Redshift Reference Calibration 110
5.4 Discussion 112

A Building a Spectrograph for Educational or Amateur Astronomy 113
A.1 Introduction 114
A.2 Optimizing the Optical Design 115
A.2.1 Layout of a Generic Spectrograph 115
A.2.2 Sampling and the Relative Scaling of the System 117
A.3 IntroSpec 121
A.3.1 General Overview of the Instrument 121

A.3.2 Working With Fibers 127
A.3.3 The Manual Guider 129
A.4 Conclusion 130

References **135**

Acknowledgements

I thank Daniel Fabricant for helping me to make my dreams come true. With patience and a gift for teaching, Dan has guided me in my transformation from novice to professional astronomer, training me in every scientific skill from basic data reduction to how to write a good research proposal to principles of instrument design. I am grateful to Dan for giving me the freedom to pursue my own insights and interests, while at the same time holding me to high standards of rigorous thought and careful expression. At a personal level, Dan has earned my deepest respect and affection for his integrity both as a scientist and as a human being. I hope that I may live up to his example in my own career.

The bulk of the research presented here was conducted in collaboration with the Nearby Field Galaxy Survey team: Rolf Jansen, Marijn Franx, Nelson Caldwell, Dan, and myself. I thank the team for shared data, expertise, and friendship, and I especially thank Rolf for cheerfully answering all of my questions over the years, however elementary. Betsy Barton and Mike Pahre have also collaborated on related projects with me, which do not appear in this thesis but have helped to shape my scientific personality. I would also like to acknowledge all those who have observed for me and with me at Mt. Hopkins: Dan, Perry Berlind, Zoltan Balog, Barbara Carter, Lauren Hough, Natasha Lepore, and Jennifer Weinberg-Wolf. Our adventures fighting furry bugs, turning potatoes into charcoal, and chasing the telescope dome around in circles will not be soon forgotten.

The Appendix of this thesis describes a project from my other area of doctoral research, astronomical instrumentation. When I began working with Dan, I had hardly set foot in a lab, and Dan ingeniously conceived the perfect training project: IntroSpec, an educational spectrograph for the Harvard Astronomy Department. I owe my success in building the instrument to the patient mentorship of Dan and Charlie Hughes, machinist-magician and very dear friend. I would also like to thank John Huchra for the opportunity to work with the NGST Near-IR Spectroscopy Panel, my first introduction to the science and politics of NASA instrument design, and for looking out for me *in loco advisoris* on several occasions.

Many others have aided my dissertation work in specific ways which are acknowledged in the individual chapters. More generally, I would like to acknowledge my committee (Paul Horowitz, Bob Kirshner, and Giovanni Fazio), the staff in the OIR division, especially Katie Lynn, Doug Mink, and Susan Tokarz, the amazingly helpful people at Wolbach Library and at the CfA Computation Facility, and the Mt. Hopkins day crew, who fixed every problem with a smile and the occasional gift of a dead bug. Dan Reisenfeld and Pauline Barmby provided essential LaTeX/BibTeX expertise, and John Huchra, Massimo Marengo, Barbara Carter, Warren Brown, and Jonathan McDowell helped me to prepare for my defense. I also thank Bob Collins and Diane Sheehan, RSI therapists extraordinaire, for literally making it possible for me to type this thesis.

Graduate school has been a roller coaster for me, and I am grateful to the friends and colleagues who have kept my heart and soul together through all the ups and downs: my officemates in D-16, especially Kristin Nelson-Patel; the many talented and supportive women I have known over the years through the Women in Physics Study Night; Dave Latham and the rest of the crew at Dave's not-quite-weekly wine tastings; and my close personal friends, particularly Dan Reisenfeld, Daphna Enzer, Neepa Maitra, and Chris Woodward, who never stopped cheering for me. I thank my family for their love and faith in me throughout this long journey — especially my sister Maryann for her support at a time when life has not been easy for either of us, and my mother for her conviction that I was wonderful no matter what happened. During my time in graduate school I lost two beloved family members — my dog of 15 years, who knew me better than most humans do, and my nephew of 19 years, with whom I was struggling to connect. I never knew that the hardest sacrifice of this thesis would be the time I didn't spend with them.

Somewhere beyond colleague or friend or even family is my husband, Douglas Mar. Doug is in every page of this thesis: in ideas clarified through talking with him, in words I could type only because he massaged away the RSI pain, in time spent working while he generously cooked and cleaned, and in creativity set free by his confidence in me. I cannot begin to express my gratitude for twelve years of love, partnership, and intellectual challenge. *All that I am, and the best that I can become....*

Preface

The image of a galaxy is like the face of a person: its surface appearance hides a rich inner life, shaped by all the events of its formative years. The internal motions of galaxies — their kinematics — offer a window into this inner life. Kinematics provide clues to how a system is dynamically supported against gravity, whether it is in equilibrium, and how much invisible dark matter it contains. The most basic observable property of a galaxy — its mass — is encoded in the speeds with which its gas and stars move about the galaxy center. Comparing the rotational and randomly directed motions of the gas and stars reveals the dynamical relationship between these two components and whether they have a common origin.

This thesis is an exploration of the life stories of galaxies as told by their gas and stellar kinematics. In an era when giant telescopes and deep surveys target ever more distant galaxies, the present study shows that much can still be learned in our own cosmic backyard with a small but carefully crafted data set acquired with a 60-inch telescope. Using gas and stellar kinematic data for a sample of 200 galaxies that represent the full variety of the local universe from bright elliptical galaxies to faint dwarf irregular systems, I examine how the broad processes of galaxy formation are written into the quirks of individual galaxies — asymmetric motions, counterrotating gas and stars, and deviations from the standard correlation between luminosity and rotation velocity (the Tully-Fisher relation). The distribution of these irregularities in the galaxy population offers insight into the mechanisms of galaxy evolution.

Galaxies transform both through internally driven processes and through interactions with gas and other galaxies nearby. Beyond all the specific analyses and conclusions presented in the pages to come, perhaps the single most important result of this work is simply this: the fireworks of galaxy evolution — flyby interactions, large galaxies swallowing small satellites, and major galaxy-galaxy collisions — are neither rare, nor confined to "abnormal" systems. While any one observation cannot clinch the case, the possibility and indeed strong plausibility of galaxy interactions and mergers recurs as a constant leitmotif in explaining the properties of systems ranging from irregular dwarfs to giant spirals. Even smooth and apparently undis-

turbed elliptical and lenticular galaxies often harbor kinematic traces of a violent past. The survey described here is uniquely well suited to revealing how the life stories of these individual galaxies are embedded in the shared history of a collectively evolving population.

Chapter 1

Introduction

Our current understanding of galaxy evolution is a bit like the proverbial blind men's understanding of the elephant. Based on the regular structure of our own Milky Way, Eggen et al. (1962) proposed the classic isolated collapse scenario for primordial disk galaxy formation. Based on the extreme distortions of systems like the Antennae, Toomre & Toomre (1972) emphasized the role of galaxy collisions. Recent work on galaxies of all shapes and sizes has left us with a model for everything: secular evolution via bar and spiral arm instabilities (Lin & Shu, 1964), supernova feedback and gas blowout in small galaxies (Wyse & Silk, 1985), transformation of merged galaxies into smooth ellipticals by violent relaxation (Lynden-Bell, 1967; Schweizer & Seitzer, 1992), bulge building through minor mergers or tidally-induced gas inflow (Mihos & Hernquist, 1994; Barton et al., 2000b), bulge building through secular inflow of disk material (Pfenniger & Norman, 1990), giant galaxy formation through mergers of primordial dwarfs (Lacey & Cole, 1993), dwarf galaxy formation in the tidal tails of giant galaxy mergers (Mirabel et al., 1992), and finally S0 formation by a host of mechanisms ranging from ram-pressure stripping to cluster tidal field interactions to minor mergers (Gunn & Gott, 1972; Moore et al., 1998; Bekki, 1998; Kannappan & Fabricant, 2001a).

The challenge for modern studies of galaxy evolution is to put all of these pieces together into a single coherent picture, balancing the influence of secular and environmentally-driven evolutionary processes. Most likely, the dominant processes vary throughout the life of a galaxy — e.g., galaxies may alternately build spheroids and grow disks as in the model of Baugh et al. (1996). In addition, galaxies that are subject to different processes may follow different evolutionary tracks, as suggested by the morphology-density relation (Dressler, 1980) or by the dichotomy between low surface brightness and high surface brightness galaxies (Mo et al., 1994; Taylor et al.,

1996). Finally, the relative importance of different evolutionary processes may vary with redshift and galaxy mass (Cowie et al., 1996; Patton et al., 1997; Mihos, 2001).

This thesis takes a basic observational step toward assembling a unified picture, by examining the distribution of evidence for various mechanisms of evolution within a survey explicitly designed to reflect the natural diversity of galaxies in the local universe. With newly acquired gas and stellar kinematic data, I examine clues to these galaxies' individual and collective formation histories, attempting to identify the essential drivers shaping the population as a whole. The survey, the different analysis approaches taken in this thesis, and the major results of each chapter are described below.

1.1 The Nearby Field Galaxy Survey

The kinematic data set acquired for this thesis builds on the Nearby Field Galaxy Survey (NFGS), a collection of UBR images and spectrophotometry for 196 nearby galaxies chosen to fairly represent the local galaxy population over a wide range in luminosity, $M_B = -23$ to -15 (Jansen et al., 2000b). What is unique about the survey is the combination of a big-picture perspective with the kind of high-quality data typically found only for a small sample.

The NFGS was selected to provide a broad cross-section of the low-redshift galaxy population, as if one were to take "a scoop of the universe." The sample makes no explicit cuts on galaxy morphology, color, line-of-sight inclination, diameter, surface brightness, or luminosity. Galaxies were chosen from the CfA 1 redshift survey (Huchra et al., 1983) without respect to environment, except for the exclusion of the nearby Virgo cluster to avoid an overrepresentation of cluster galaxies. The resulting sample is a field sample in the non-exclusive sense: it includes galaxies from all environments ranging from low to high density.

By drawing the NFGS from the CfA 1 redshift survey, Jansen et al. started with a statistically complete parent sample — a big improvement over bright galaxy catalogs. Nonetheless, the NFGS partakes of the inevitable biases inherent in its magnitude-limited parent survey, as well as inheriting the biases of its grandparent survey, the photographic plate-based Zwicky catalog. The sample inevitably misses some low surface brightness galaxies and dust-enshrouded, infrared-bright systems. Within these constraints, however, Jansen et al. sought to minimize bias and ensure that the NFGS sample would include a fair sample of galaxy types.

First, to avoid exacerbating the bias against low surface brightness galaxies,

Jansen et al. did not limit angular size directly. Instead, to increase the likelihood that sample galaxies would be smaller than the length of the spectrograph slit, the authors imposed a lower limit on redshift that increased with luminosity, so that brighter galaxies would be selected at greater distances.

Second, to ensure fair representation of each different galaxy type, Jansen et al. pre-sorted the candidate galaxies into bins by morphological type and luminosity. The survey sample was then selected by choosing "every Nth galaxy" in each bin. Such a strategy produces a representative, rather than a random sample: it negates the possibility of randomly choosing a set of galaxies that omits some segment of the population by pure bad luck.

Finally, Jansen et al. partially compensated for the bright-galaxy bias inherent in the magnitude-limited CfA 1 parent survey by giving increasing weight to fainter galaxies in the NFGS selection process: effectively, the "N" in the "every Nth galaxy" procedure was chosen to try to make the luminosity distribution of galaxies in the NFGS be proportional to the true luminosity distribution of galaxies per unit volume in the universe (the galaxy luminosity function). However, in practice the luminosity distribution of the NFGS is limited at the faint end by the small number of intrinsically faint galaxies available to select from the CfA 1 survey. Nonetheless, the NFGS spans an unusually wide range of galaxy luminosities, from bright ellipticals at $M_B = -23$ to faint dwarfs at $M_B = -15$.

1.2 The Kinematic Data

Kinematic data were obtained for all 196 galaxies in the NFGS over the course of ∼40 observing nights at Whipple Observatory, Mt. Hopkins, Arizona. Most of the data were acquired with the FAST spectrograph on the 60" Tillinghast Telescope (Fabricant et al., 1998); a few spectra were taken at the MMT with the Blue Channel Spectrograph. The survey includes two types of spectra: (1) high-resolution ($\sigma \sim 30$ km s^{-1}) ionized gas emission-line spectra centered on Hα, and (2) lower resolution ($\sigma \sim 60$ km s^{-1}) stellar absorption-line spectra centered on the MgI triplet. I personally reduced all of the two-dimensional long slit spectra and extracted the kinematic parameters. Stellar rotation curves were obtained using an existing cross-correlation routine in IRAF, while stellar velocity dispersions were computed with a code kindly provided by M. Franx. Gas rotation curves were extracted using a Gaussian fitting code I wrote to combine the signal from all available emission lines. This code was fully tested against alternative cross-correlation techniques in collaboration with E. Barton, as reported in Barton et al. (2000c).

A total of 270 reduced spectra are currently in the kinematic database, each of which represents a combination of 2–3 raw spectra from the telescope. All galaxies in the NFGS have at least one (stellar or gas) kinematic observation. Stellar kinematic data are available for 108 galaxies, including all elliptical and S0 galaxies in the sample and 73% of the Sa–Sbc spirals. Only 14% of galaxies typed Sc and later have stellar absorption line data, but we are working to increase this figure. In general, stellar kinematic information for extremely late type galaxies is rare in the literature due to the difficulty of achieving sufficient signal-to-noise, and such data may offer interesting surprises (see Chapter 2).

Gas kinematic data are available for all galaxies in the NFGS that have emission lines, to reasonable detection limits (see Chapter 4). The high-resolution emission-line spectra provide major-axis gas kinematics for 143 galaxies, plus minor-axis or 45°-off-axis gas kinematics for 19 galaxies. Emission lines in the lower resolution spectra (Hβ and [OIII]) provide major-axis gas kinematic data for another 10 galaxies. In total, major-axis gas kinematics are available for 98% of galaxies with morphological type Sa or later and 30% of earlier type galaxies; the remaining galaxies do not have ionized gas within our detection limits.

These observations provide a data set unique in both its broad coverage of the galaxy population and its provision of uniform, spatially resolved data describing both gas and stellar kinematics. Prugniel et al. (1998) catalog all existing spatially resolved kinematic data in the literature through 1998, a total of 4536 observations of 2207 galaxies. The single largest gas kinematic data set is the 970-galaxy Hα rotation curve survey of Mathewson et al. (1992), a spiral sample dominated by bright galaxies but also including some fainter late-type spirals down to about $M_B = -17$. Other large ionized gas rotation curve samples include the field galaxy and Virgo cluster spiral samples of Rubin and collaborators (Rubin et al., 1985, 1999) and the 300 galaxy Sb–Sc sample of Courteau (1997). Verheijen & Sancisi (2001) have conducted a resolved HI (neutral gas) survey of ∼40 spirals and dwarf galaxies in the nearby Ursa Major cluster, providing a nearly complete sample down to $M_B = -17$. The WHISP project has begun mapping several hundred galaxies in HI (Kamphuis et al., 1996) and eventually plans to make the data available to the community. None of these data sets offers matching stellar kinematic data.

Most large stellar kinematic data sets focus on bright elliptical and S0 galaxies, which are the easiest targets for absorption line observations and are useful for Fundamental Plane distance indicator work (e.g. Davies et al., 1987; Scodeggio et al., 1998). Héraudeau & Simien (1998) and Héraudeau et al. (1999) present one of the best available spiral bulge samples, with resolved stellar kinematics for the bulges of ∼70 Sa–Sc galaxies. A few small galaxy samples offer both gas and stellar data

acquired in a uniform fashion for a limited range of morphological types (e.g. Jore, 1997; Bertola et al., 1992; Caon et al., 2000). The NFGS is unique in providing such data for a wide range of morphologies and luminosities.

1.3 Research Approach

This work takes several approaches to studying galaxy evolution with the kinematic data described above. The first approach is to try to infer the specific evolutionary histories of individual galaxies from their individual kinematic properties. If hierarchical models of galaxy formation through interactions and mergers are correct (cf. Lacey & Cole, 1993; Schweizer, 1998), then these events should leave traces in a galaxy's kinematics. The bizarre phenomenon of galaxies with counterrotating gas and stars offers the most compelling kinematic evidence for such interactions, as the gas and stars almost certainly have different origins. Chapter 2 searches for evidence of counterrotation in the NFGS.

Even when the evolutionary histories of individual galaxies cannot be traced, statistical patterns may offer clues to how different classes of galaxies formed. For example, Rubin et al. (1999) have recently reported a higher rate of kinematic disturbances for spiral galaxies on orbits passing through the center of the Virgo cluster than for galaxies that avoid the cluster core, implying that the disturbances probably arise from interactions either between galaxies and the intracluster medium or between galaxies and other galaxies. Chapter 3 searches for statistical patterns in the distribution of rotation curve asymmetries within the NFGS.

Chapter 4 takes a similar statistical approach to analyzing how residuals from the Tully-Fisher relation vary with morphology, color, and a variety of other galaxy properties (including rotation curve asymmetry). In addition, this chapter adopts a comparative strategy, taking advantage of the complete Tully-Fisher data set recently published by Verheijen & Sancisi (2001) for the Ursa Major Cluster. Contrasting the NFGS with the Ursa Major survey highlights environmental dependences in galaxy evolution.

Finally, one can opt for the direct approach to studying galaxy evolution: a side-by-side comparison of galaxies at different ages of the universe. The basic difficulty in such an analysis lies in the mapping between distant and nearby galaxies: if we knew what the progenitors of present-day galaxies looked like, we wouldn't have to study galaxy evolution. A broadly representative low-redshift sample is essential to evaluate the possible scenarios. Chapter 5 examines evidence for luminosity evolution

at intermediate redshifts by direct comparison of the TF relation for the NFGS and the TF relations for two intermediate-redshift samples in the literature.

1.4 Summary of Results

Chapter 2

About 25–30% of emission-line elliptical and S0 galaxies have counterrotating gas and stellar components. This phenomenon provides fossil evidence for interactions and mergers in the E/S0 galaxy population. Counterrotation is rare for spiral galaxies, consistent with the idea that any retrograde gas from minor mergers will be dynamically neutralized, while major mergers will alter a galaxy's morphology. The abundance of faint S0 counterrotators and the possible detection of a Magellanic irregular counterrotator suggest that disk galaxies may sometimes arise from mergers between dwarf galaxies.

Chapter 3

Dwarf Sd-Im and emission-line E/S0 galaxies are more likely than spiral galaxies to have large gas rotation curve asymmetries in the plane of the disk. The largest measured asymmetry is for a Pec galaxy strongly warped by an interaction. Sources of rotation curve asymmetry include internal turbulence as well as external disturbances; not all kinematic asymmetries indicate asymmetry in the gravitational potential.

Chapter 4

Tully-Fisher (TF) scatter correlates with the physical properties of galaxies. For spirals brighter than $M_R^i = -18$, strong correlations between TF residuals and both $B-R$ color and Hα emission line strength (both indicators of recent and continuing star formation) make it possible to reduce scatter in the TF relation to approximately the level of NFGS measurement errors. The extremes of the correlations are driven by Sa galaxies and spirals with morphological peculiarities such as warps or multiple nuclei. The observed slope of the color–TF residual correlation is steeper than the slope predicted by stellar population synthesis models for quiescently evolving disk galaxies, suggesting the possibility that large starbursts, such as those induced by interactions and minor mergers, may play a significant role in some spirals' star

formation histories.

For dwarf galaxies, TF residuals correlate poorly with color and EW(Hα), but other physical properties become more important. Dwarfs that are overluminous with respect to the TF relation have properties suggestive of disturbance (high rotation curve asymmetry, rapid gas consumption by star formation) while dwarfs that are underluminous with respect to the TF relation have properties characteristic of less disturbed, passive evolution. The relative abundance of the two types of dwarfs appears to differ between the NFGS and a survey of galaxies drawn from the Ursa Major cluster, possibly indicating an environmental effect: the formation of undisturbed, slowly evolving dwarfs may have been suppressed in Ursa Major. These undisturbed dwarfs represent the most natural choice to extend the traditional undisturbed spiral-galaxy TF relation; however, they define a steep break in slope from the main relation.

Chapter 5

The NFGS permits a reevaluation of evidence for luminosity evolution in the intermediate-redshift TF relation. Careful recalibration of the TF relation for two intermediate-redshift samples indicates that galaxies were only modestly (if at all) brighter at redshifts of $\sim$0.3–0.5. However, this analysis is fundamentally limited by the lack of a broadly representative intermediate-redshift sample comparable to the NFGS.

Appendix

The appendix describes a highlight from my "other life" as an instrumentalist: the design and construction of IntroSpec, an optical fiber-fed CCD spectrograph built for the Harvard Astronomy Department.

1.5 Future Work

This thesis only scratches the surface of what may be learned from the NFGS. Several further projects are already underway. In one project, E. Barton and I are comparing rotation curve asymmetries for the NFGS with rotation curve asymmetries for her sample of galaxies in close pairs, in order to calibrate the role of galaxy interactions in producing such asymmetries. I am also collaborating with M. Pahre and R. Jansen in measuring near infrared photometric parameters, including bulge-to-disk ratios, for the NFGS. The infrared data will be useful for two further projects that will

make use of the combined gas and stellar kinematic database: an extension of the Fundamental Plane to spiral bulges (cf. Whitmore et al., 1979) and an analysis of the galaxy mass function. In addition, I have begun to explore how rotational-to-random velocity (v/σ) ratios for bulges vary as a function of galaxy properties, and I expect to continue this work in collaboration with J. Kormendy and a student at the University of Texas.

Chapter 2

A Broad Search for Counterrotating Gas and Stars: Evidence for Mergers and Accretion†

†Kannappan, S. K. & Fabricant, D. G. 2000, AJ, 121, 140
+ Kannappan, S. K. & Fabricant, D. G. 2000, PASP Conf. Series Vol. 230, 447, in press

ABSTRACT

We measure the frequency of bulk gas-stellar counterrotation in a sample of 67 galaxies drawn from the Nearby Field Galaxy Survey, a broadly representative survey of the local galaxy population down to $M_B \sim -15$. We detect 4 counterrotators among 17 E/S0's with extended gas emission ($24^{+8}_{-6}\%$). In contrast, we find no clear examples of bulk counterrotation among 38 Sa–Sbc spirals, although one Sa does show peculiar gas kinematics. This result implies that, at 95% confidence, no more than 8% of Sa–Sbc spirals are bulk counterrotators. Among types Sc and later, we identify only one possible counterrotator, a Magellanic irregular. We use these results together with the physical properties of the counterrotators to constrain possible origins for this phenomenon.

2.1 Introduction

Galaxies with counterrotating gas and stars offer dramatic evidence for the hypothesis of hierarchical galaxy formation. Counterrotation highlights the possibility of multiple events in a galaxy's formation history, as opposed to isolated collapse and infall models (Rubin, 1994; Schweizer, 1998). Studies of elliptical, S0, and Sa galaxies have demonstrated that gas-stellar counterrotation and related phenomena such as non-coplanar rotation may be quite common (e.g. Bertola et al., 1992; Jore, 1997), although cospatial stellar-stellar counterrotation may be less so (Kuijken et al., 1996). However, the frequency of these phenomena in the general galaxy population is uncertain. Equally important, we do not know whether the physical processes responsible for counterrotation merely perturb the host galaxy along the Hubble sequence, or completely reshape it. Comparisons of gas accretion and merger scenarios have been inconclusive (Thakar et al., 1997; Galletta, 1996).

Combining the compilation of Galletta (review 1996) with a few recent discoveries (Kuijken et al., 1996; Morse et al., 1998; Jore, 1997), we identify in the literature at least 18 elliptical and S0 gas-stellar counterrotators, as well as 9 spiral and later type galaxies. Non-coplanar rotation, particularly in the stable configuration of a polar ring, may also be common: Whitmore et al. (1990) list 6 kinematically confirmed polar ring galaxies and many more visual candidates. Unfortunately the statistical implications of these numbers are unclear, since so many of the discoveries were serendipitous.

To date, the best statistical estimates of the frequency of gas-stellar counterrotation come from studies restricted to early type galaxies. Bertola et al. (1992)

and Kuijken et al. (1996) have analyzed samples of emission-line S0's and report that ∼20–25% of these galaxies show counterrotation or other strong kinematic decoupling between the gas and stars. Jore (1997) has surveyed 23 isolated, unbarred Sa galaxies and finds 4 that show clear gas-stellar counterrotation along the major axis, with the bulk of the stars rotating opposite to the bulk of the gas (see also Haynes et al., 2000).

Here we report the frequency of gas-stellar counterrotation along the major axes of 67 galaxies ranging from ellipticals to Magellanic irregulars. This work makes use of data from the recently completed Nearby Field Galaxy Survey (NFGS, Jansen et al., 2000b,a; Kannappan et al., 2001c), which contains imaging, spectrophotometric, and kinematic observations for ∼200 galaxies drawn from the CfA 1 redshift survey (Huchra et al., 1983). Jansen et al. designed the survey to provide a fair sampling of the local galaxy population, with as little selection bias as possible. Galaxies were chosen without preference for morphology, environment, inclination, or color, beyond that inherent in the B-selected and surface-brightness limited parent survey.

An important virtue of the NFGS is its inclusion of the faint galaxy population. To counteract the observational bias toward bright galaxies, Jansen et al. selected galaxies from CfA 1 approximately in proportion to the local galaxy luminosity function (e.g. Marzke et al., 1994). The resulting sample spans luminosities from $M_B \sim -23$ to -15, limited only by the decreasing CfA 1 survey volume at faint magnitudes.

2.2 Data & Methods

All distances and magnitudes are computed with H_o=75, using a simple Hubble flow model corrected for Virgocentric infall as in Jansen et al. (2000b).

2.2.1 Sample

The sample analyzed in this paper consists of all 67 NFGS galaxies for which we have both stellar and ionized gas rotation curve data. This group includes 100% of the E/S0's with detectable ionized gas, i.e. 17 of 57 or 30% of all E/S0's. For later types, the stellar kinematic database is incomplete: gas and stellar data are available for 38 of 52 early type Sa-Sbc spirals (73%), and 12 of 87 later type spiral and irregular galaxies (14%). Figure 2.1 shows the sample in the context of the NFGS, demonstrating that the 55 E-Sbc galaxies we analyze provide a fair sample of the full survey population of emission line galaxies, whereas the 12 galaxies typed Sc and later do not.

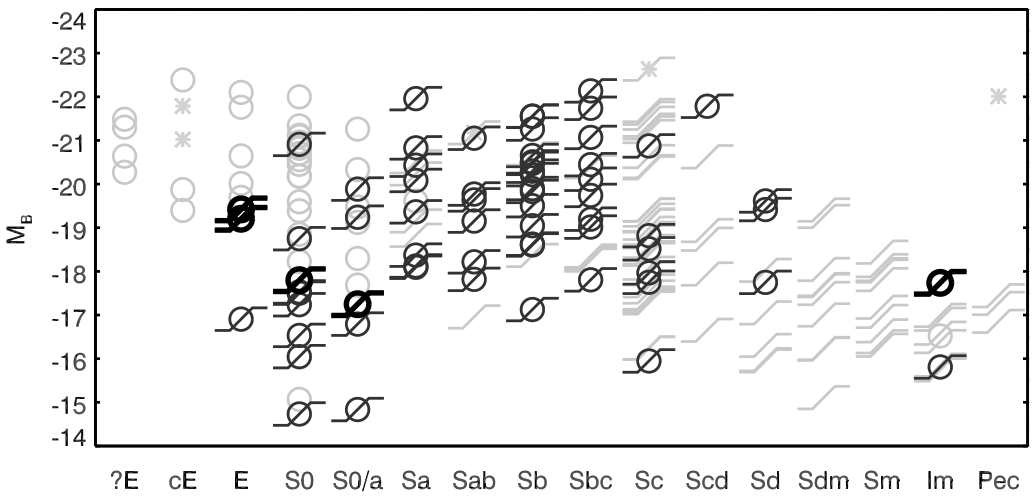

Figure 2.1.— An overview of the Nearby Field Galaxy Survey, showing the demographics of all 196 galaxies sorted by morphology and B-band luminosity. A circular symbol indicates that we have stellar absorption line data for the galaxy, while an S-shaped symbol indicates that we have extended gas emission line data. The subsample of galaxies analyzed for gas-stellar counterrotation consists of all galaxies for which both symbols appear. These 67 galaxies are shaded dark gray, with counterrotators in thick black. Here we have separated S0/a's from S0's to reduce crowding in the figure, although the original morphological classification does not discriminate reliably between these two classes and all are considered "S0" in the text. A star indicates that absorption line data were obtained but are strongly contaminated by an AGN.

2.2.2 Observations & Data Reduction

Long slit spectra were obtained at the F. L. Whipple Observatory during several observing runs from 1996 to 1999, primarily using the FAST spectrograph on the Tillinghast Telescope (Fabricant et al., 1998). The entire data set and full details of the data reduction are described elsewhere (Kannappan et al., 2001c). In most cases, we have only major axis spectra.

For the gas kinematics, we observed a 1000 Å interval centered on H_α, with a spectral resolution of $\sigma \sim 30$ km s^{-1} and a spatial binning of 2.3 arcseconds/pixel, comparable to the typical seeing of 2". For the stellar kinematics, we observed a 2000 Å interval centered on the MgI triplet at 5175 Å, again with 2.3 arcseconds spatial binning, but with spectral resolution $\sigma \sim 60$ km s^{-1}. We also obtained stellar kinematic data for a few galaxies with the Blue Channel Spectrograph on the MMT, using a configuration with 1.2 arcsecond binning, reduced wavelength coverage, and $\sigma \sim 40$ km s^{-1}. Spectra of non-rotating G and K giant stars were recorded to serve as velocity templates for the absorption line data.

All of the data were reduced by standard methods, including bias and dark subtraction, flat-fielding, wavelength calibration, heliocentric velocity correction, sky subtraction, spectral straightening, and cosmic ray removal, using IRAF and IDL.

We extract high-resolution gas rotation curves (RC's) by simultaneously fitting H_α, [NII], and [SII] lines, excluding data with S/N < 3. When possible, we also derive low resolution RC's from H_β and [OIII] lines appearing in the stellar absorption line spectra. The low resolution RC's act as the primary data for 10 galaxies for which we lack H_α observations, and otherwise serve as confirming data. In cases of severe H_α or H_β absorption, we rely on RC's derived from the [NII], [SII], and [OIII] lines.

To extract stellar rotation curves, we cross correlate the galaxy absorption line spectra with the stellar template spectra in Fourier space, using **xcsao** in the rvsao package for IRAF (Kurtz et al., 1992). We accept fits with R values > 3.5 and error bars < 35 km s^{-1}. We check this procedure by deriving stellar RC's with a velocity dispersion analysis code kindly provided by M. Franx, described in Franx et al. (1989). The two methods yield consistent results within the errors. We exclude a few points in the outer parts of one galaxy, A11332+3536, where the two methods do not yield overlapping error bars.

2.2.3 Identification of Gas-Stellar Counterrotators

Operationally, we assume that a single rotation curve adequately describes the kinematics of the stars, and likewise the gas. In reality, multiple velocity components may well be present (e.g. Jore, 1997), but our spectra have insufficient signal to noise for us to detect secondary velocity components in an unbiased way. Instead we search for bulk counterrotation between the gas and stars. Our approach highlights the most extreme counterrotators, but the number of counterrotators we find should be considered a lower limit.

We adopt the simplest possible definition of a counterrotator: a galaxy in which the observed gas and stellar rotation curves show opposite sign. Again, this approach yields a lower limit, because our stellar curves have varying spatial extent, and some galaxies may contain undetected velocity reversals at large radii, similar to the reversal we see in NGC 3011 (Figure 2.2). Furthermore, not all apparent counterrotators actually contain gas and stars in coplanar counterrotating disks. An inclined gas disk may also create an apparent counterrotation signature, and this scenario provides a plausible interpretation for one of our galaxies (see §2.3.1). However, we note that the processes that produce inclined disks and those that produce coplanar counterrotating disks are probably similar, and the former may even evolve into the latter, so our interpretation does not rest critically on this distinction.

We estimate the confidence level for each counterrotation detection by attempting to rule out a model in which the stars simply do not rotate. Using a standard χ^2 minimization algorithm, we fit a straight line to the stellar rotation curve to determine its slope and the error on the slope. In most cases the stellar RC may be reasonably (if crudely) approximated by a straight line, except in NGC 3011, which shows a mix of corotation and counterrotation (see §2.3.1). In this case we fit just the counterrotating points. The slope divided by the error on the slope constitutes the confidence level of our claim of *counter*rotation, as opposed to zero rotation. For two galaxies that we label counterrotators, the data differ from a zero rotation model by only 2–3σ, so such a model cannot be completely ruled out. On the other hand, three S0's and one Im galaxy rotate so little that we cannot definitely say that they are *not* counterrotators. We return to this point in §2.3.2. [1]

[1] Our sample also contains one peculiar case, an Sa galaxy (NGC 4795, see Kannappan & Fabricant, 2001b) in which the gas appears to be non-rotating, despite stellar velocities $\sim$150 km s^{-1} and despite a tight match between the major axis position angle and the observed PA's. There is a faint suggestion that better data might show counterrotation at radii $\lesssim$ 1 kpc, but the present data do not permit such a claim. This is the only such case in our 67 galaxy sample. NGC 4795 exists in a field of multiple small companions, and it may be accreting one of them.

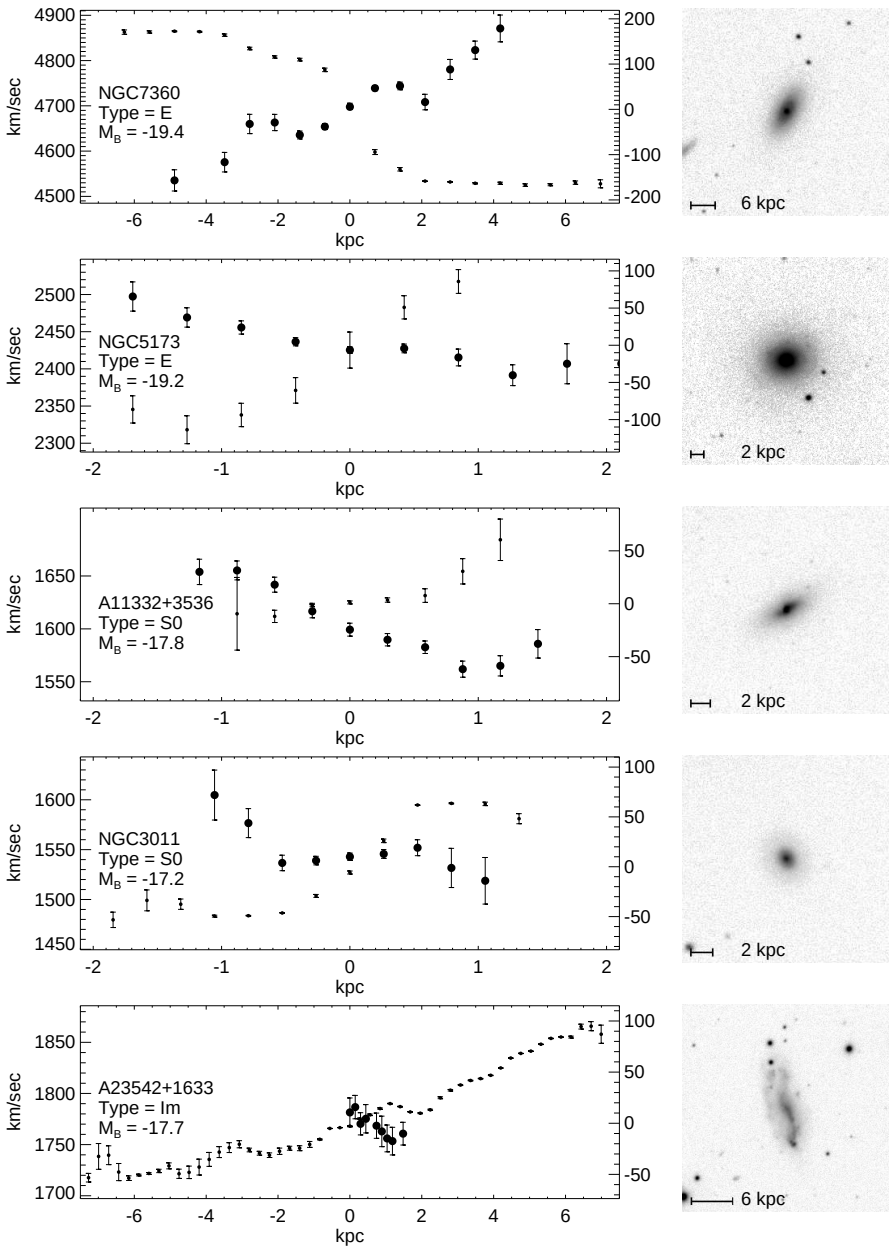

Figure 2.2.— Major axis rotation curves and images for the five gas-stellar counter-rotators (see Tables 1–2). Small dots show ionized gas emission line data, and large dots show stellar absorption line data. No correction has been made for inclination to the line of sight. Images shown are U or B-band exposures, courtesy of Jansen et al. (2000b).

Table 1. Basic Properties of Counterrotators

Galaxy	UGC	Conf.[a] (σ)	Dist.[b] (Mpc)	M_B[b] (mag)	r_e[b] (kpc)	Type[c]	Morphology Notes
NGC 3011	5259	3.0	24.0	-17.2	0.8	S0	completely smooth
A11332+3536	6570	11.6	26.7	-17.8	1.2	S0	faint inner bar+arms
NGC 5173	8468	5.9	38.5	-19.2	1.8	E	outer knottiness, arms[d]
NGC 7360	12167	17.5	63.4	-19.4	3.9	E	smooth, very elongated
A23542+1633	12856	2.2	25.4	-17.7	4.0	Im	knotty elongated core

[a]Confidence level of claim that stars *counter*rotate, as opposed to having zero rotation. For NGC 3011, only the outer four points are considered. See §2.2.3.

[b]Distances, magnitudes, and effective radii from Jansen et al. (2000b), converted to H_o=75.

[c]Morphological types as used by Jansen et al. (2000b), except that we refer to all lenticular galaxies from L- to S0/a as "S0."

[d]Vader & Vigroux (1991) observe possible spiral arms in their continuum-subtracted B-band image of this galaxy.

2.3 Results & Discussion

2.3.1 Individual Counterrotators

In our sample of 67 galaxies, we identify five likely gas-stellar counterrotators: 2 S0's, 2 E's, and 1 Im. Figure 2.2 shows their rotation curves and images, and Tables 1–4 summarize their properties. Figure 2.3 shows the available minor axis data.

We note that the type Im counterrotator found here, A23542+1633, may be the first known gas-stellar counterrotator in this morphology class, although the confidence level of the detection is not decisive (by fitting the slope as described in §2.2.3, we rule out a stellar non-rotation model at 2.2σ confidence, and rule out equal-amplitude corotation at 3.2σ confidence). Galletta (1996) lists several counterrotators as "Irr," but these are peculiar rather than Magellanic irregular galaxies. The only previous observation of any form of counterrotation in a Magellanic irregular galaxy appears to be that of Hunter et al. (1998), who have reported two counterrotating H I gas components in NGC 4449. We should of course consider the possibility that A23542+1633 might display misleading velocity reversals due to gas infall along the elongated structure on its major axis. However the gas RC does not show large velocity reversals. The small velocity shifts near $\sim\pm2$ kpc may reflect infall, especially given the fluctuations seen in the minor axis RC (Figure 2.3), but these shifts do not dominate the major axis kinematics.

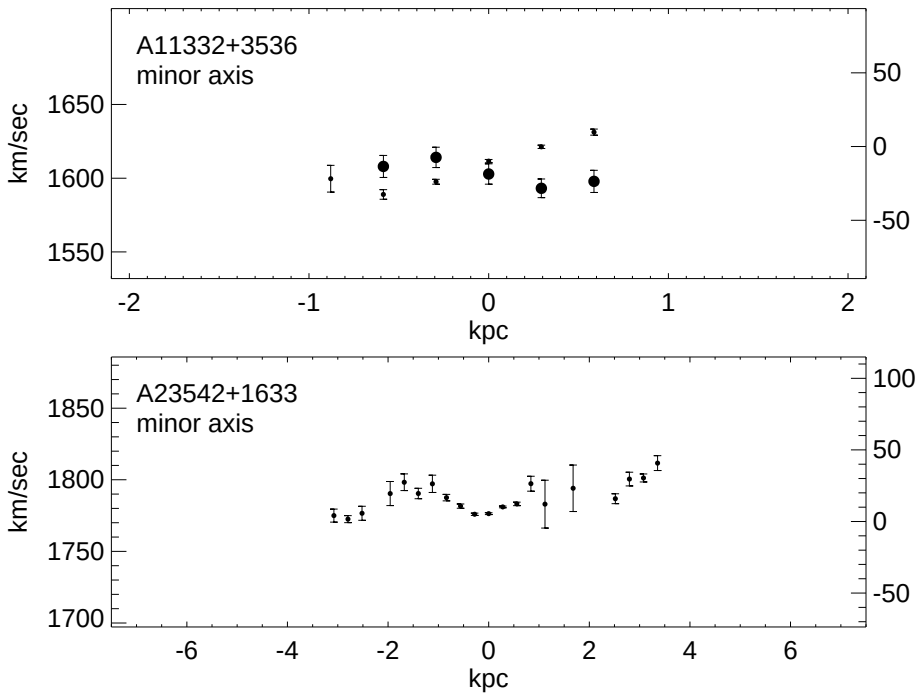

Figure 2.3.— Minor axis rotation curves for A11332+3536 and A23542+1633. Small dots show ionized gas emission line data, and large dots show stellar absorption line data (none is available for A23542+1633). No correction has been made for inclination to the line of sight.

Table 2. Position Angles Observed

Galaxy	Major Axis PA [a]	Stellar RC PA	Gas RC PA
NGC 3011	52	50	52
A11332+3536	123	122, 32 (minor axis)	same observations [b]
NGC 5173	100	100	same observation [b]
NGC 7360	153	153	153
A23542+1633	12	20 [c]	12, 102 (minor axis)

[a]Major axis PA's are as compiled by Jansen et al. (2000b) from the Uppsala General Catalog of Galaxies (UGC, Nilson, 1973); except for NGC 5173, for which the UGC lists indefinite PA. Vader & Vigroux (1991) measure a PA of 100 ± 5 from their high-quality B band image of this galaxy.

[b]For A11332+3536 and NGC 5173, we do not have data in the 6000–7000 Å range, so our primary gas RC's are derived from [OIII] and H_β emission lines in the stellar absorption line spectra.

[c]This observation was obtained at the Multiple Mirror Telescope Observatory, a facility operated jointly by the University of Arizona and the Smithsonian Institution.

In the S0 A11332+3536, the apparent counterrotation may be caused by an inclined gas disk. Consistent with a misaligned disk, the minor axis gas shows velocity amplitude comparable to the major axis gas, and while the minor axis gas appears to rotate faster than the stars, the major axis gas appears to rotate slower than the stars (see Figures 2.2 & 2.3). This galaxy also has a small bar along its minor axis. Bettoni (1989) and Galletta (1996) point out that radial motions along a bar may sometimes create a false impression of counterrotation in one-dimensional data; however, in this case the orientation of the bar makes confusion due to non-circular motions unlikely.

In NGC 3011, the stellar rotation pattern changes with radius. Stars within $\sim$0.5 kpc rotate very slowly (if at all) in the same sense as the gas, while stars at larger radii counterrotate with 3σ confidence. This combination suggests that the inner stars may consist of two oppositely rotating stellar populations, one population having formed more recently from infalling gas. Further data would be required to test this hypothesis.

2.3.2 Statistics

Figure 2.1 shows the distribution of gas-stellar counterrotators in morphology and luminosity, within the context of our 67 galaxy sample as well as the larger NFGS. The bulk counterrotation frequency for the 67 galaxy sample is $\sim$7%. However,

Table 3. Gas and Star Formation Properties of Counterrotators

Galaxy	$M_{\rm HI}$ [a] ($M_\odot$)	$M_{\rm HI}/L_B$ ($M_\odot/L_\odot$)	SFR[b] ($M_\odot$/yr)	T[c] (Gyr)	EW(H_α)[d] (Å)	$B-R$[e] (mag)
NGC 3011	8.6E+07	0.07	0.055	1.6	-15.81	1.20
A11332+3536	2.4E+08	0.12	0.096	2.5	-15.42	1.17
NGC 5173	2.1E+09	0.28	0.078	27	-3.13	1.29
NGC 7360	3.6E+09	0.39	0.073	49	-2.37	1.35
A23542+1633	2.3E+09	1.21	0.220	11	-62.33	0.69

[a]Computed from H I fluxes (Bottinelli et al., 1990; Theureau et al., 1998).

[b]Computed from Hα fluxes (R. Jansen, private communication) using the calibration of Kennicutt (1998).

[c]Gas consumption timescale uncorrected for recycling.

[d]Jansen et al. (2000a).

[e]Jansen et al. (2000b).

this number includes E/S0's, early type spirals, and later type galaxies in differing proportions (§2.2.1) and would likely be lower in a properly weighted sample.

For E/S0's taken alone, gas-stellar counterrotators comprise 4 out of 17 emission line galaxies in the NFGS, which we survey completely. This result yields a frequency of 24^{+8}_{-6}% (errors are 68% confidence limits from binomial distribution statistics). If we exclude the 3 S0's that show almost no rotation (§2.2.3), then the statistics are 4 in 14, or 29^{+10}_{-8}%. In sharp contrast, we find no clear cases of counterrotation among 38 Sa–Sbc spirals, although one Sa does show another form of kinematic decoupling (NGC 4795, see note 1). This rate of non-detection implies that, at 95% confidence, no more than 8% of such early type spirals are bulk counterrotators. For types Sc and later, we can make no statistical conclusions due to inadequate sampling.

The strong clustering of the NFGS counterrotators in the early type morphology region of Figure 2.1 probably arises from two factors. First, if counterrotation originates from galaxy mergers (as discussed in §2.3.3), then early type morphologies are a natural corollary. Second, if galaxies of all types were to accrete retrograde gas with equal probability, then this gas would survive longer in relatively gas-poor early type galaxies, where collisions with existing gas and loss of angular momentum are less important.

Figure 2.1 also illustrates the tendency of our gas-stellar counterrotators to have low luminosity (sub-L_*). This result may simply reflect the fact that low luminosity galaxies, especially early types, are more likely to be gas rich, while brighter galaxies

Table 4. Neighbors of Counterrotators [a]

Galaxy	Nearest Neighbor	Nearest Brighter Neighbor
NGC 3011	270 kpc, 0.6 mag fainter	440 kpc, 2 mag brighter
A11332+3536	175 kpc, 0.5 mag fainter	240 kpc, 0.4 mag brighter
NGC 5173	50 kpc, 1.2 mag fainter	180 kpc, 0.3 mag brighter
NGC 7360	none in UZC[b]	
A23542+1633	480 kpc, 0.1 mag brighter[c]	same as nearest neighbor

[a]Based on a search of the Updated Zwicky Catalog (Falco et al., 1999) within 600 kpc and 600 km s^{-1}; all neighbors listed have $\Delta v<250$ km s^{-1}.

[b]Small projected neighbor appears to be a background galaxy.

[c]A bright knot within this galaxy has at times been interpreted as a neighbor, but is in fact part of the main galaxy.

often have too little gas for us to detect, and so are not part of our sample.

Previous studies of gas-stellar counterrotation have focused on samples restricted by morphology. Jore (1997) and Haynes et al. (2000) analyze the detailed kinematics of a sample of 23 isolated, unbarred Sa galaxies. Their sample contains 4 bulk gas-stellar counterrotators, suggesting that we should see ∼1–2 examples among our 8 Sa's. In fact, we see none, but our results are consistent within the small number statistics. Also, we do find one Sa with kinematically decoupled gas (NGC 4795, see note 1), apparently non-rotating even at radii ∼3 kpc. The sense of gas rotation in the central ∼1 kpc of this galaxy is not well determined.

In two surveys of S0's with extended gas emission, Bertola et al. (1992) and Kuijken et al. (1996) independently obtain gas-stellar counterrotation frequencies of ∼20–25% for samples of 15 and 17 objects respectively. Combining the two surveys yields a frequency of $\sim 24^{+6}_{-5}\%$ for a total sample of 29 galaxies, with 3 objects common to both samples. Both surveys were drawn from bright galaxy catalogs and contain objects in the range $M_B \sim -21$ to -18, with a median of ~ -19.

By comparison, the 14 S0's with extended gas emission in the NFGS span luminosities from $M_B = -20.9$ to -14.7, with a median of ~ -17. Only ∼30% of these NFGS galaxies overlap the luminosity range of the two bright galaxy surveys (see also Kannappan & Fabricant, 2001b). Nonetheless, our gas-stellar counterrotation statistics for these 14 S0's agree with Bertola et al. and Kuijken et al. within the errors: $14^{+9}_{-6}\%$, or $18^{+12}_{-8}\%$ if we exclude the 3 S0's that show almost no rotation (§2.2.3).

Such agreement suggests the possibility that similar mechanisms form emission line S0's over a wide range of physical scales — at least $M_B \sim -21$ to -17, the range

within which S0 gas-stellar counterrotators have now been detected. However, we should point out that the low luminosity "S0" population is heterogeneous, and may include objects with very different formation histories. We assigned the S0 classification purely based on morphology, so it applies to all NFGS galaxies with the visual appearance of a two-part bulge+disk structure with minimal spiral structure. At low luminosities, this category reveals at least two subclasses: mostly smooth galaxies, and knotty or otherwise peculiar galaxies, typically with centers bluer than their outer parts (often labelled blue compact dwarfs). It is possible that only the smoother subclass forms a continuum with higher luminosity S0's in terms of formation history, or alternatively that the more peculiar objects are simply at an earlier stage of evolution. Our two S0 counterrotators have most in common with the smoother subclass, although A11332+3536 does have a small central bar and tiny spiral arms.

2.3.3 Formation Mechanisms

The two most plausible formation mechanisms for gas-stellar counterrotators are late-stage gas accretion and galaxy mergers (e.g. Thakar et al., 1997; Rubin, 1994, and references therein). Secular evolution cannot easily explain large quantities of chemically enriched counterrotating gas (e.g. Caldwell et al., 1986). We do not separately discuss inclined gas disks here, since they are likely to be closely related to counterrotating disks.

Late-stage gas accretion mechanisms include acquisition of a large H I cloud, transfer of gas during a close encounter, and infall of nearby gas stimulated by a flyby of another galaxy.

Assuming that the counterrotators' H I gas rotates in the same peculiar sense as their ionized gas, accretion of a single H I cloud cannot easily explain these galaxies' substantial H I gas masses ($\sim 10^8 - 10^9$ $M_\odot$, Table 3). If the accreted H I cloud were similar to the high velocity clouds found near the Milky Way, then it would have an H I mass of $\sim 10^7$ $M_\odot$, at least an order of magnitude too small (Blitz et al., 1999). Note that this estimate assumes that the high velocity clouds are local group objects at $\sim$1 Mpc distances — if the clouds are closer to the Milky Way, then their H I masses are even smaller (Zwaan & Briggs, 2000).

The likelihood of either companion gas transfer or infall triggered by a flyby encounter is harder to evaluate, especially since the responsible galaxy may have left the neighborhood or may be too faint to be included in a galaxy catalog. We can only say that we see no strong evidence in favor of this scenario. Based on a search of the Updated Zwicky Catalog (Falco et al., 1999) within 600 kpc and 600 km s^{-1} of

each counterrotator, only one counterrotator has a neighbor within 150 kpc projected on the sky (NGC 5173, see Table 4). However, Knapp & Raimond (1984) have mapped this galaxy in detail in H I, and they see no evidence for H I flow from the companion. The lack of obviously interacting companions near our counterrotators is consistent with expectations based on the analogy between counterrotation and polar rings. Brocca et al. (1997) compare the local environments of ∼50 apparent polar ring galaxies with those of a control sample, and they find no statistical difference between the two groups in the number of close neighbors of comparable luminosity within ∼600 kpc.

Of course, the fact that 4 of our 5 counterrotators have E/S0 morphology hints that they probably exist in regions of high local galaxy density, which density calculations confirm (courtesy N. Grogin, see Figure 2.4), although the environments are only moderately dense. This observation is consistent with either flyby or merger formation scenarios.

Mergers provide a simple alternative to late-stage gas accretion mechanisms. In this case the companion is gone, so no enhanced abundance of close neighbors is expected. The scale of the merger might range from satellite accretion to a major merger of comparably sized galaxies (though not necessarily comparably gas rich). Even mergers with dwarf galaxies could easily yield the H I gas masses observed, which are similar to the H I masses of late type dwarfs in the NFGS (computed from catalog H I fluxes, Bottinelli et al., 1990; Theureau et al., 1998).[2]

As discussed in §2.3.2, the tendency for bulk counterrotators to have early type morphologies may mean that both morphology and counterrotation have a common origin, in which case the merger would have been substantial. On the other hand, minor satellite accretion could also explain the primarily early type morphologies of the counterrotators, if galaxies of all types accreted small neighbors, but the retrograde gas did not survive in gas rich later types. We expect that retrograde gas will shock with existing prograde gas and either form stars immediately or lose angular momentum, creating enhanced infall and central star formation (Lovelace & Chou, 1996; Kuznetsov et al., 1999).

For the round elliptical NGC 5173, either scenario is plausible. Knapp & Raimond (1984) propose that this galaxy may have formed when a gas poor elliptical accreted a gas rich satellite; such an event could explain the galaxy's apparently small

[2]The relative plausibility of mergers vs. gas accretion would be much better constrained for the NFGS counterrotators if we could determine the mass and extent of any counterrotating stellar populations (see comments regarding NGC 3011, §2.3.1). Our existing data do not permit such an analysis, but we plan to obtain higher resolution stellar kinematic data to address this question.

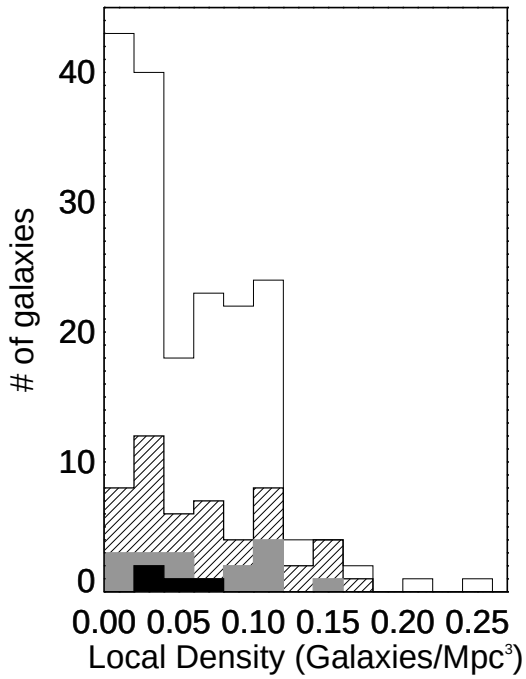

Figure 2.4.— A histogram of local galaxy density around each sample galaxy. Successively smaller histograms represent in order: the entire NFGS sample, E/S0's in the NFGS sample; E/S0's with extended gas emission; and the four E/S0 gas-stellar counterrotators. Densities were provided by N. Grogin (private communication), and were derived from the CfA 2 survey using the methods described in Grogin & Geller (1998). These calculations yield densities smoothed over ∼6.7 Mpc scales (H_o=75), counting only galaxies brighter than $M_B \sim -17$. Grogin & Geller compute densities as multiples of the mean density; we convert these to an absolute scale using their choice of mean density, 0.03 galaxies/Mpc^3 for H_o=75. Six NFGS galaxies outside the bounds of the CfA 2 survey volume are excluded from the figure, none of which has extended gas emission.

dust to gas mass ratio (Vader & Vigroux, 1991). Alternatively, simulations show that major mergers between gas rich disk galaxies can also produce counterrotating gas in an elliptical (Hernquist & Barnes, 1991).

For the two S0 counterrotators and the disky elliptical NGC 7360, minor mergers present a likely intermediate option. Simulations by Bekki (1998) and Naab et al. (1999) show that minor mergers produce disky remnants, and when dissipation and star formation are included, gas rich minor mergers can produce gas poor S0's (Bekki, 1998).

Rix et al. (1999) reject the minor merger hypothesis for low luminosity E/S0's because observations of these galaxies show significantly greater rotational support than is seen in 3:1 disk merger simulation remnants. However, none of the simulations for which v/σ information is available include the physics of dissipation, infall, and star formation, which are clearly critical ingredients in the formation of a disk from gas rich progenitors.

In our view, minor or even gas-rich major mergers provide a very plausible formation mechanism for disky low luminosity E/S0's, if one considers that the likely progenitors bear little resemblance to the model galaxies currently used in merger simulations. Mihos & Hernquist (1994) have shown that bulgeless disk galaxy mergers evolve very differently from bulge + disk galaxy mergers, but no one has yet modelled the complexities of a dwarf-dwarf merger. For example, the progenitors might be gas rich dwarfs with extended filamentary H I envelopes that continue to fall into the remnant late in the merger process. The gas dynamics of small gravitational potential wells may also be important: many small early types in the NFGS display broad emission line wings, possibly related to mass outflows.

Given the steeply rising numbers of galaxies at the faint end of the galaxy luminosity function (Marzke et al., 1994), gas rich dwarf-dwarf mergers are inevitable, and some of the remnants of such mergers may well look like S0's, or spirals embedded in S0 envelopes. The existence of very low luminosity S0's, and counterrotators as faint as $M_B \sim -17$, contrasts with the sharp decrease in early type spirals fainter than $M_B \sim -18$ and the corresponding increase in the number of late type dwarfs (Figure 2.1, see also Sandage et al., 1985; Schombert et al., 1995; Marzke et al., 1994). We note that the faint population of the NFGS contains a number of possible "proto-S0's" — galaxies with very blue centers and outer envelopes reminiscent of early types (Jansen et al., 2000b). These galaxies are variously typed late or early depending on the surface brightness of the envelope and the degree of inner structure. In the nomenclature of the dwarf galaxy literature, some would be known as blue compact dwarfs, a class of galaxies showing many of the expected characteristics

of merger remnants (Doublier et al., 1997). [3]

Of course, some dwarf merger remnants probably just turn into bigger, brighter late type dwarfs. For example, although the Im counterrotator A23542+1633 appears to be actively evolving, with ongoing infall (§2.3.1) and moderately strong star formation (Table 3), it does not much resemble a proto-S0, but appears more like a proto-Sd.

If the counterrotators are merger remnants, one might expect them to show signatures of enhanced past or present star formation. On the other hand, the E/S0 counterrotators' smooth morphologies (with small perturbations, see Table 1) suggest that for these four galaxies, the merger probably took place at least ∼1 Gyr ago (Schweizer, 1998). In keeping with this view, these galaxies show moderate H_δ absorption equivalent widths (∼1–3 Å, R. Jansen, private communication), consistent with starburst ages greater than ∼1.5 Gyr for solar metallicity (Worthey & Ottaviani, 1997). By contrast, the one irregular counterrotator shows stronger H_δ absorption (∼5–6 Å, subject to some uncertainty in the emission correction), suggesting a more recent/ongoing starburst. We note also that for the two faint S0's, the nominal gas consumption timescale is relatively short (∼2 Gyr uncorrected for recycling, see Table 3), possibly implying rapid evolution. In fact, both of these galaxies are Markarian galaxies and have starburst nuclei (Balzano, 1983).

2.4 Conclusions

We have searched for bulk gas-stellar counterrotation in 67 galaxies spanning a broad range of morphologies and luminosities within the ∼200 galaxy NFGS sample. This sample permits statistical conclusions for types E–Sbc, and includes a few later types as well. However, our detections represent a lower limit to the true rate of counterrotation, because the data do not permit separation of multiple kinematic components and do not rule out counterrotation beyond the radial extent of the observations.

We detect 5 gas-stellar counterrotators, generally of early type and low luminosity. These galaxies include 2 E's, 2 S0's, no spirals, and 1 Magellanic irregular. The Im galaxy counterrotates with 2.2σ confidence, and if confirmed represents the first known example of gas-stellar counterrotation in a Magellanic irregular. One of the S0 counterrotators probably contains an inclined gas disk rather than coplanar counter-

[3] None of this precludes that some S0's may form through tidal stripping, but it would be rather difficult to form a counterrotator that way, unless the formation of the galaxy and the acquisition of counterrotating gas were entirely separate events.

rotation; we assume that these phenomena are closely related in our interpretation.

Statistically, we conclude that $24^{+8}_{-6}\%$ of E/S0's with extended emission are bulk gas-stellar counterrotators, or $29^{+10}_{-8}\%$ if we exclude 3 S0's that display very little rotation. In contrast, our non-detection of spiral counterrotators implies that no more than 8% of Sa–Sbc spirals are bulk counterrotators, at 95% confidence. This morphological dependence of counterrotation frequency may arise from two effects. First, if galaxy interactions and mergers are responsible for creating the counterrotators, then the same mechanisms will tend to produce early type morphologies. Second, even small-scale retrograde gas accretion events that do not strongly reshape morphology will be easier to detect in E/S0's, because bright spiral galaxies will typically have sufficient prograde gas to dynamically neutralize the infall.

Sa galaxies may represent a transitional case. Although we detect no Sa counterrotators, our sample is small (only 8 galaxies) and includes one galaxy in which the sign of the central gas rotation is uncertain. The same galaxy shows clear gas-stellar decoupling at larger radii, where its gas displays zero apparent rotation, despite large stellar velocities. Jore (1997) finds that ∼15–20% of bright, unbarred Sa's are bulk gas-stellar counterrotators.

For S0's with extended gas emission, the frequency of gas-stellar counterrotation we derive agrees with the results of Bertola et al. (1992) and Kuijken et al. (1996), although the median luminosity of our sample is ∼2 mag fainter ($M_B \sim -17$). The agreement suggests that similar mechanisms form this category of S0's over a wide range of physical scales, at least $-17 > M_B > -21$.

As noted by Bertola et al. (1992), every known counterrotator implies at least one corotator that formed by a similar process, and probably more due to effects that tend to erase the retrograde kinematic signature. Therefore the ∼25% bulk counterrotation rate for emission line E/S0's implies that at least ∼50% of E/S0's with extended gas emission have experienced the evolutionary processes that produce gas-stellar counterrotation.

In examining the range of possible processes, we conclude that galaxy mergers (including satellite accretion) provide the most plausible explanation for the counterrotators, especially given these galaxies' significant H I masses and lack of obvious companions. However flyby or faint companion interactions remain a possibility. We note that the possible products of gas rich dwarf-dwarf mergers remain largely unexplored in detailed simulations, despite clear evidence for such mergers in the faint galaxy population, and we suggest that our S0 and Im dwarf counterrotators may be products of such mergers.

2.5 Appendix: Frequency of Gas-Stellar Counterrotation‡

2.5.1 Abstract

We search for bulk counterrotation of the gas and stars in 67 galaxies of all types and a wide range of luminosities. Bulk counterrotation characterizes ∼25–30% of E/S0's with extended gas, but at most a few percent of Sa–Sbc spirals. For S0's, the frequency of counterrotation we derive agrees with previous work, but we sample significantly fainter luminosities. Thus the agreement suggests that similar formation mechanisms may operate over a wide range of physical scales.

2.5.2 Sample

The survey sample (Figure 2.5) consists of 67 galaxies drawn from the Nearby Field Galaxy Survey (NFGS), a survey of ∼200 galaxies including all morphological types in their natural abundance and spanning luminosities from $M_B \sim -23$ to -15 (Jansen et al., 2000b). Our sample includes all of the NFGS E/S0's with extended gas emission, a representative majority of the Sa–Sbc spirals, and a few later types. Three S0's show minimal rotation with uncertain sense.

2.5.3 Results

Counterrotators are circled in Figure 2.5. Four are E/S0's, totalling 24(29)% of all sample E/S0's with(without) the 3 uncertain S0's. One is an Im, for which the confidence of our counterrotation claim is $\sim 2.2\sigma$. Full details appear in Kannappan & Fabricant (2001a). We stress that our detections represent a lower limit, because we cannot separate multiple kinematic components.

2.5.4 Discussion

Bertola et al. (1992) and Kuijken et al. (1996) find gas-stellar counterrotation frequencies of ∼20–25% for emission line S0's. We find 14(18)% with(without) the 3 uncertain S0's. This agreement, despite a strong difference in sample luminosity dis-

‡Kannappan, S. K. & Fabricant, D. G. 2000, PASP Conf. Series Vol. 230, 447, in press

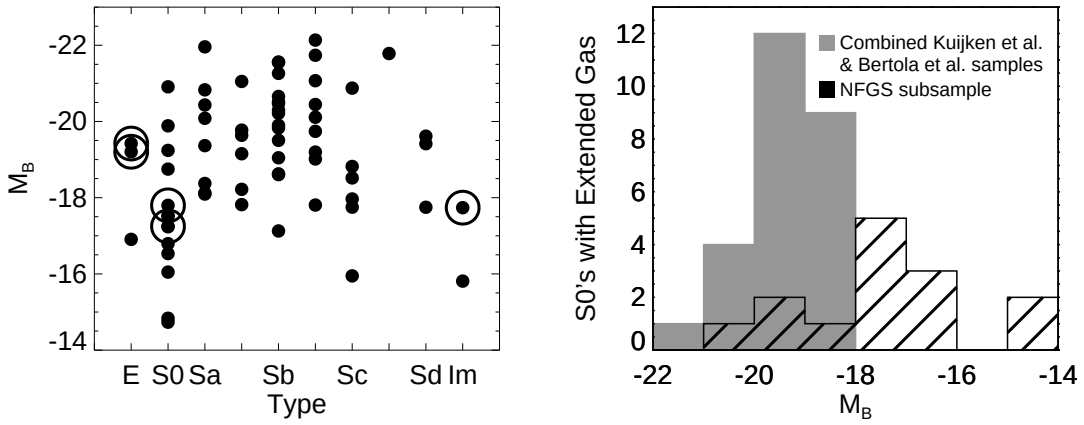

Figure 2.5.— Left: The search sample, with counterrotators circled. Right: Luminosity distributions for the 14 S0's in our sample and for the Bertola et al. (1992) and Kuijken et al. (1996) studies.

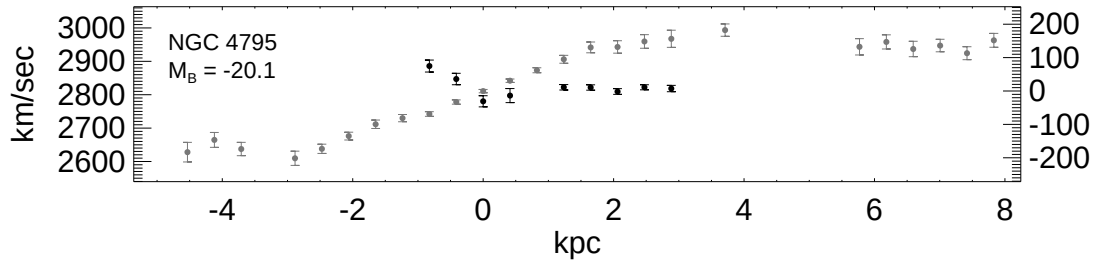

Figure 2.6.— Gas (black) and stellar (grey) kinematics for NGC 4795.

tributions (Figure 2.5), suggests that similar mechanisms form gas rich S0's over a wide range of physical scales.

Among 38 Sa–Sbc spiral galaxies, we find no clear cases of bulk counterrotation, implying a counterrotation frequency of <8% (95% confidence). However, counterrotation cannot be ruled out in the inner parts of one Sa (NGC 4795). This galaxy shows clear evidence of gas-stellar decoupling at large radii (Figure 2.6), possibly related to satellite accretion. Jore (1997) finds a bulk counterrotation frequency of ∼17% in a sample of 23 bright Sa's, consistent with our results given our Sa sample size of 8 (see also Haynes et al., 2000).

As argued in Kannappan & Fabricant (2001a), mergers and accretion provide the simplest explanation for the counterrotators' properties, particularly their early type morphologies, significant HI masses, and lack of obvious close neighbors. The signatures of minor retrograde accretion events may be washed out in gas rich spirals, while more substantial mergers are likely to produce E/S0/Sa galaxies. Dwarf-dwarf mergers may help to explain the faint S0 population.

Rolf Jansen generously provided his data and assisted us in using it. Norm Grogin kindly calculated local galaxy densities for us. Nelson Caldwell, Marijn Franx, and Lars Hernquist made helpful suggestions. Finally, Betsy Barton, Barbara Carter, Emilio Falco, Martha Haynes, John Huchra, Bob Kirshner, Douglas Mar, Hans-Walter Rix, and Aaron Romanowsky all provided information or resources for which we are extremely grateful. S. J. K. acknowledges support from a NASA GSRP Fellowship.

Chapter 3

Rotation Curve Asymmetries†

†includes excerpts from Kannappan, S. K. & Fabricant, D. G. 2000, PASP Conf. Series Vol. 230, 449, in press

ABSTRACT

We analyze asymmetries in the gas rotation curves of 151 galaxies drawn from the Nearby Field Galaxy Survey, spanning a broad range of luminosities and morphologies. If the origin of the rotation curve is chosen to minimize the asymmetry, then 21% of the Sa-Sd spirals with inclination greater than 40° show rotation curve asymmetries greater than 5%. Asymmetries increase both for lower inclinations and for non-spiral morphologies. We stress that rotation curve asymmetries arise from multiple sources, and not all gas kinematic asymmetries indicate asymmetries in the gravitational potential.

3.1 Introduction

Roughly 50% of bright spiral galaxies show asymmetry in their global HI profiles (Haynes et al., 1998). Such asymmetries may arise from noncircular motions, lopsided gas distributions, or unresolved companions. By examining resolved optical rotation curves (RC's), we can isolate the kinematic contribution to the asymmetry. Although optical RC's do not extend as far as *resolved* HI data, Courteau (1997) points out that global HI profiles sample primarily the kinematics of the inner disk, and high quality optical data generally perform equally well.

Our sample consists of 151 emission-line galaxies drawn from the Nearby Field Galaxy Survey (NFGS, Jansen et al., 2000b; Kannappan et al., 2001c), whose 196 galaxies were selected to represent the local galaxy population without any explicit bias in morphology or inclination over a wide range of luminosities, $-15 > M_B > -23$. The subsample analyzed here includes 151 of the 153 NFGS galaxies for which we have resolved gas RCs, omitting only two galaxies for which measuring RC asymmetry by our technique is not possible.

3.2 Asymmetry Measurement Technique

We adopt a quantitative measure of RC asymmetry akin to the photometric asymmetry index of Abraham et al. (1996). Reflecting the rotation curve about its origin, we compute the asymmetry as the average absolute deviation between the two sides, $<| v - v^{\rm reflected} |>$.

Measured RC asymmetries depend critically upon the choice of origin, so we shift both the spatial and velocity coordinates of the origin to numerically minimize the

asymmetry. We constrain the spatial coordinate of the origin to remain within the one-sigma error bars of our determination of the continuum peak position, but we allow the velocity coordinate to vary freely. To partially standardize our asymmetry measurements, we perform this minimization using only the inner RC, with radius less than $1.3r_e$ (the radius at which a pure exponential disk reaches peak velocity, Freeman, 1970). The total RC asymmetry (averaged over the entire RC) is then computed with respect to the origin determined by minimizing the inner RC asymmetry. We express the total RC asymmetry as a percentage of the velocity width $2V$ (using the V_{pmm} measure of Kannappan et al., 2001b).

3.3 Results

Figure 3.1 shows the distribution of the present sample in morphology and luminosity (uncorrected for internal extinction), within the context of the NFGS. Galaxies with total RC asymmetries greater than 5% are highlighted, representing 41% of the sample. Such galaxies are usually early type or very late type galaxies of low luminosity. However, within the spiral population, >5% asymmetries concentrate at the bright end of the luminosity distribution. The largest RC asymmetry we measure is 47%, for a peculiar galaxy strongly warped by an interaction (A14489+3547, Figure 3.2).

Figure 3.3 plots individual asymmetry values as a function of inclination in several bins, with the median value in each bin shown as a histogram-style horizontal line. RC asymmetries clearly increase for inclinations $i \lesssim 40$, presumably because turbulent motions perpendicular to the plane of the disk begin to dominate the observed kinematics. This trend partly explains why we see >5% asymmetries more often among bright spirals than among faint spirals: the brightest spirals have lower inclinations on average, as lower inclinations yield lower internal extinctions and higher apparent luminosity.

Limiting the sample to the 108 galaxies with $i > 40$, we find a clear trend in RC asymmetry as a function of morphology (Figure 3.4). On average, Sa–Scd spirals display total asymmetries of only ∼3–4%, while emission-line E/S0's and late-type Sd–Im galaxies display asymmetries of ∼6–13%. Emission-line E/S0's and Sd–Im galaxies tend to have low luminosity, so the observed morphology trend is also a luminosity trend (see also Kannappan et al., 2001b). Including galaxies with $i < 40$ weakens these trends, as face-on turbulence becomes more significant.

Rubin et al. (1999) argue that Virgo cluster spirals on radial orbits through the cluster core have a higher rate of rotation curve disturbances (judged by eye) than

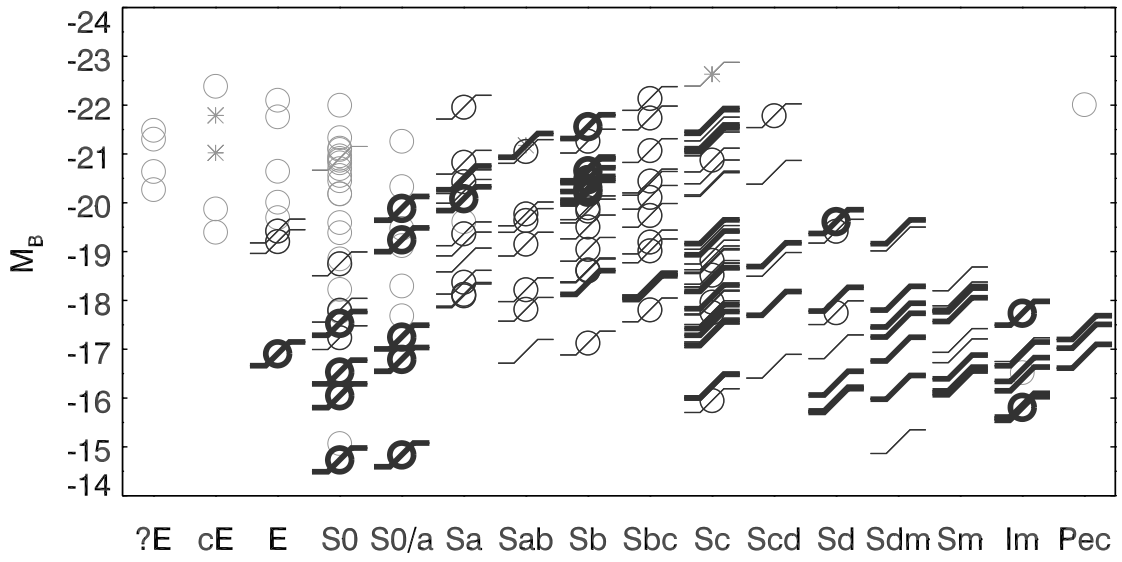

Figure 3.1.— Distribution of the sample by morphology and B-band luminosity. A circular symbol indicates that the NFGS database has stellar absorption line data for the galaxy, while an S-shaped symbol indicates that the database has extended gas emission line data and a star indicates a strong AGN. The asymmetry analysis sample consists of the 151 galaxies shown with a black S-shaped symbol. Galaxies with total asymmetry >5% are highlighted in thick black. Gray symbols represent NFGS galaxies not included in the asymmetry analysis sample.

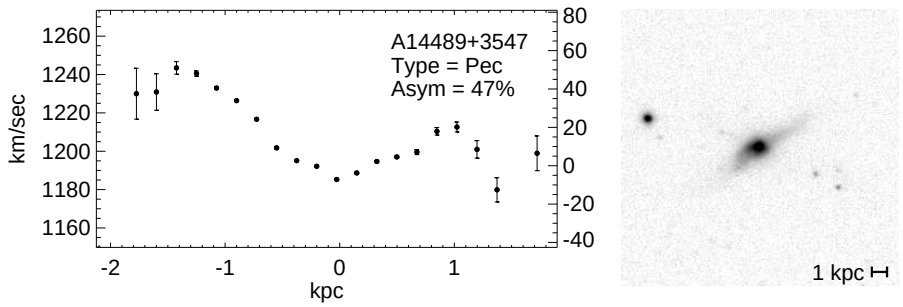

Figure 3.2.— Gas RC for the sample galaxy with the largest RC asymmetry.

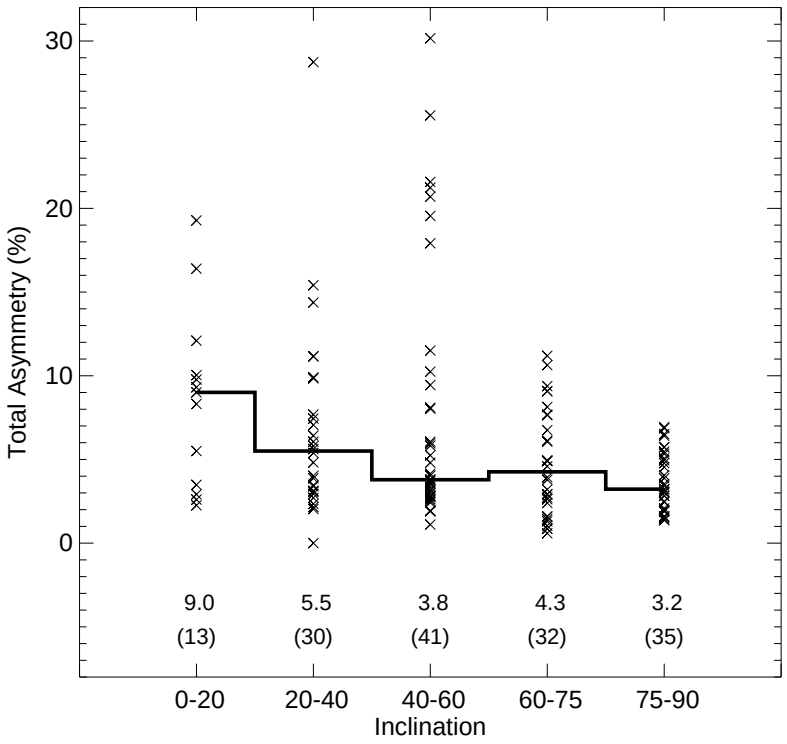

Figure 3.3.— Total RC asymmetries as a function of inclination. X's show individual asymmetry values, except for two off-scale asymmetries (37% in the i = 20–40 bin and 47% in the i = 75–90 bin). Horizontal lines connect the median values in each bin.

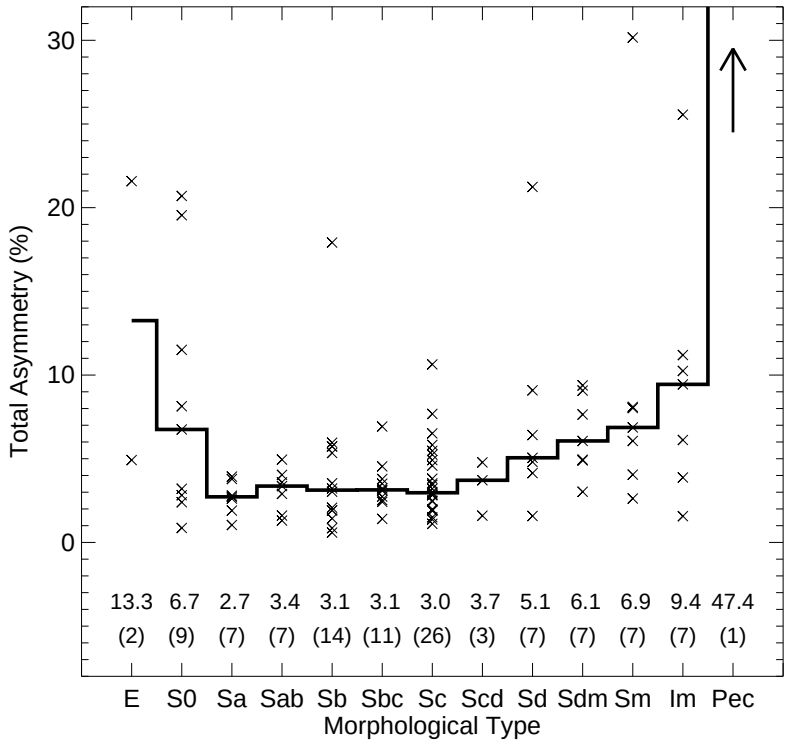

Figure 3.4.— Total RC asymmetries as a function of morphology for galaxies with $i > 40$. X's show individual asymmetry values, except for one off-scale asymmetry (47% in the Pec bin). Horizontal lines connect the median values in each bin.

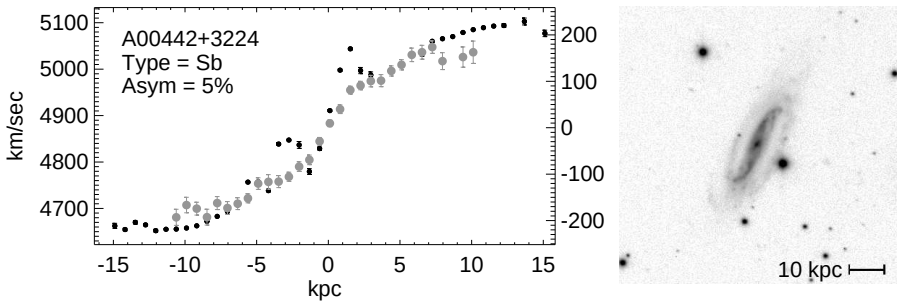

Figure 3.5.— Gas and stellar RCs for a barred Sb, represented by small black dots and large gray dots respectively.

other Virgo spirals, suggesting that galaxy interactions and rotation curve disturbances are linked. However, it remains an open question whether the morphology and luminosity trends in the NFGS reflect the relative frequency of galaxy interactions for different morphological types; these trends may also reflect variations in internal dynamics or in gas infall rates for different galaxies. To address this question, a study is currently in progress to compare RC asymmetries for the NFGS with RC asymmetries for a sample of galaxies in close pairs (E. Barton, private communication).

Although 41% of the galaxies in our full sample have asymmetries >5%, only 21% of the Sa–Sd spirals with $i > 40$ have asymmetries that high. Furthermore, some of the asymmetries we see reflect peculiar gas dynamics with no stellar counterpart, as illustrated in Figure 3.5. Thus the fraction of spiral galaxies with asymmetric gravitational potentials is probably quite a bit smaller than 21%. The frequency of significant RC asymmetries in NFGS spiral galaxies appears to be lower than the frequency of significant HI profile asymmetries in the spirals of Haynes et al. (1998), consistent with the idea that we are isolating kinematic asymmetries from lopsidedness in the HI distributions. However, direct comparison is difficult given the differences in asymmetry measurement technique. A calibration of the two techniques on a common sample would be useful.

We thank R. Jansen for sharing the NFGS photometry. S. J. K. received support from a NASA GSRP Fellowship.

Chapter 4

Physical Sources of Scatter in the Tully-Fisher Relation†

†Kannappan, S. K., Fabricant, D. G., & Franx, M.

ABSTRACT

We analyze residuals from the Tully-Fisher relation for emission-line galaxies in the Nearby Field Galaxy Survey, a broadly representative survey of the local galaxy population designed to fairly sample the full range of galaxy morphologies and environments for luminosities from $M_B = -15$ to -23. For a subsample consisting of spirals brighter than $M_R^i = -18$, we find strong correlations between Tully-Fisher residuals and both $B-R$ color and EW(Hα). The extremes of the correlations are populated by Sa galaxies, which show consistently red colors, and spirals with morphological peculiarities, which are often blue. If we apply an EW(Hα)-dependent or $B-R$ color-dependent correction term to the Tully-Fisher relation, the scatter in the relation no longer increases from R to B to U but instead drops to a nearly constant level in all bands, close to the scatter we expect from measurement errors. We argue that these results probably reflect correlated offsets in luminosity and color as a function of star formation history. Broadening the sample in morphology and luminosity, we find that most non-spirals brighter than $M_R^i = -18$ follow the same correlations between Tully-Fisher residuals and $B-R$ color and EW(Hα) as do spirals, albeit with greater scatter. However, the correlations do not apply to galaxies fainter than $M_R^i = -18$ (dwarfs) or to emission-line S0 galaxies with anomalous gas kinematics. Tully-Fisher residuals for the dwarf population correlate with other physical properties: dwarfs that are overluminous for their velocity widths are more disturbed than underluminous dwarfs, with higher rotation curve asymmetries, brighter U-band effective surface brightnesses, and shorter gas consumption timescales. As a result, the measured slope of the Tully-Fisher relation at low luminosities depends upon how the sample is selected. If we limit the sample at all luminosities to include only passively evolving, rotationally supported galaxies, then only the underluminous dwarfs are included and we find a break toward steeper slope at low luminosity. However, the dwarfs in the complete Ursa Major sample of Verheijen & Sancisi (2001) define a shallower slope, occupying the Tully-Fisher locus of our more disturbed dwarfs; this result offers clues to the origin of the Ursa Major dwarfs.

4.1 Introduction

The tight correlation between luminosity and rotation velocity for spiral galaxies, a.k.a. the Tully-Fisher relation (TFR, Tully & Fisher, 1977), has motivated dozens of studies over the years. In pursuit of the best possible distance indicator, most TF analyses have been carried out in red or infrared passbands (see reviews by Strauss & Willick, 1995; Jacoby et al., 1992), which offer lower scatter than bluer passbands.

However, recent theoretical work has emphasized the value of studying TF scatter for its own sake, as this scatter holds fundamental clues to the formation and evolution of galaxies (e.g. Buchalter et al., 2001a; Elizondo et al., 1999; Eisenstein & Loeb, 1996). Observations in bluer passbands are ideal for understanding TF scatter, because the scatter arising from recent star formation, differences in stellar populations, and the spread in formation redshifts is most visible in the blue.

Physical scatter in the TFR can come from three sources: (1) variations in the stellar mass-to-light ratio, (2) variations in the stellar mass fraction (stellar-to-total mass ratio), and (3) differences in how the observed velocity width relates to the total mass. By identifying physical scatter from any one of these sources we limit the contributions of the other two, simultaneously gaining insight into the star formation histories of galaxies, the relationship between visible galaxies and dark matter halos, and the dynamics and structure of galaxy disks.

A better understanding of the sources of TF scatter may also minimize uncertainties in other types of TF analyses. For example, if TF slope varies with environment or if TF zero point varies with color, then a cluster TFR calibrated with a small set of galaxies with Cepheid distances may not be universal (e.g. Tully & Pierce, 2000; Sakai et al., 2000). Correcting for these systematics could reduce scatter and improve the TFR as a distance indicator. Calibrating zero point shifts as a function of color and emission line strength could also aid in the interpretation of evidence for luminosity evolution in the intermediate-redshift TFR (Simard & Pritchet, 1998; Vogt et al., 1997).[1]

Here, we use a well-defined sample of emission-line galaxies drawn from the 196-galaxy Nearby Field Galaxy Survey (NFGS, Jansen et al., 2000b; Kannappan et al., 2001c) to examine how offsets from the U, B, and R-band TFRs depend upon the physical properties of galaxies. While previous TF studies have often included hundreds or thousands of galaxies (e.g. Aaronson et al., 1982; Pierce & Tully, 1992; Mathewson et al., 1992; Willick et al., 1996; Giovanelli et al., 1997a; Courteau, 1997; Sakai et al., 2000; Tully & Pierce, 2000), none of these data sets has both the broadly representative sample demographics and the wide array of supporting data of the NFGS (§4.2). Thus despite its modest size, the present survey offers unique advantages for studying scatter in the TFR.

The bulk of this paper analyzes a sample of NFGS galaxies consisting of $\sim$70 Sa–Sd spirals brighter than $M_R^i = -18$. This spiral sample allows us to investigate the behavior of galaxies often excluded from the TFR: Sa galaxies and galaxies with

[1]We recalibrate evidence for luminosity evolution in the intermediate-z TFR in a companion paper, Kannappan et al. (2001a).

peculiarities such as warps, multiple nuclei, or interacting companions. Ultimately, we seek to fit these galaxies into a unified picture, in which we understand TF residuals in terms of continuous physical properties. To this end we undertake a detailed analysis of third-parameter correlations with TF residuals, and we attempt to form a physical understanding of TF scatter.

The remainder of the paper draws from the full NFGS to define an extended sample of ∼110 galaxies including very late types, emission-line E/S0 galaxies, and faint dwarfs. The extended sample allows us to search for physical drivers of TF scatter in a heterogeneous population. The only other comparable TF sample is the ∼40-galaxy Ursa Major sample of Verheijen & Sancisi (2001), which was drawn from a restricted environment. The Virgo and Fornax cluster samples of Yasuda et al. (1997) and Bureau et al. (1996) apply morphology restrictions that exclude irregular or interacting galaxies. Although some intermediate-redshift TF analyses have included a wide range of morphologies (Rix et al., 1997; Forbes et al., 1996; Simard & Pritchet, 1998), these studies nonetheless favor a select population: typically, moderately bright blue galaxies with strong emission and high surface brightness. And although the samples studied by Pierini & Tuffs (1999) and McGaugh et al. (2000) both span large ranges in luminosity, the former study is restricted by Hubble type and evidence for interaction, while the latter study is drawn from a heterogeneous mix of smaller samples selected by various criteria in different photometric bands. The NFGS thus provides an unusually broad and unbiased representation of the general galaxy population.

In what follows, we describe the survey and our data reduction and analysis techniques (§4.2–4.5), then present results for the spiral sample (§4.6–4.8) and for the extended sample (§4.9). We summarize our major conclusions in §4.10.

4.2 The Nearby Field Galaxy Survey

The comprehensive nature of the Nearby Field Galaxy Survey (NFGS) enables us to analyze how TF scatter depends on a broad range of galaxy properties. The database includes UBR photometry, integrated and nuclear spectrophotometry, and gas and stellar kinematic data for a representative sample of the local galaxy population (Jansen et al., 2000a,b; Kannappan et al., 2001c). Jansen et al. (2000b) selected the 196-galaxy sample from the CfA 1 redshift survey (Huchra et al., 1983) without preference for morphology, color, diameter, inclination, environment, or any other galaxy property. To counteract the bright galaxy bias of CfA 1, galaxies were included approximately in proportion to the local B-band galaxy luminosity function (LF, e.g.

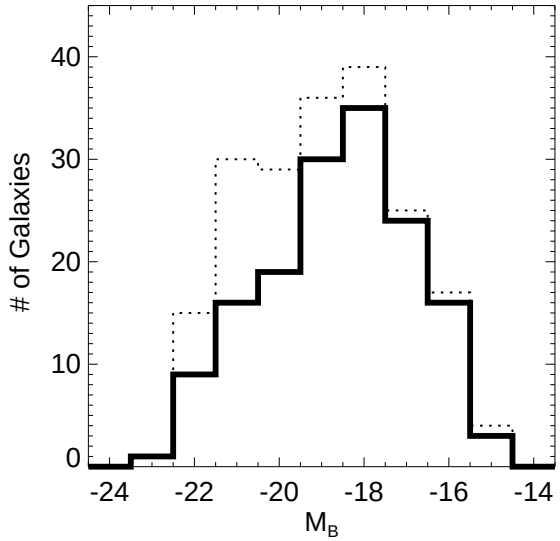

Figure 4.1.— Luminosity distribution for the Nearby Field Galaxy Survey, using B-band CCD magnitudes from the NFGS database (Jansen et al., 2000b) converted to H_0=75. The dotted line shows the full NFGS and the solid line shows the 153 galaxies with extended ionized gas emission (optical rotation curves).

Marzke et al., 1994), with the final sample spanning luminosities from $M_B \sim -23$ to -15.

The resulting sample provides an unusually unbiased sampling of the general galaxy population. However, no sample is completely free of selection effects. The NFGS is subject to the inherent color and surface brightness biases of the parent CfA 1 survey, itself a descendent of the Zwicky catalog and therefore essentially B-selected.

The NFGS also suffers from residual luminosity bias, despite the attempt to favor faint galaxies in the selection process. Figure 4.1 shows that the sample luminosity distribution provides decent statistics in the range $-16 > M_B > -22$ but cuts off for brighter and fainter galaxies. In addition, a subtle luminosity bias may arise because of the luminosity-distance correlation built into the NFGS. The survey was selected with a luminosity-dependent lower redshift limit instead of a maximum diameter limit, in order to increase the odds that galaxies would fit on the spectrograph slit without biasing the sample in diameter. As a result, fainter galaxies have greater fractional uncertainties in distances and absolute magnitudes, and such galaxies receive less weight in error-weighted TF fits. For this reason, we adopt unweighted fits as our primary fitting technique (see §4.5 for a discussion of the differences between techniques).

4.3 Velocity Width Data

Our primary velocity widths are derived from the full set of 153 major-axis ionized gas rotation curves (RCs) obtained for the NFGS kinematic database (Kannappan et al., 2001c). This sample is complete in the sense that kinematic observations were attempted for all NFGS galaxies; however, emission line detection limits varied with observing conditions, integration times, and available emission lines (see §4.3.1). Figure 4.2 displays the emission line properties of the optical RC sample in the context of the NFGS as a whole.

As illustrated in Figure 4.3, the optical RC sample includes all NFGS galaxies of type Sab and later (including type "Pec" galaxies), except for one Magellanic irregular galaxy and the BL-Lac Markarian 421,[2] both of which show largely featureless spectra. In addition, the sample includes 12 of the 13 Sa's in the NFGS and 17 of the E/S0's.

For comparison with the optical data, we have also extracted HI 21-cm linewidths for 105 NFGS galaxies from the catalogs of Bottinelli et al. (1990) and Theureau et al. (1998). These galaxies are *not* a fair sampling of the NFGS in luminosity; HI measurements are missing for many of the brighter, more distant galaxies (see Figure 4.4). We exclude from analysis one galaxy that has HI data but no optical RC (NGC 2692, an Sa galaxy).

The NFGS includes galaxies at all inclinations i, but $\sin i$ corrections are uncertain for galaxies with $i < 40$, so most of our analysis considers only the 108 NFGS emission-line galaxies with $i > 40$. However, we do not restrict inclinations when calibrating optical-to-radio conversions (§4.3.3), because no inclination correction is required.

4.3.1 Optical Rotation Curve Observations

Long slit spectra were obtained during several observing runs between 1996 and 1999, using the FAST spectrograph on the Tillinghast Telescope (Fabricant et al., 1998). For most galaxies we observed the Hα, [NII], and [SII] lines between ∼6200–7200 Å, with spectral resolution $\sigma \sim 30$ km s^{-1}, a 2" or occasionally 3" wide slit, and a spatial binning of 2.3 arcseconds/pixel (comparable to the typical seeing of 2"). For some galaxies, in conjunction with stellar absorption line observations, we also observed the Hβ and [OIII] emission lines between ∼4100–6100 Å, again with 2.3 arcseconds

[2]Markarian 421 is not a true late type. It was assigned type "Pec" in the NFGS, but its host galaxy is probably an elliptical. The other three type "Pec" galaxies in the NFGS are true late types.

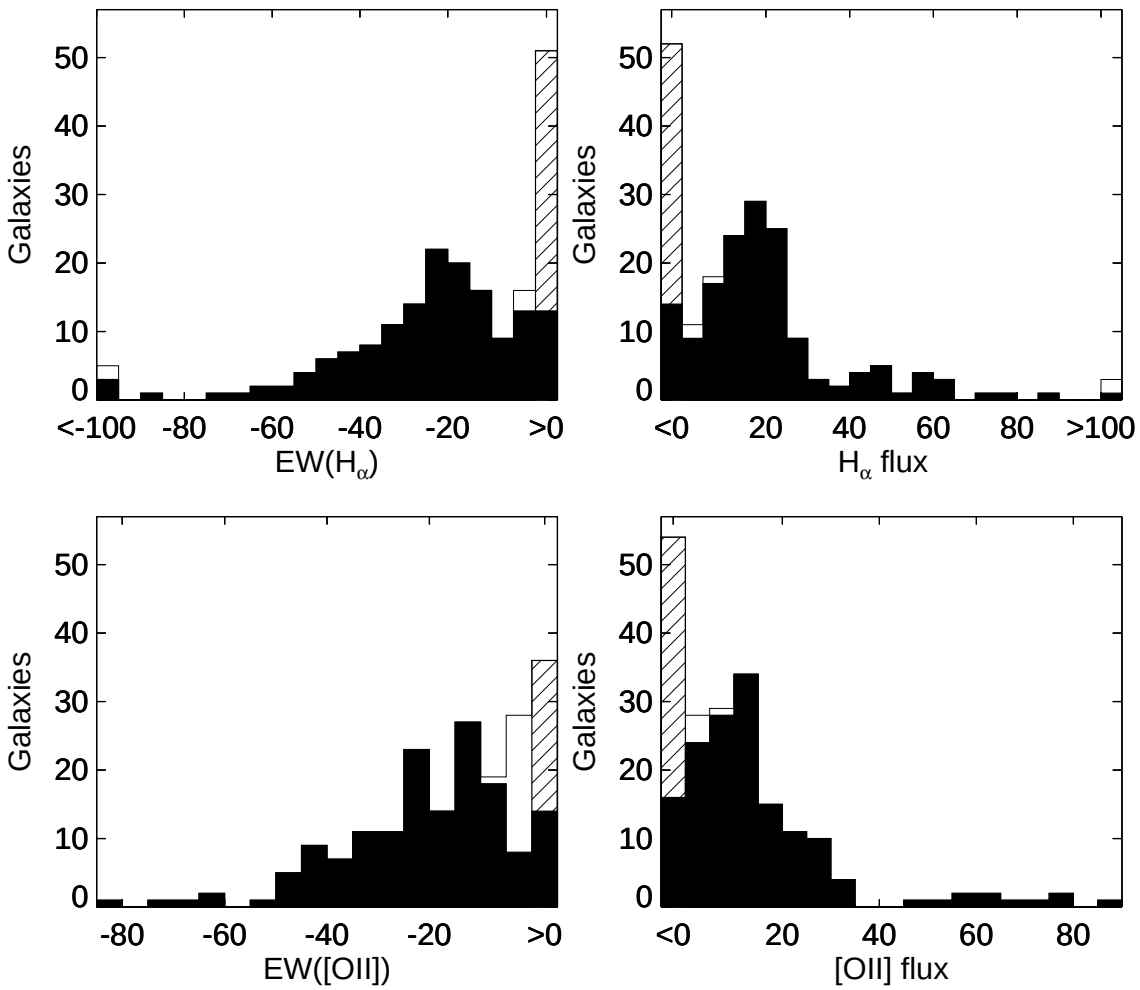

Figure 4.2.— Detection of extended emission (rotation curves) as a function of emission line strength. Left panels: Hα and [OII] 3727 equivalent widths for the entire NFGS (outline) and for the 153-galaxy optical RC sample (solid). Right panels: Calibrated line fluxes in the same format. Cross-hatched bins represent all galaxies for which the integrated spectrophotometry indicates lines in absorption; with the higher resolution kinematic data we can detect extended emission in a number of these galaxies. Hα fluxes/equivalent widths brighter than 100/-100 are shown with values of 100/-100 to limit the axis range. Galaxies with strong Hα emission but no rotation curve are AGNs. We use equivalent widths from the NFGS database (Jansen et al., 2000a) and fluxes courtesy of R. A. Jansen (private communication).

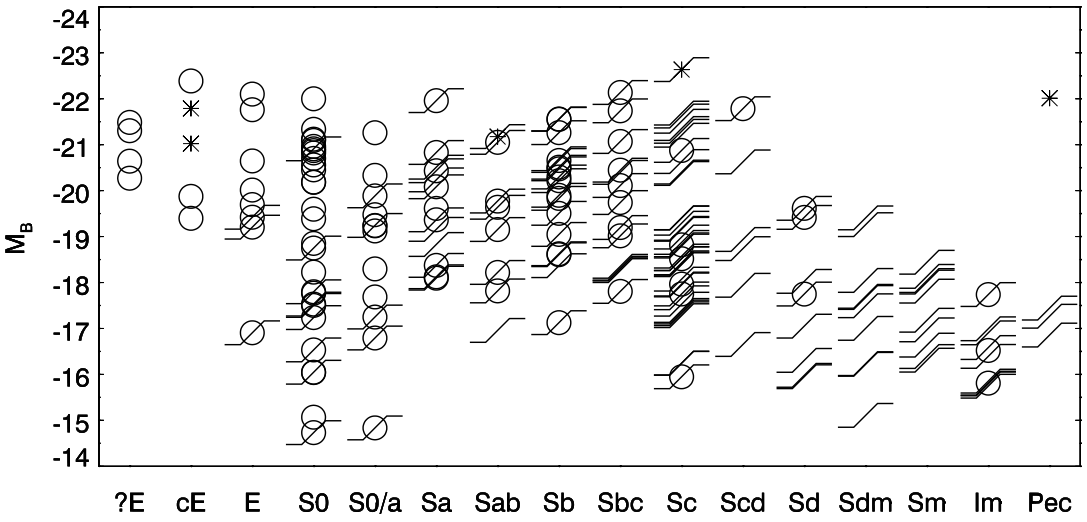

Figure 4.3.— An overview of the Nearby Field Galaxy Survey, showing the demographics of all 196 galaxies sorted by morphology and B-band luminosity. A circular symbol indicates that we have stellar absorption line data for the galaxy, while an S-shaped symbol indicates that we have extended gas emission line data. The optical RC sample consists of the 153 galaxies shown with an S-shaped symbol. Strong AGNs are marked with a star.

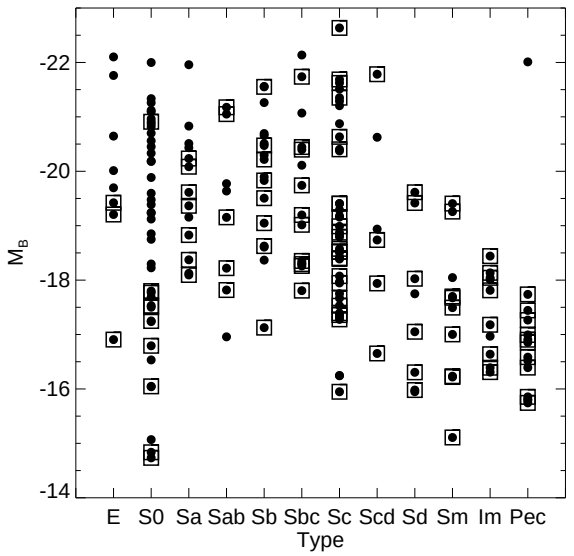

Figure 4.4.— Distribution of NFGS galaxies in luminosity and morphology, with boxes around the galaxies for which we have obtained HI linewidths from the catalogs of Bottinelli et al. (1990) and Theureau et al. (1998).

spatial binning and a 2" slit, but with reduced spectral resolution, $\sigma \sim 60$ km s^{-1}. These lower resolution observations serve as the primary emission line data for 10 galaxies for which we lack high resolution observations.

The alignment between the slit position angle and the galaxy major axis position angle listed in the UGC (Nilson, 1973) was generally tight, ΔP.A. $< 6°$. For two galaxies the slit was severely misaligned (ΔP.A. $= 40°$ and $75°$). Also, a few galaxies had no UGC P.A. and were instead assigned P.A.'s based on visual inspection of the digitized POSS images; these galaxies have uncertain ΔP.A. All galaxies with large or uncertain ΔP.A. have photometric inclination $i < 40$ and so are automatically excluded from our TF samples. In §4.3.3, where we do not employ an inclination restriction, we explicitly exclude galaxies with large or uncertain ΔP.A.

All of the data were reduced using standard methods, including bias and dark subtraction, flat-fielding, wavelength calibration, heliocentric velocity correction, sky subtraction, spectral straightening, and cosmic ray removal, using IRAF and IDL.

We extracted rotation curves by fitting all available emission lines simultaneously with fixed line spacing in $\log \lambda$, rejecting fits with S/N $\lesssim 3$. In cases of severe Hα or Hβ absorption, these lines were omitted from the fits. Further details are given in Kannappan et al. (2001c).

4.3.2 Rotation Curve Asymmetry Measurements

We compute asymmetries in the optical rotation curves using a technique similar to the photometric technique of Abraham et al. (1996). Reflecting the rest-frame rotation curve about its origin, we find the average absolute deviation between the two sides, $<| v - v^{\rm reflected} |>$, and express the result as a percentage of the velocity width $2V_{pmm}$ (§4.3.3.3).[3]

Asymmetry measurements depend sensitively on the choice of origin for the spatial and velocity axes. We therefore vary the position of the origin to minimize the asymmetry, keeping the spatial coordinate constrained within the one-sigma error bars of the continuum peak position, while allowing the velocity coordinate to vary freely. At each step in the minimization process we resample the rotation curve onto a uniform spatial grid about the trial origin.

To partially standardize our asymmetry index for rotation curves of differing

[3]Our asymmetry, velocity width, and central redshift measurements are not completely independent of one another, therefore in practice we perform these calculations iteratively with approximations in the initial round.

spatial extent, we define an inner asymmetry using only points within $1.3r_e$ (the peak velocity position for a pure exponential disk, where r_e is the effective radius; see §4.3.3.2). When the rotation curve does not extend this far, we compute the inner asymmetry from the data available. The rotation curve origin is determined by minimizing the inner asymmetry. All other analysis makes use of the total asymmetry, which we compute relative to the origin defined by minimizing the inner asymmetry.

4.3.3 Velocity Width Definitions & Optical-To-Radio Conversions

Except when comparing our data with other studies that employ optical rotation curves, we convert both optical and radio velocity width measures to an equivalent W_{50} linewidth scale. For galaxies with W_{20} but no W_{50} in the catalog, we simply subtract 20 km s^{-1} from the W_{20} linewidths and use the adjusted W_{20}'s together with the W_{50}'s, referring to the combined data set as W_{HI}. The number 20 km s^{-1} comes from a comparison of W_{20} and W_{50} where we have both measures; Haynes et al. (1999) derive a similar value from a much larger sample. However, our data show considerable scatter around the 20 km s^{-1} value, so to calibrate the optical velocity widths to the W_{50} scale we use only the W_{50} data.

In §4.3.3.1–4.3.3.3 we present three different optical velocity width definitions (V_{max}, V_{fit}, and V_{pmm}) and place them on an equivalent W_{50} scale. Except when comparing with Courteau (1997), we adopt the W_{50}-equivalent velocity width $W_{V_{pmm}}$ as our primary optical velocity width measure. Our optical-to-radio conversions are expected to differ from those of Courteau, not just because of differences in sample selection, but also because Courteau's conversions are calibrated using turbulence-corrected HI linewidths (taken from Giovanelli et al., 1997b). In our case, the conversions are calibrated using uncorrected HI linewidths.

Note that all optical velocity widths are computed from rest-frame rotation curves, so no additional correction for cosmological stretch is necessary. HI linewidths are corrected for cosmological stretch by dividing by $(1 + z)$.

4.3.3.1 V_{max}

We define V_{max} as the single largest velocity in the rotation curve, relative to the origin defined by minimizing the asymmetry (§4.3.2). Because this number does not make use of the full information in the rotation curve, we expect it to be somewhat unreliable. We do not use V_{max} in what follows, but include it only for comparison

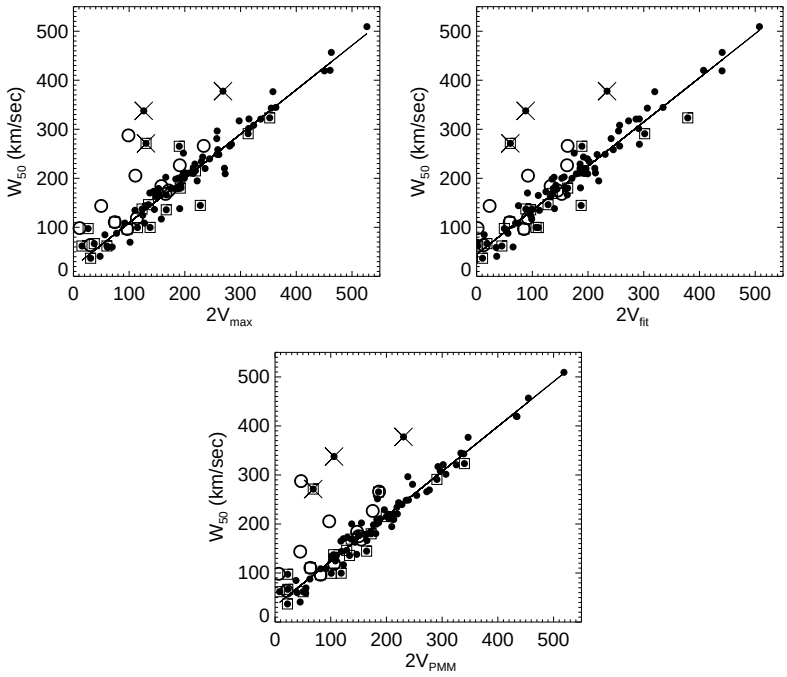

Figure 4.5.— W_{50} versus V_{max}, V_{fit}, and V_{pmm} for the 96 galaxies with both optical RC and HI W_{50} velocity widths. Boxes indicate points for which the optical rotation curve does not extend to $1.3r_e$; remarkably, these points show no strong deviation from the general correlation. Lines indicate least squares fits to the data (§4.3.3), with automatically rejected points ($>3.5\sigma$) marked by an X. All three X's represent galaxies currently interacting with another galaxy: NGC 4795, NGC 7752, and NGC 2799. The open-circle points mark galaxies with potentially large position angle misalignment in the optical RC data (§4.3.1); these are also excluded from the fit. The zero point offset indicates the nonzero contribution of turbulence to the HI profiles even at zero rotation velocity.

with the other two velocity width definitions. Nonetheless, it correlates surprisingly well with the radio linewidth W_{50} (Figure 4.5), even when the optical RC does not extend as far as $1.3r_e$ (the peak velocity position for an exponential disk, see §4.3.3.2). An iterative least-squares fit with automatic 3.5σ outlier rejection yields

$$W_{50} = 19\,(\pm 6) + 0.90\,(\pm 0.03)\,(2V_{\rm max}) \tag{4.1}$$

with scatter 25 km s^{-1}.

4.3.3.2 V_{fit}

Following Courteau (1997), we define V_{fit} by first fitting the empirical function

$$v = v_0 + v_c \frac{(1+x)^\beta}{(1+x^\gamma)^{1/\gamma}} \tag{4.2}$$

to the observed RC, with the origin unconstrained, and then interpolating to find the velocity at a specific radius. Here $x = r_t/(r - r_0)$, (r_0, v_0) defines the origin, v_c gives the velocity scale, r_t is related to the turnover radius, and γ and β are free parameters governing the shape of the rotation curve. We modify Courteau's technique slightly, in that we interpolate the velocity V_{fit} at $1.3r_e$ rather than at 2.2 disk scale lengths r_d, because $1.3r_e$ remains well defined even for non-disk galaxies and does not require bulge+disk decomposition. Theoretically the two radii are equivalent, in that both represent the peak velocity position for a pure exponential disk (Freeman, 1970). For disk-dominated galaxies in the NFGS, $1.3r_e$ and $2.2r_d$ also match well observationally. (Disk scale lengths are courtesy of R. Jansen, private communication; both disk scale lengths and r_e's are from the B band images of Jansen et al. (2000b).)

As illustrated in Figure 4.6, our modified-Courteau technique sucessfully models bright spiral galaxies similar to those in Courteau's sample, but sometimes fails when confronted with the full variety of rotation curve shapes in our sample. Figure 4.5 shows the correlation of V_{fit} with radio linewidth W_{50}, demonstrating reasonable agreement, although some points are simply missing because the fit would not converge. An iterative least-squares fit with automatic 3.5σ outlier rejection yields

$$\mathrm{W}_{50} = 45\,(\pm 5) + 0.90\,(\pm 0.03)\,(2\mathrm{V}_{\mathrm{fit}})\,. \tag{4.3}$$

We define the equivalent W_{50} linewidth $\mathrm{W}_{V_{fit}}$ by this equation and assign it an error equal to the scatter in the fit, 25 $\mathrm{km\,s^{-1}}$.

4.3.3.3 V_{pmm}

Following Raychaudhury et al. (1997), we define V_{pmm} as half the difference between the statistical "probable maximum" and "probable minimum" velocities implied by the observed rotation curve. The probable maximum velocity v_{pmax} is defined to have a 10 percent chance of exceeding all velocities in the rotation curve:

$$\prod_i P\,(v_{pmax} > v_i) = 0.1. \tag{4.4}$$

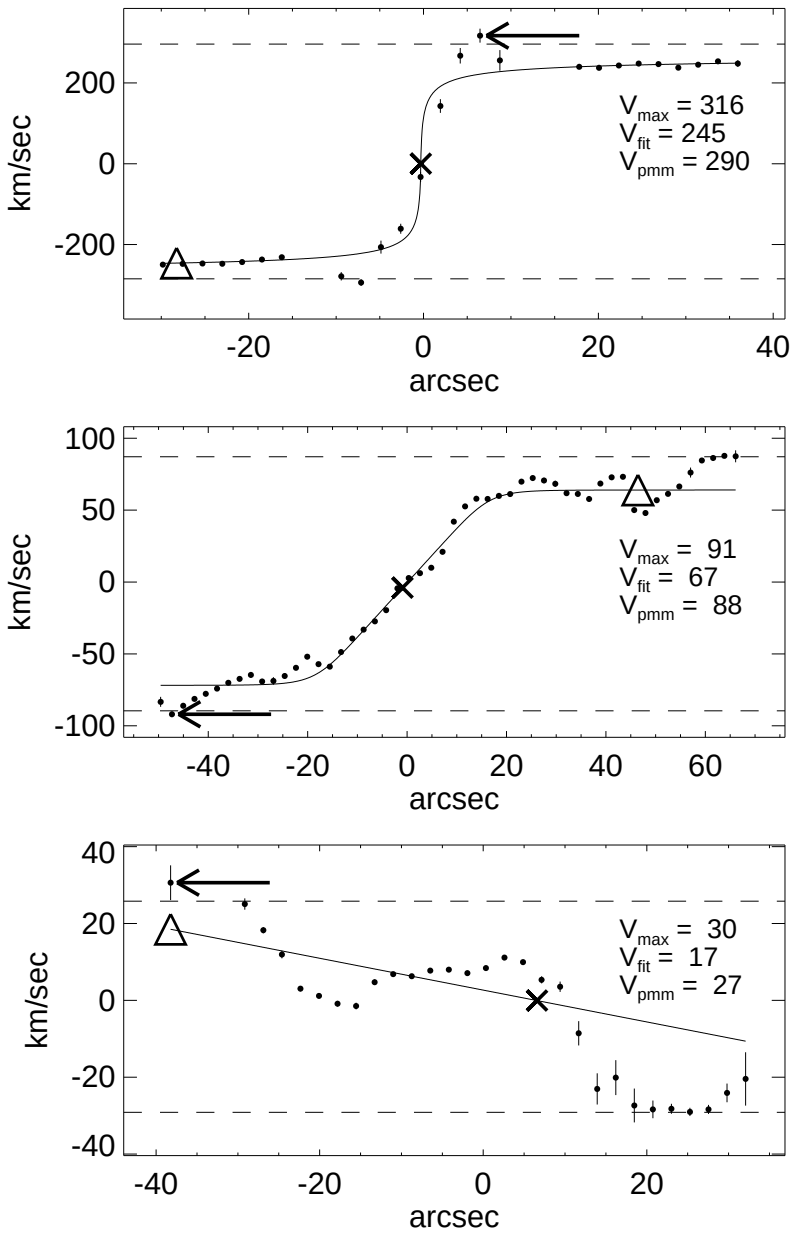

Figure 4.6.— Comparison of optical velocity width definitions. The data are dered-shifted with respect to the origin determined by asymmetry minimization (§4.3.2), and the arrow marks the largest velocity with respect to that origin, defined as V_{max}. The two dashed lines indicate the probable minimum and maximum velocities, with half the difference between the two equalling V_{pmm} (independent of origin). The solid line shows a functional fit to the data (§4.3.3.2) with origin unconstrained; an X marks the resulting origin and an open triangle marks the point defined as V_{fit}.

Modeling each velocity v_i as a Gaussian distribution about the measured value, with σ equal to the measurement error, we obtain

$$\prod_i \left(\frac{1}{2} + \frac{1}{2} \mathrm{erf} \frac{v_{pmax} - v_i}{\sqrt{2}\sigma_i} \right) = 0.1, \tag{4.5}$$

which may be solved numerically for v_{pmax}. The probable minimum velocity v_{pmin} is defined by analogy, and $2V_{pmm} = v_{pmax} - v_{pmin}$.

Courteau (1997) suggests that V_{pmm} will be very sensitive to outlying points in the rotation curve, while Raychaudhury et al. (1997) claim the opposite. The difference seems to hinge on the size of the error bars associated with the outliers — if a high S/N cosmic ray hit masquerades as a very high-velocity data point, it may indeed throw off V_{pmm}, but outlying points with large error bars will have relatively little impact. In practice, V_{pmm} produces smaller scatter than V_{fit} in the optical-to-HI conversion. More importantly, as Raychaudhury et al. point out, V_{pmm} has the virtue of using all of the data in the rotation curve without imposing a specific model on the data. The diversity of the NFGS defies modeling through a simple fitting function (see previous section and Figure 4.6).

Figure 4.5 shows the correlation of V_{pmm} with radio linewidth W_{50}. An iterative least-squares fit with automatic 3.5σ outlier rejection yields

$$\mathrm{W}_{50} = 33\,(\pm 5) + 0.92\,(\pm 0.02)\,(2\mathrm{V}_{\mathrm{pmm}})\,. \tag{4.6}$$

We define the equivalent W_{50} linewidth $\mathrm{W}_{V_{pmm}}$ by this equation and assign it an error equal to the scatter in the fit, 20 km s^{-1}. $\mathrm{W}_{V_{pmm}}$ is our default optical velocity width measure.

4.3.4 Velocity Width Corrections & Errors

We correct for inclination by dividing by $\sin i$, denoting corrected velocity widths with a superscript i. Here

$$i = \cos^{-1} \sqrt{\left((b/a)^2 - q_0^2\right) / \left(1 - q_0^2\right)} \tag{4.7}$$

with i set to 90 whenever $b/a < q_0$, the assumed intrinsic minor-to-major axis ratio. We adopt $q_0 = 0.20$ except when comparing with Courteau (1997), in which case we use his value (0.18). Tests with a range of q_0's as well as an alternative "opaque slab" model for $\sin i$ determinations (R. Jansen, private communication) indicate that TF scatter is remarkably insensitive to the method of computing inclinations. The errors are propagated assuming errors in b and a equal to their measurement precision in the

UGC (typically 0.05–0.1 arcmin). We have checked the quality of the UGC estimates against estimates derived from both 2MASS data and NFGS CCD photometry (R. Jansen, private communication): the newer measurements do not improve TF scatter.

We do not apply turbulence corrections to either optical or radio velocity widths, except when calculating extinctions (see §4.4.2). Turbulence estimates are uncertain, and furthermore turbulence corrections may be inappropriate for small galaxies and non-equilibrium systems. In fact turbulence may provide an important source of support for such systems, and we might wish to *add* a gas pressure correction to the optical velocity widths, but our velocity resolution is inadequate to the task on a galaxy-by-galaxy basis. However, the conversion of optical velocity widths to an equivalent W_{50} scale (§4.3.3) effectively makes such a correction, averaged over the sample.

Barton et al. (2000a) suggest a correction formula for P.A. misalignment, based on an axisymmetric thin disk model. For our data, this misalignment correction actually increases TF scatter, probably partly because the finite-width slit of the observations is more forgiving than a theoretical zero-width slit, especially for edge-on galaxies, and partly because the reference P.A.'s are themselves uncertain. Simulations by Giovanelli et al. (1997b) indicate that slit misalignment effects remain negligible for ΔP.A. $< 15°$, and observational tests in the range ΔP.A. $< 8°$ confirm this result (Courteau, 1997). Taking the UGC as a reference, our alignments for galaxies with $i > 40$ are all within 6° (§4.3.1). Comparison between the UGC P.A.'s and corresponding automated P.A. measurements from 2MASS and POSS (Garnier et al., 1996) suggests typical deviations of under 15°, except for a few cases with large discrepancies, possibly due to the automation. Therefore the combined misalignment from observational mismatch and reference uncertainty should nearly always be within the range tested by Giovanelli et al. (1997b), and we choose to make no correction. However, an rms P.A. misalignment error term is *de facto* included in our errors, because we estimate the optical velocity width errors based on the scatter in the optical-to-radio conversion.

4.4 Luminosity Data

Extrapolated total B and R magnitudes are available in the NFGS photometry database (Jansen et al., 2000b) for all galaxies with optical RCs. In addition, Jansen et al. provide U-band magnitudes for all but two of the galaxies. The database magnitudes include corrections for galactic absorption and have typical errors of ∼0.02–0.03 mag.

4.4.1 Absolute Magnitudes

We compute absolute magnitudes using distances derived from a linear Hubble flow model with $H_0 = 75$. For consistency, we use the redshifts tabulated by Jansen et al. (2000b) and adopt their Virgocentric infall correction (from Kraan-Korteweg et al., 1984). Comparison with our newly measured redshifts indicates good agreement between the two sets of measurements ($\sigma \sim 35$ km s^{-1}) with a few outliers. In most cases the difference is $\lesssim 5\%$ of the galaxy's recession velocity, except for four nearby galaxies for which the fractional difference reaches $\sim$7–13%. Using our measurements does not affect TF scatter. We assign a redshift error of the greater of 35 km s^{-1} or the difference between the tabulated and newly measured redshifts and add this term in quadrature with an assumed peculiar velocity uncertainty of 200 km s^{-1}. These errors are propagated into the absolute magnitude errors.

4.4.2 Internal Extinction Corrections

Magnitudes corrected for internal extinction are denoted by a superscript i. Except when comparing with Courteau (1997), we adopt the velocity width-dependent (and thus implicitly luminosity-dependent) internal extinction corrections of Tully et al. (1998):

$$A_i^\lambda = \gamma_\lambda \log(a/b), \tag{4.8}$$

where a/b is the major to minor axis ratio and γ_λ is the extinction coefficient. Tully et al. measure γ_λ at B, R, and K':

$$\gamma_B = 1.57 + 2.75\left(\log W_R^i - 2.5\right), \tag{4.9}$$

$$\gamma_R = 1.15 + 1.88\left(\log W_R^i - 2.5\right), \tag{4.10}$$

$$\gamma_{K'} = 0.22 + 0.40\left(\log W_R^i - 2.5\right). \tag{4.11}$$

For the U band we use an extrapolated coefficient:

$$\gamma_U = 1.69 + 3.00\left(\log W_R^i - 2.5\right). \tag{4.12}$$

Here W_R is the velocity width on the turbulence-corrected scale of Tully & Fouque (1985):

$$W_R^2 = W_{20}^2 + W_t^2 - 2W_tW_{20}\left(1 - e^{-W_{20}^2/W_c^2}\right) - 2W_t^2 e^{-W_{20}^2/W_c^2} + 4W_{dwarf}^2, \tag{4.13}$$

where $W_t = 38$, $W_c = 120$, and $W_{dwarf} = 17$. Tully & Fouque introduce the last term to define a dynamical velocity width suitable for dwarf galaxies; it prevents

small linewidths from being "corrected" to square roots of negative numbers.[4] While we do not generally use turbulence corrections (see §4.3.4), we make an exception in this case for consistency with Tully et al., defining our equivalent W_{20} linewidths according to the empirical conversions given in §4.3.3.

Although the Tully et al. (1998) extinction corrections were derived for spiral galaxies, Pierini (1999) has shown that they perform well for dwarf galaxies. As prescribed by Tully et al., the extinction corrections are set to zero whenever they go negative, to avoid having the corrected luminosities come out fainter than the observed luminosities. For the same reason, the error bars on the corrected magnitudes do not extend fainter than the measurement errors on the observed magnitudes.

Courteau (1996), following Willick et al. (1996), uses an alternative correction formula with no velocity width or luminosity dependence, and Willick et al. further argue that there is no evidence for luminosity dependence in the residuals from their corrections. However, if we follow their procedure and apply a correction of the form $\gamma \log(a/b)$, where γ is a luminosity-independent constant to be chosen to minimize TF scatter, we find that no value of γ reduces scatter as well as the Tully et al. formulation. In the R band, the Tully et al. corrections perform only marginally better than the luminosity-independent corrections (TF scatter decreases by 11% compared to 10%), but at B and U the differences become more substantial (at U, scatter decreases by 18% compared to 8%). We therefore conclude that the general behavior, if not the zero point, of the luminosity-dependent corrections appears correct.

4.5 Fitting Technique

TF samples are generally incomplete at low luminosities and low surface brightnesses, resulting in asymmetric scatter about the fundamental relation. In a fit to magnitude as a function of $\log v$ (the "forward" TFR), this asymmetric scatter leads to artificially shallow slopes. Extended luminosity coverage, as in the NFGS, helps to alleviate the problem, but asymmetric faint-end scatter can still bias results.

Willick (1994) describes one way to address TF slope bias, using an iterative analysis. His technique assumes that the "missing" galaxies have the same intrinsic TF slope and scatter as the observed galaxies. However, if either the scatter or the slope increases at low luminosity, the bias-corrected slope is still too shallow.

[4]Note that we add the 17 $\mathrm{km\,s^{-1}}$ "restored turbulence" term before the inclination correction, apparently contrary to the formula in Tully & Fouque, because otherwise the turbulence correction is multiplied by $1/\sin i$ while the restoration is not, which still results in square roots of negative numbers.

Alternatively, one can fit the "inverse" relation (minimizing the scatter in velocity width as a function of magnitude) without any bias correction, assuming that velocity width biases are negligible (cf. Tully & Pierce, 2000; Schechter, 1980). This approach seems appropriate for our sample, because: (1) optical RC data (unlike radio data) are not subject to a velocity width detection bias, and (2) the NFGS makes no explicit diameter cut that might introduce an indirect velocity width bias through a correlation of rotation speed with surface brightness. However, intrinsic surface brightness and color bias in the parent survey may still play a role.

Tables 1 and 2 present our basic TF calibrations using three different techniques: error-weighted inverse fits, bivariate fits with regression in both magnitude and velocity width errors, and unweighted inverse fits, our preferred technique. Error-weighted inverse fits avoid the usual TF slope bias, but they favor galaxies with higher luminosity and larger velocity width, which have smaller errors. Bivariate fits use all the available information but at the expense of introducing some slope bias (c.f. Sakai et al., 2000). In the remainder of this paper we rely on unweighted inverse fits. Note that the systematic differences between these fitting techniques often exceed the formal errors (Tables 1 and 2).

We compute unweighted inverse fits in two steps. First we find the 68% confidence interval for the slope, where for each test value of the slope we allow the intercept to assume the value that minimizes deviations for that slope. Once we have the best-fit slope, we fit for the intercept with the slope fixed. Although the results are the same as those of a one-step two-parameter fit, the errors are different. This type of fit is appropriate for comparing slopes of different subsamples irrespective of zero point, or conversely for comparing zero points at fixed slope.

All fits are subject to one round of 3σ rejection. Such rejection reduces measured scatter in a Gaussian distribution by $\sim$2%, which we correct for in $\sigma_{3\sigma\,\mathrm{rej}}$. Using the same slope and zero point we also compute the full scatter $\sigma_{\mathrm{all\,pts}}$, the biweight scatter (Beers et al., 1990), and the predicted scatter from observational errors σ_{pred}. The biweight statistic provides the most robust measure of observed scatter, generally agreeing closely with $\sigma_{3\sigma\,\mathrm{rej}}$.

4.6 The Spiral TFR 1: Basic Calibration & Literature Comparison

Traditional TF samples consist of moderately bright spirals, chosen to be relatively edge-on to avoid uncertain $\sin i$ corrections. In this section and the next two, we analyze the TFR for spirals that are brighter than $M_R^i = -18$ and inclined by more than 40°. The NFGS contains 69 Sa–Sd spirals that meet these criteria; optical velocity widths and magnitudes are available for 68 of these (67 at U). HI linewidths are available for 46 of the 68 (or 45 of the 67).

Table 1 provides TF fit parameters for these samples in U, B, and R, including the observed scatter values and the scatter values predicted to arise from measurement errors. Measurement-error scatter remains fairly constant across the three passbands, while observed scatter increases sharply from R to B to U. Subtracting the two in quadrature yields an estimate of the intrinsic scatter in the TFR.[5]

To demonstrate that our results are consistent with previous Tully-Fisher analyses, the remainder of this section compares the NFGS spiral sample with two large field-galaxy samples (Courteau, 1997; Mathewson et al., 1992, hereafter MFB) and with the complete Ursa Major sample of Verheijen & Sancisi (2001).

4.6.1 Field Galaxy Samples

The Courteau and MFB samples are ideal for a direct comparison because both employ optical rotation curves. Both data sets have been analyzed by Courteau (1997) using the V_{fit} velocity width parameter described in §4.3.3.2. The Courteau

[5]Using the 46 galaxies in the HI linewidth sample, we can directly compare the scatter in the HI linewidth and optical RC TFRs. For the HI TFR, the unweighted inverse fit results in Table 1 imply an intrinsic scatter of 0.53 mag. An unweighted inverse fit to the optical RC TFR for the same 46 galaxies has an observed scatter of 0.72 mag and a predicted measurement-error scatter of 0.54 mag, implying an intrinsic scatter of 0.48 mag. The intrinsic scatter should really be the same in both cases, because the sample and photometry are identical. This analysis indicates that the errors on the optical velocity widths have probably been overestimated, and those on the catalog HI linewidths underestimated (the HI errors do not account for systematic effects such as confusion in the beam). We can harmonize the two intrinsic scatter estimates by adding 0.16 mag in quadrature to the optical RC intrinsic scatter estimate and subtracting 0.16 mag in quadrature from the HI intrinsic scatter estimate. (Any correction to the errors should be approximately equal for the optical and radio velocity widths, because the optical velocity width errors were originally estimated from the scatter in the optical-to-radio conversion, see §4.3.3.) However, we do not adjust the predicted scatter values in Table 1 to reflect this correction, as the listed values would change by only ∼0.02 mag, and the correction estimated here is based on an incomplete subsample.

Table 1. Tully-Fisher Fits to the Sa-Sd $M^i_R < -18$ Sample [a]

Band	Wtd Inv	Bivariate	Unwtd Inv	Unwtd Inv HI
		Slope		
U	-9.54±0.29	-8.36±0.34	-10.85±0.46	-10.53±0.33
B	-9.52±0.27	-8.68±0.33	-10.09±0.39	-10.44±0.32
R	-9.70±0.27	-9.15±0.31	-10.14±0.37	-9.75±0.27
		Zero Point		
U	-19.60±0.04	-19.71±0.05	-19.82±0.06	-19.71±0.04
B	-19.71±0.04	-19.79±0.05	-19.83±0.05	-19.74±0.04
R	-20.69±0.04	-20.76±0.05	-20.81±0.05	-20.62±0.03
		Scatter [b]		
U	0.88(0.56)	0.81(0.51)	1.02(0.63)	0.85(0.45)
B	0.78(0.56)	0.73(0.52)	0.82(0.59)	0.77(0.46)
R	0.70(0.56)	0.67(0.53)	0.74(0.58)	0.68(0.42)

[a]Fit results from weighted inverse, bivariate, and unweighted inverse fitting techniques for optical ($W_{V_{pmm}}$) and radio (W_{HI}) T-F calibrations (see §4.5). Errors given are the formal statistical errors from a two-step fit, see §4.5. We require $i > 40$.

[b]Measured biweight scatter and predicted scatter (in parentheses) from measurement errors.

sample consists of ∼300 Sb–Sc spirals with $55 < i < 75$, typically brighter than $M^i_R \sim -18$ (using Courteau's extinction corrections) and pruned by eye to eliminate peculiar and interacting galaxies (Courteau, 1996). The MFB sample includes ∼950 Sb–Sd spirals with $i > 40$, typically brighter than $M^i_R \sim -18$ (assuming $R-I$ colors of ∼0.5 mag and using our standard extinction corrections).

Figure 4.7 plots the TFRs for two subsamples of the NFGS defined to match the Courteau and MFB selection criteria.[6] The left panels show Courteau's TF fits for the

[6]We select the NFGS comparison sample for Courteau using inclinations defined with Courteau's value of q_0 (0.18) and using magnitudes defined with Courteau's preferred extinction corrections (which include a zero point offset, Courteau, 1996). We interpret Courteau's Sb–Sc restriction to include galaxies of type Sab and Scd, and in keeping with Courteau we prune the NFGS sample to remove galaxies with strong peculiarities (defined in §4.7.2). The comparison sample for MFB is selected using inclinations defined with our standard q_0 (0.20) and using magnitudes defined with the Tully et al. (1998) extinction corrections, although these galaxies are plotted in the lower left panel of Figure 4.7 using Courteau's inclination and extinction corrections. The MFB comparison sample is unpruned, with all galaxies of type Sb–Sd (3–7) included. Except for the exclusion of Sa

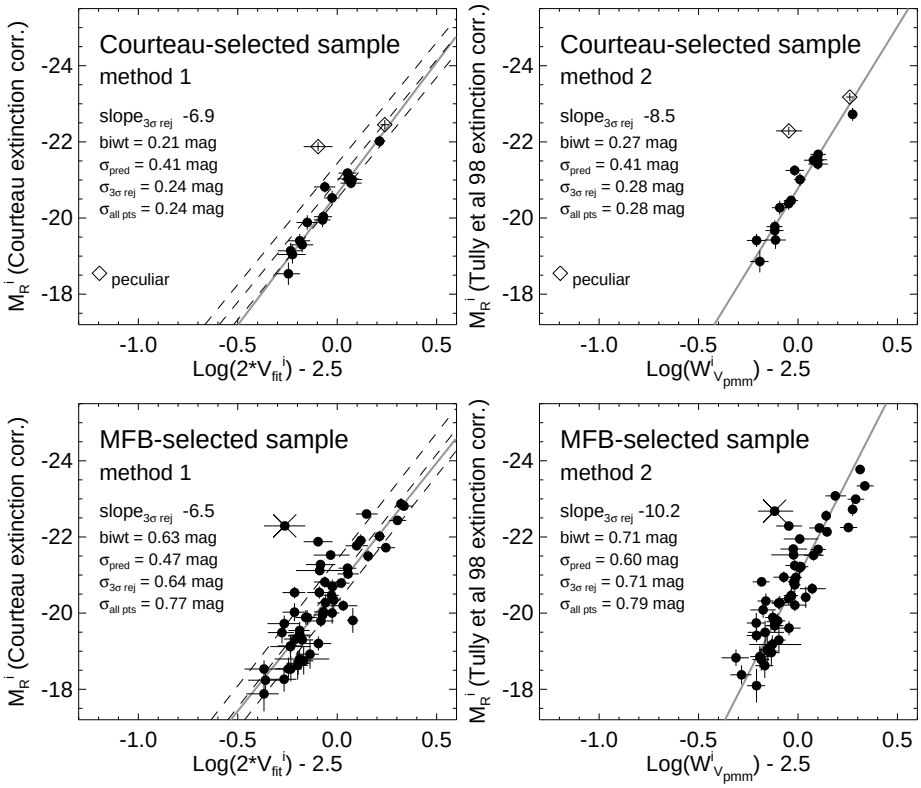

Figure 4.7.— Comparison between TF fits for the NFGS and for the samples of Courteau (1997) and Mathewson et al. (1992, as analyzed by Courteau 1997). The upper panels show NFGS data meeting Courteau's selection criteria, while the lower panels show NFGS data meeting MFB's selection criteria (§4.6.1). Diamonds indicate peculiar/interacting galaxies eliminated from the Courteau-selected sample following Courteau (our peculiarity classification is discussed in §4.7.2). X's indicate a galaxy rejected from the MFB sample fits as a $>3\sigma$ outlier (but still included in calculating the biweight scatter and $\sigma_{\rm all\ pts}$). *Left Panels:* NFGS comparison samples analyzed using the methods of Courteau (forward fits, luminosity-independent extinction corrections, V_{fit} velocity parameter, and $q_0 = 0.18$). Fit parameters and thick gray lines give fit results for the NFGS data. Dashed lines show Courteau's forward fits to the Courteau and MFB data sets and the $\pm 1\sigma$ scatter on these fits; both fits have been adjusted to $H_0 = 75$. The Courteau fits have also been shifted from Gunn r to Cousins R using $r - R = 0.354$ (Jorgensen, 1994), and the MFB fits have been shifted from Cousins I to Cousins R using $R - I = 0.5$ (Frei & Gunn, 1994, their I_c and R_c). *Right Panels:* The same data analyzed using our standard techniques (unweighted inverse fits, luminosity-dependent extinction corrections, $W_{V_{pmm}}$ velocity parameter, and $q_0 = 0.20$). Fit parameters and thick gray lines give fit results for the NFGS data.

MFB and Courteau samples overlaid on our matching subsample data points and fits. Here we use Courteau's analysis techniques, including forward fits (minimizing residuals in M_R^i), the V_{fit} velocity width parameter, and Courteau's luminosity-independent extinction corrections. For the 15 NFGS galaxies matching the Courteau selection criteria, the biweight scatter of 0.21 mag is lower than Courteau's 0.46, probably fortuitously. The apparent zero-point offset may also represent small-number statistics, especially since no significant zero-point shift is apparent between the NFGS and MFB samples.[7] For the 54 NFGS galaxies matching the MFB selection criteria, the biweight scatter of 0.63 mag is quite close to the value Courteau measures from the MFB data, 0.56. Note that we expect the MFB sample to have lower measurement-error scatter than the NFGS, because MFB galaxies were selected to have diameters larger than 1.7 arcmin, which is equal to the *mean* major-axis diameter for NFGS spirals: this difference implies that the MFB data set benefits from greater precision in photometric inclination determinations. In addition, the MFB sample luminosity distribution includes relatively fewer low-luminosity galaxies, which tend to have higher TF scatter.

The right panels of Figure 4.7 demonstrate the effect of switching to our standard analysis techniques. We use unweighted inverse fits (minimizing residuals in velocity width), the $W_{V_{pmm}}$ velocity parameter, and luminosity-dependent extinction corrections (Tully et al., 1998). With these conventions, the slope of the TFR steepens considerably, and the measured scatter about the fit increases, despite the smaller scatter perceived by eye. The eye perceives the scatter in velocity width, whereas we measure the scatter in absolute magnitudes: the scatter in absolute magnitudes increases as a result of the steeper slope of the TFR. This steeper slope is due in roughly equal measure to the use of inverse fits and to the use of luminosity-dependent extinction corrections. *We stress that the slope, zero point, and scatter in different samples can only be meaningfully compared when differences in sample selection and analysis techniques are fully taken into account.*

Furthermore, we have not yet accounted for measurement errors. The approximate agreement of our scatter with the scatter in the MFB sample should really be

galaxies, the Sb–Sd sample we define to match the MFB selection criteria is identical to the spiral sample analyzed throughout §4.6–4.8.

[7]However, a problem with the Courteau zero point may have been seen elsewhere. Barton et al. (2000a) report that their sample of galaxies in close pairs shows no zero-point offset from the Courteau sample but does show an offset of ∼0.4–0.5 mag from Tully & Pierce (2000), in the sense that the pairs galaxies are brighter than the reference sample. Given the likelihood that many of the Barton et al. galaxies have experienced some luminosity enhancement due to interactions, the zero point offset from Tully & Pierce seems more likely to be correct, in which case the Courteau zero point would be too bright (as we see here).

taken as evidence that the measurement errors in the two data sets are very similar. For the NFGS subsample defined by MFB's criteria and analyzed using our standard techniques (lower right panel of Figure 4.7), we calculate that 0.60 mag of the observed 0.71 mag of scatter arises from measurement errors, leaving only ∼0.38 mag of intrinsic scatter after subtraction in quadrature. The NFGS subsample error budget includes four contributions added in quadrature: Hubble-law distance uncertainties (0.18 mag[8], dominated by the contribution of the peculiar velocity field); photometric inclination errors (0.42 mag, dominated by the one-decimal place precision of the UGC axial ratios and expected to be better for MFB as explained above); velocity width uncertainties (0.38 mag, dominated by intrinsic scatter in the correspondence between "true" rotation velocities and measured optical velocity widths, regardless of high-quality rotation curves); and extinction correction errors (0.09 mag, derivative of the uncertainties in inclination and velocity width). If the scatter difference between the MFB and NFGS samples is ascribed entirely to inclination errors, then we infer MFB inclination errors of ∼0.3 mag.

4.6.2 Cluster Samples

Figure 4.8 directly compares the NFGS spiral sample with the spiral galaxies in the complete Ursa Major sample of Verheijen & Sancisi (2001, hereafter VS). Like the NFGS, the VS sample is morphology-blind, including both Sa galaxies and peculiar and interacting galaxies. Here we restrict both samples to $M_R^i < -18$, type Sa–Sd, and $i > 45$. Because the full VS sample also contains dwarfs and extreme late-type galaxies, we will revisit it when we extend the NFGS sample to include such galaxies (§4.9.3.2).

With extinction corrections and velocity width definitions carefully matched, we detect no zero-point offset within the errors (Figure 4.8). The slope of the VS sample appears considerably shallower, but inspection of the data reveals that the behavior of a few galaxies at the faint end of the TFR accounts entirely for the difference. We argue in §4.9.3.2 that environmental effects may be responsible for a real divergence between the two samples at the faint end.

The sources of measurement-error scatter for the Ursa Major sample are qualitatively different than for the NFGS, so we must compare intrinsic scatter values, formed by subtracting measurement-error scatter from observed scatter in quadrature. We predict the measurement-error scatter for VS using the same code with which we propagate our own errors; this procedure yields a total predicted scatter of

[8]This number also includes a tiny contribution from photometry errors.

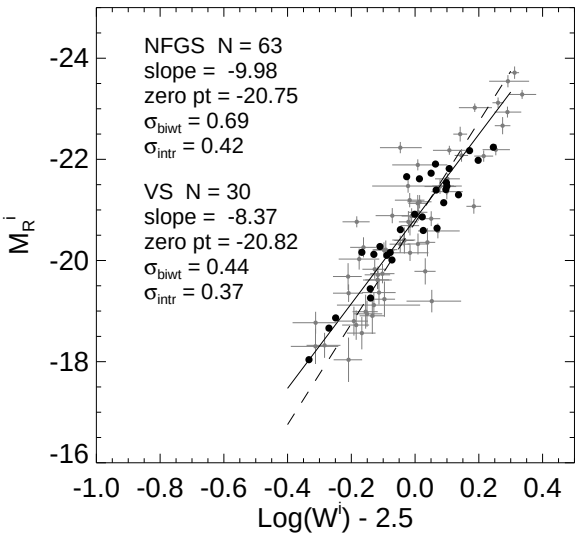

Figure 4.8.— Comparison of TFRs for the NFGS (gray) and for the Ursa Major sample of Verheijen & Sancisi (2001, black), with both samples restricted to types Sa–Sd, $M_R < -18$, and $i > 45$. Solid and dashed lines are unweighted inverse fits to the VS and NFGS data respectively. Biweight scatters are with respect to the corresponding fits. Intrinsic scatters are computed by subtracting measurement-error scatter in quadrature (see §4.6.2). We have recomputed VS's extinction corrections using the original W_R^i definition of Tully & Fouque (1985) to exactly reproduce the method used for the NFGS corrections (§4.4.2). To match the distance modulus VS use for Ursa Major, we temporarily adopt $H_0 = 77$. W^i is $W^i_{V_{pmm}}$ for the NFGS (§4.3.3.3) and W^i_{50} for the VS sample.

0.24 mag from four sources: hybrid kinematic-photometric inclination errors[9] (0.09 mag); HI linewidth errors (0.13 mag); distance uncertainties from cluster depth effects (0.17 mag, as estimated by Verheijen, 1997); and errors in photometry and extinction correction (0.06 mag). These numbers are based on the inclination and HI linewidth errors given by VS; we assume basic photometry errors of ∼0.05 mag.

After subtracting measurement-error scatter in quadrature, we obtain very similar intrinsic scatters for the NFGS and Ursa Major samples: 0.42 mag and 0.37 mag.[10] Recomputing the NFGS scatter and errors about the shallower slope of the

[9]VS's inclination errors would be small even given purely photometric inclinations, because their galaxies are very large on the sky. We have tried substituting inclinations based on UGC axial ratios for their preferred inclinations and the scatter increases negligibly.

[10]Similar agreement is found in the B band, where we estimate intrinsic scatters of 0.52 and 0.48 for the NFGS and Ursa Major spiral samples respectively.

Ursa Major sample, we find an intrinsic scatter of 0.39 mag. If the NFGS velocity width errors are slightly overestimated as discussed earlier (§4.6), then the intrinsic scatter in the NFGS sample may be as high as ∼0.42 mag. Moderately higher intrinsic scatter for the NFGS than for the Ursa Major sample should not be at all surprising, as the NFGS includes a wide range of environments and star formation histories. Apart from the hint of a systematic offset at the faint end already discussed, the two samples are in excellent agreement.

Other cluster TF studies quote lower scatters than we find for the complete Ursa Major sample. For example, combining data from multiple clusters (including Ursa Major, Fornax, Coma, the Pisces Filament, and several others), Tully & Pierce (2000) measure an R-band scatter of 0.34 mag. Sakai et al. (2000) obtain the same result with a partially overlapping data set.[11] However, directly comparing the NFGS spiral sample with these multi-cluster samples would be misleading, for several reasons. First, each individual cluster in the multi-cluster samples obeys a different definition of "complete" and satisfies that definition to a different degree. For example, the "complete" Fornax sample rejects interacting or disturbed galaxies and multiple systems (Bureau et al., 1996). Second, each cluster represents a slightly different environment, and indeed the clusters' mean $B-I$ colors sometimes differ by ∼0.1 mag, probably indicating different star formation histories (Tully & Pierce, 2000). We will see in §4.8.2.1 that such color offsets almost certainly imply TF zero point offsets between the clusters. However, these zero-point offsets are suppressed and do not contribute to the scatter, because the multi-cluster analyses slide each individual cluster's TFR in zero point until it best matches the other clusters' TFRs. A third concern is the effect of a top-heavy luminosity distribution: in combining more distant clusters with more nearby ones, the multi-cluster studies define samples that statistically favor bright galaxies. This bias drives down scatter.

[11] Sakai et al. use bivariate fits, intermediate between forward and inverse fits; see §4.5 and Table 1, but otherwise use techniques similar to Tully & Pierce and ourselves. Their estimates of the intrinsic scatter of the TFR using the local calibrator galaxies with Cepheid distances is not relevant to the present discussion, as the calibrator galaxies do not even approximate a complete sample of the local galaxy population.

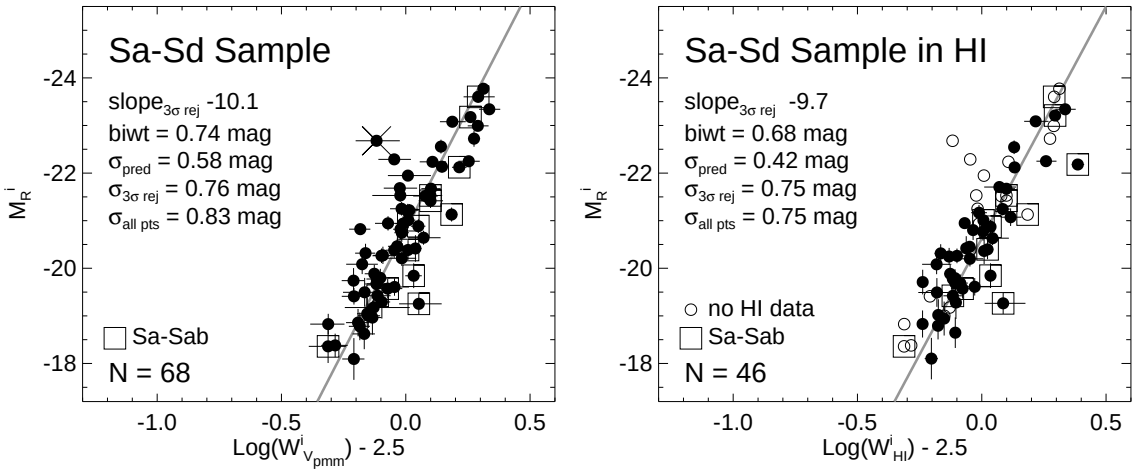

Figure 4.9.— The TFR for the Sa–Sd sample, illustrating the Sa galaxy offset toward higher W^i or lower L. The left panel uses optical velocity widths while the right panel uses HI linewidths, with missing data points indicated by an open circle at the position of the optical velocity width. Lines show unweighted inverse fits to the solid points.

4.7 The Spiral TFR 2: Sa & Peculiar Galaxies

Sa galaxies and galaxies with morphological peculiarities are often excluded from TF samples. Here we analyze their TF residuals within the NFGS spiral sample (types Sa–Sd brighter than $M^i_R = -18$ and inclined by $>40°$).

4.7.1 An Sa Galaxy Offset

Fourteen of the 68 galaxies in the NFGS spiral sample are Sa galaxies.[12] As a group, these 14 galaxies sit clearly to one side of the Sb–Sd TFR (Figure 4.9), offset toward lower L and higher W^i by 0.7 mag at R, 0.9 mag at B, and 1.2 mag at U (with an uncertainty $\sim$0.15 mag). Extrapolating our results redward using Cousins $R-I$ colors from Frei & Gunn (1994, their R_c and I_c), we predict an I-band offset of $\sim$0.55 mag with an uncertainty of $\gtrsim$0.15 mag. Giovanelli et al. (1997a) measure an I-band offset of 0.32 mag between Sa galaxies and later types, roughly consistent with our extrapolated prediction, using somewhat different analysis techniques.

The possibility that Sa galaxies rotate faster at a given luminosity was first suggested by Roberts (1978) based on 21 cm data. Sa offsets became controversial

[12] "Sa" will be taken to mean both Sa and Sab for this discussion.

after Rubin et al. (1985) claimed that the Sa TFR lies a full 2 mag below the Sc TFR in the B band. Simard & Pritchet (1998) argue that a greater intrinsic spread of luminosities for late-type vs. early-type galaxies at a given velocity width, combined with Malmquist bias, may explain the large offset found by Rubin et al. (1985). However, Sa offsets continue to be observed in increasingly complete samples (e.g. Verheijen, 1997).

The scatter properties of our data suggest that the offset we observe is mostly real. In the R band, the Sa galaxies and the Sb–Sd galaxies have biweight TF scatters of 0.62 mag and 0.71 mag, respectively. These numbers imply that Malmquist bias is very unlikely to produce the observed 0.7 mag offset between the two populations. In the B and U bands, the scatter in each population increases but the offset increases even more. The offset exceeds the scatter by 0.3 mag at U.

We have investigated whether the Sa offset in our data may be ascribed to systematic errors in luminosity or velocity width measurements. For example, large bulges could make Sa galaxies appear rounder (and more face on) than they really are, leading to underestimated extinction corrections and overestimated $\sin i$ corrections. Sa's in the present sample do have more face-on inclination estimates on average (61° vs. 66° for the full spiral sample); however, this difference can account for an offset of only $\sim$0.2 mag at a TF slope of -10. Furthermore, even extreme assumptions about axial ratios (e.g. assigning an intrinsic axial ratio of $q_0 = 0.4$ to Sa's and assigning $q_0 = 0.09$ to all other types, or modifying the UGC axial ratios for Sa's according to $(b/a)_{\rm mod} = (b/a)_{\rm orig} - 0.2(1 - (b/a)_{\rm orig})$) reduce the R-band offset by at most half and have much less effect in the B and U bands. No other aspect of our analysis is responsible for the offset either. Whether we adopt luminosity-dependent or independent extinction corrections has negligible effect on our results. We do not add an explicit morphological type dependence to our extinction corrections, but we note that adding such a dependence would only increase the Sa offset: extinction is expected to be lower in Sa galaxies (Kodaira & Watanabe, 1988). The offset is not appreciably affected when we substitute V_{fit} for V_{pmm} or when we omit the optical-to-radio conversion. The available HI data also seem to confirm the offset (Figure 4.9), although these data are subject to incompleteness and high scatter for the Sa population.

We conclude that the bulk of the Sa offset in our sample is real. However, with just 14 Sa galaxies, our analysis is subject to small number statistics. Formally, a Kolmogorov-Smirnov test yields a probability of 6×10^{-4} that the R-band TF residuals of the Sa and Sb–Sd subpopulations were drawn from the same parent population ($\sim 3.5\sigma$). A possible physical explanation for the Sa offset will be discussed in §4.8.2.1.

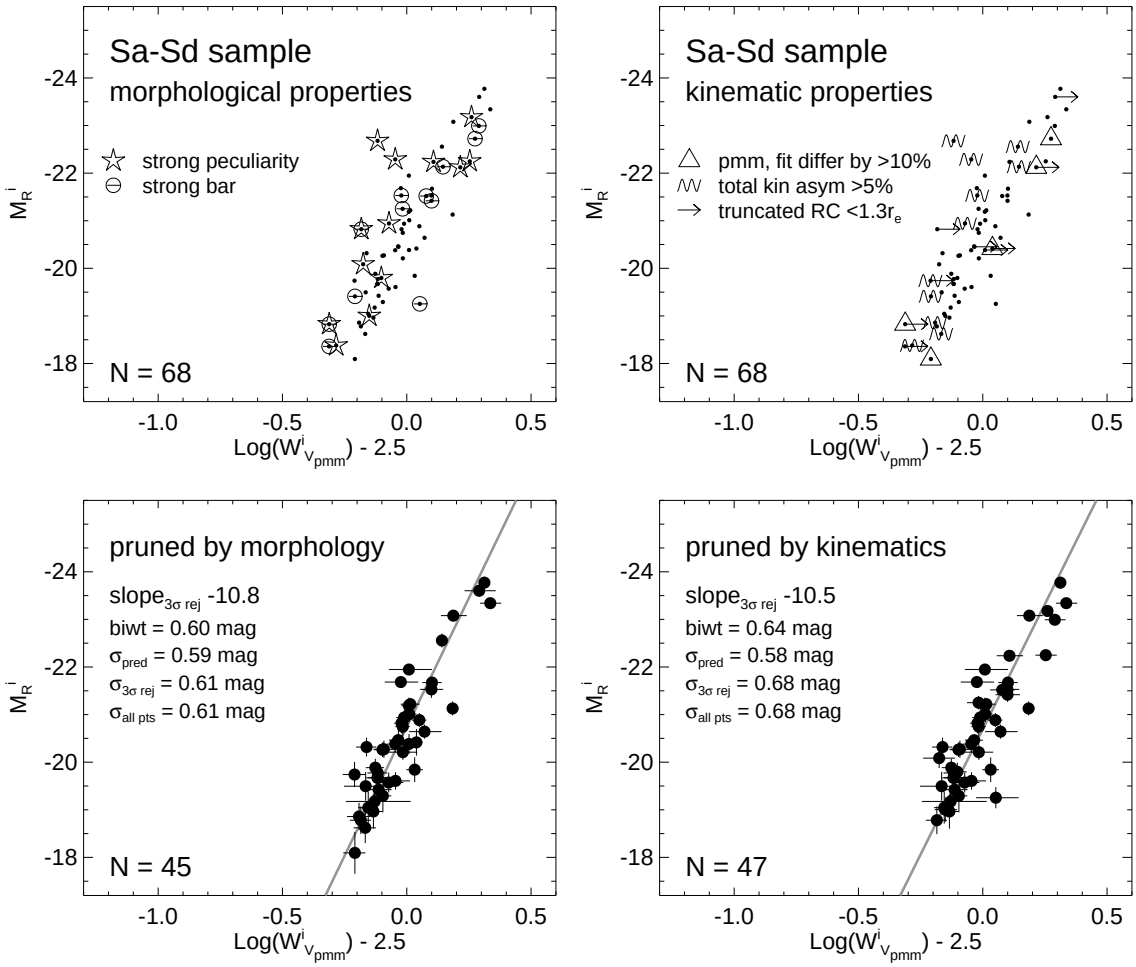

Figure 4.10.— Upper Panels: Location of kinematically and morphologically peculiar galaxies within the Sa–Sd TFR. Lower Panels: Effect of pruning the sample to remove such galaxies. Unweighted inverse fit results are shown.

4.7.2 Galaxy Peculiarity and Sample Pruning

The top left panel of Figure 4.10 identifies galaxies in the spiral sample with strong bars or morphological peculiarities such as warps, tidal features, multiple nuclei, polar rings, or interacting neighbors. Below we refer to galaxies with morphological peculiarities as "peculiar galaxies," with the understanding that these galaxies are really disturbed spirals rather than galaxies that cannot be reliably classified. The top right panel of Figure 4.10 identifies galaxies with kinematic peculiarities: these galaxies have truncated rotation curves ($r_{max} < 1.3r_e$), rotation curve asymmetries greater than 5% (§4.3.2), or discrepancies between $W_{V_{fit}}$ and $W_{V_{pmm}}$ greater than 10%. Both morphologically peculiar galaxies and galaxies with high rotation curve

asymmetry tend to lie on the high L/low W^i side of the TFR. We return to these observations in §4.8.

The lower left panel of Figure 4.10 demonstrates that removing peculiar and barred galaxies from the sample reduces R-band scatter to approximately the level expected from measurement errors. This reduction implies that peculiar and barred galaxies contribute 0.14 mag of the full spiral sample scatter of 0.74 mag, or 0.43 mag in quadrature. The pruned sample shows even more substantial scatter reduction in bluer passbands, but the lower scatters in these bands still exceed the level expected from measurement errors: we measure 0.63 mag and 0.71 mag in B and U, respectively, compared to predicted measurement-error scatters of 0.58 mag in both wavelength bands. The lower right panel of Figure 4.10 shows that kinematic pruning is as effective as morphological pruning for Sb–Sd galaxies, but it misses some Sa outliers. Most NFGS Sa galaxies have very symmetric and extended rotation curves. Both types of pruning reduce the sample size by >30%.

Of course, labeling a galaxy "peculiar" or even "barred," is somewhat subjective, as each galaxy is unique and we see galaxies only in projection. To avoid bias, bars and morphological peculiarities were independently identified by two of us (S.K. and M.F.) without reference to TF residuals. The identifications were homogenized by S.K. and further checked against the notes provided by R.A. Jansen in Jansen et al. (2000b). Although a number of weak bars and peculiarities were noted, here we report only strong, unambiguous cases identified by more than one observer. These peculiarities are broadly distributed across a wide range of spiral types and luminosities.

Our kinematic peculiarity classifications are objective in that they are quantitative, however the classification criteria were chosen empirically (the $r_{max} > 1.3r_e$ requirement does have some theoretical basis, as discussed in §4.3.3.2). To test whether these criteria have physical significance or merely identify faulty rotation curves, Figure 4.11 shows the effect of pruning the HI linewidth TFR using kinematic peculiarity information obtained from our optical RCs. After kinematic pruning, the scatter in the HI TFR drops to 0.56 mag, compared to 0.68 mag before pruning and 0.60 mag after morphological pruning. The success of kinematic pruning for the HI TFR emphasizes the link between optical and radio velocity widths: optical RC peculiarities correctly flag outliers in the HI linewidth TFR. This result implies either that (1) optical RC peculiarities are associated with observational errors in NFGS surface photometry or UGC-derived photometric inclinations (common to both HI and optical RC TFRs), or that (2) optical RC peculiarities occur in galaxies that lie off the TFR for physical reasons. We find evidence for the latter in §4.8.

Kinematic and morphological peculiarities are frequently associated, but not al-

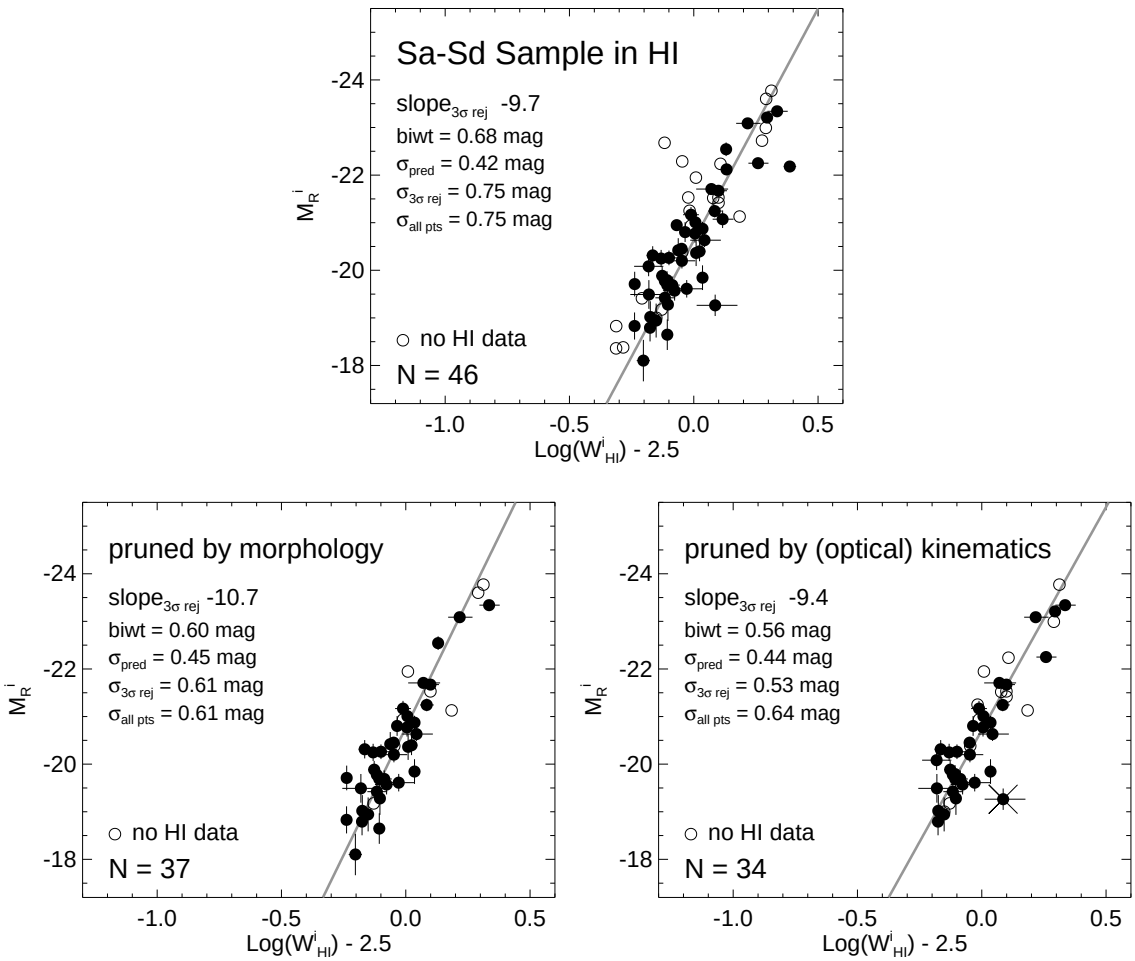

Figure 4.11.— The HI TFR for the Sa–Sd subsample. Galaxies with no HI linewidth are indicated by an open circle at the position of the optical velocity width (compare with Figure 4.7, lower right panel). Unweighted inverse fit results and sample sizes are given in each panel, using the solid points only. Lower panels show the effect of pruning the sample as in Figure 4.10. The kinematic pruning is determined by the properties of the optical rotation curve. An X marks a point rejected by the fitting routine as a $>3\sigma$ outlier (but still included in calculating the biweight scatter and $\sigma_{\rm all\,pts}$).

ways. Figure 4.12 shows rotation curves and images for three galaxies identified as morphologically peculiar. Only the top two meet our quantitative criteria for kinematic peculiarity (the third galaxy's RC does contain a kinematically distinct component, but this component is probably associated with a companion). Conversely, some galaxies with asymmetric or truncated RCs do not qualify as strongly morphologically peculiar. The imperfect correspondence between morphological and kinematic peculiarities suggests that culling peculiar galaxies from a TF sample in order to reduce scatter is a somewhat blind strategy. In §4.8 we use more objective, physically motivated techniques to reduce TF scatter to comparably low levels without discarding galaxies from the sample.

4.8 The Spiral TFR 3: Third Parameters & Physical Sources of Scatter

We have seen that interacting, merging, and peculiar galaxies often lie on the high L/low W^i side of the TFR, while Sa galaxies lie on the low L/high W^i side (§4.7 and Figure 4.13). Below we show that these offsets reflect underlying correlations between TF residuals and quantitative galaxy properties, most notably $B-R$ color and Hα equivalent width (EW). Following tradition, we refer to these properties as "third parameters," i.e. additional variables that control physical scatter in the two-parameter TFR. Our analysis makes use of photometric and spectrophotometric quantities from the NFGS database (Jansen et al., 2000a,b) and photometric asymmetries kindly provided by R. Jansen (private communication, see also Jansen, 2000).

4.8.1 Third Parameter Analysis Technique

Barton et al. (2000a) demonstrate that false correlations between TF residuals and candidate third parameters may arise when the TF slope is measured incorrectly, in which case any parameter that varies along rather than perpendicularly to the TFR will produce a correlation. A true third parameter should vary at least partly perpendicularly to the TFR.

We adopt the following strategy to avoid false detections of third parameters. First, we apply strict cuts in M^i to eliminate sections of the data where the velocity width scatter is clearly asymmetric. For the R band, these cuts are indicated by the dashed lines in Figure 4.13 (see also Table 3): the bright end of the TFR shows asymmetric scatter above $\mathrm{M}^i_\mathrm{R} \sim -22.5$ while the faint end is excluded by the spiral

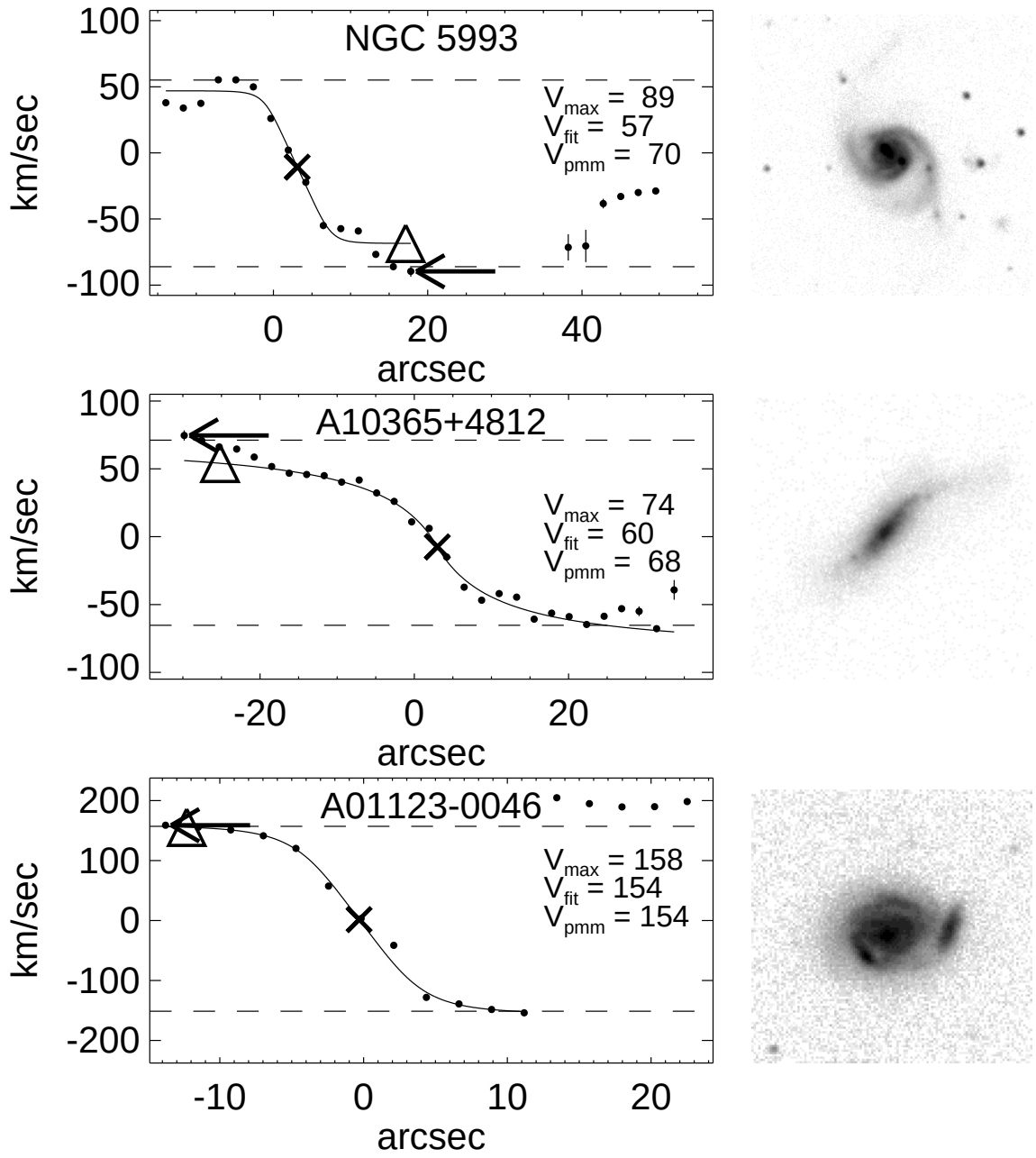

Figure 4.12.— Images and rotation curves for three galaxies with morphological peculiarities (§4.7.2). Notation is as in Figure 4.6. The distinct kinematic components at large radii in the first and third panels were not used to define velocity width measures. Images are from Jansen et al. (2000b).

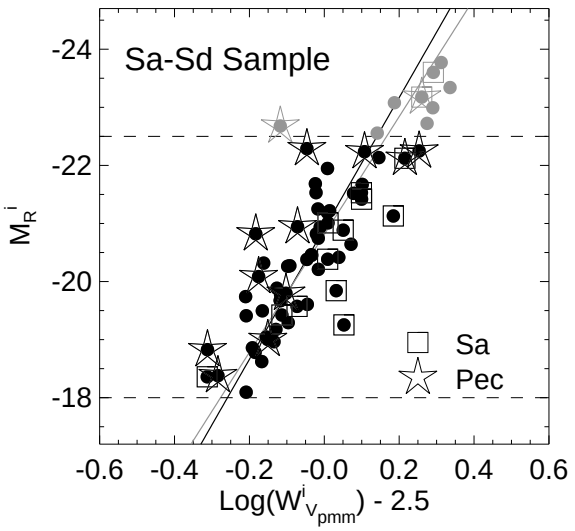

Figure 4.13.— Systematic offsets in the Sa–Sd TFR. Sa and peculiar galaxies fall on opposite sides of the TFR, helping to drive strong correlations between TF residuals and physical properties such as effective $B-R$ color and global EW(Hα). In §4.8 we quantify the statistical significance of these correlations within the luminosity range between the dashed lines. This range excludes the asymmetric scatter at the bright end of the relation to ensure fair statistical tests (§4.8.1). The gray and black lines show unweighted inverse TF fits to the sample with and without the bright-end galaxies. For statistical tests, we define residuals relative to the black line.

Table 3. Magnitude Cuts for Spearman Rank Tests [a]

	U	B	R
bright cut	-21	-21	-22.5
standard faint cut	-17	-17	-18
dwarf faint cut	-16	-16	-17

[a]Cuts applied to extinction-corrected absolute magnitudes for third-parameter tests. See §4.8.1.

sample definition. After these cuts, the data are biased in M^i but nearly perfectly unbiased in velocity width. Second, we apply an inverse TF fit to the data, which minimizes residuals in velocity width. At this point the velocity width residuals are completely uncorrelated with luminosity M^i. Finally, we use Spearman rank tests to quantify both the candidate third parameter–TF residual correlation and the candidate third parameter–luminosity correlation. For the Spearman tests, velocity width residuals and magnitude residuals are interchangeable. If these tests show that the candidate third parameter correlates with TF residuals but not with luminosity, then we conclude that it varies perpendicularly to the TFR.

In fact, even if a parameter does vary with luminosity, it may still qualify as a third parameter if it also correlates clearly with TF residuals, because we have in principle eliminated the TF residual–luminosity correlation. Nonetheless, one must be wary if the parameter-luminosity correlation is stronger than the parameter–TF residual correlation, as in such a case even small TF slope errors may lead to false correlations. For luminosity-dependent parameters, one may wish to subtract out the luminosity dependence and measure the correlation between TF residuals and "parameter residuals," i.e. parameter offsets from the fitted parameter–luminosity correlation (cf. Courteau & Rix, 1999). We give results based on uncorrected parameters below, but we also check results using a luminosity dependence correction for two parameters, rotation curve asymmetry and effective $B-R$ color (Figure 4.14).

In general, we use unweighted TF fits to define TF residuals. Unweighted fits avoid the slope bias caused by errors that vary systematically with luminosity and velocity width. However, all results reported below are significant at $\gtrsim 3\sigma$ confidence using both weighted and unweighted fits unless noted otherwise. We have confirmed all correlations using two definitions of velocity width ($W_{V_{fit}}$ and $W_{V_{pmm}}$) and using both luminosity-dependent and luminosity-independent extinction corrections (§4.4.2). In what follows we quote results using $W_{V_{pmm}}$ and the Tully et al. (1998) extinction corrections.

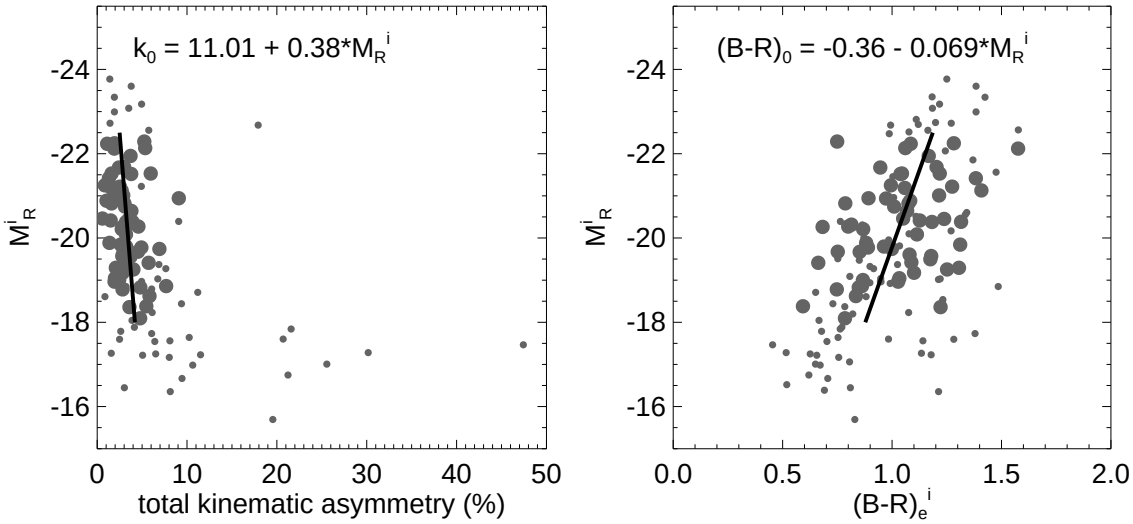

Figure 4.14.— M_R^i vs. total RC asymmetry (§4.3.2) and effective $B-R$ color. Larger points represent the luminosity and inclination-restricted spiral sample of Figure 4.13, while smaller points show other galaxies in the optical RC sample. The left panel excludes galaxies with $i < 40$ and the right panel excludes galaxies with $i < 5$. Black lines represent least-squares inverse fits to the larger points, minimizing residuals in color and RC asymmetry. Although these fits are determined using only the data for the spiral sample of Figure 4.13, for consistency we use the same fits for the full sample analysis in §4.9. Note that inverse fits are appropriate for combining with our inverse TF fits; some bias is clear in the line slopes, but it has no effect on our conclusions.

We do not perform a detailed third-parameter analysis of the radio TFR, as the catalog HI linewidths are incomplete and of mixed quality. However, both internal and external checks suggest that the same third parameters probably operate in the radio TFR (see next section).

4.8.2 Third Parameter Test Results

For the luminosity-restricted Sa–Sd sample of Figure 4.13, TF residuals correlate strongly with $(B-R)_e$ (effective $B-R$ color[13]) and global EW(Hα) in all bands. Other measures of color and emission-line strength yield somewhat noisier correlations. We also find correlations with rotation curve asymmetry, photometric asymmetry, and two measures of surface brightness; these correlations reach $>3\sigma$ significance only

[13]Effective colors are measured from all light within the B-band half-light radius r_e (Jansen et al., 2000b).

in certain photometric bands. TF residuals do not correlate with luminosity (by construction) or with inclination, validating our analysis. Likewise, we detect no correlation between TF residuals and rotation curve extent, isophotal radius, effective radius, HI gas mass, gas consumption timescale, or $M_{\rm HI}/L$ (we have incomplete data for the last three however, see §4.8.2.6).

Figure 4.15 displays some of the correlations in the R band and lists Spearman rank test results for U, B, and R (the "probability of no correlation" p is given, where $1-p$ is the confidence of the result). The symbol coding shows that Sa and peculiar galaxies drive most of the statistical signal in the R-band correlations. If we eliminate both groups of galaxies, no R-band correlation survives with $>3\sigma$ confidence. However, the $(B-R)_e$ correlation does survive in B, and both color and emission line correlations remain significant in U. In general, the two groups of galaxies contribute roughly equally to the correlations, with the Sa galaxies showing a slightly stronger signal due to lower scatter. The peculiar galaxies form a more heterogeneous group, including not only interacting, merging, and warped galaxies, but also a few galaxies whose oddities may indicate later evolutionary states, e.g. a bulge-dominated Sa galaxy deeply reddened by a polar dust lane (NGC 984).

Although Sa and peculiar galaxies dominate the statistical signal we measure, the correlations in Figure 4.15 apply to all galaxies in the sample. A blue, strongly star-forming galaxy whose image does not appear peculiar nonetheless shows the expected TF residual. Thus the correlations provide a physical, quantitative basis for understanding systematic offsets in the TFR, independent of morphological classification.

Furthermore, the correlations are not limited to the optical TFR. Despite disproportionate HI catalog incompleteness for bright and peculiar galaxies, mixed HI data quality, and confusion in single-dish linewidths, we still detect 2–3σ correlations between radio TF residuals and both $(B-R)_e$ and global EW(Hα). We also find evidence for a TF residual–total color correlation in radio data from the complete Ursa Major database of Verheijen & Sancisi (2001), see §4.8.2.1. These results emphasize the close link between optical and radio velocity widths already seen in §4.3.3 and §4.7.2.

4.8.2.1 Color

Effective $B-R$ color correlates beautifully with TF residuals, predicting spiral galaxy TF offsets better than any other physical parameter we have tested. Effective $U-B$ color also yields a clear correlation in all three bands. The color–TF residual

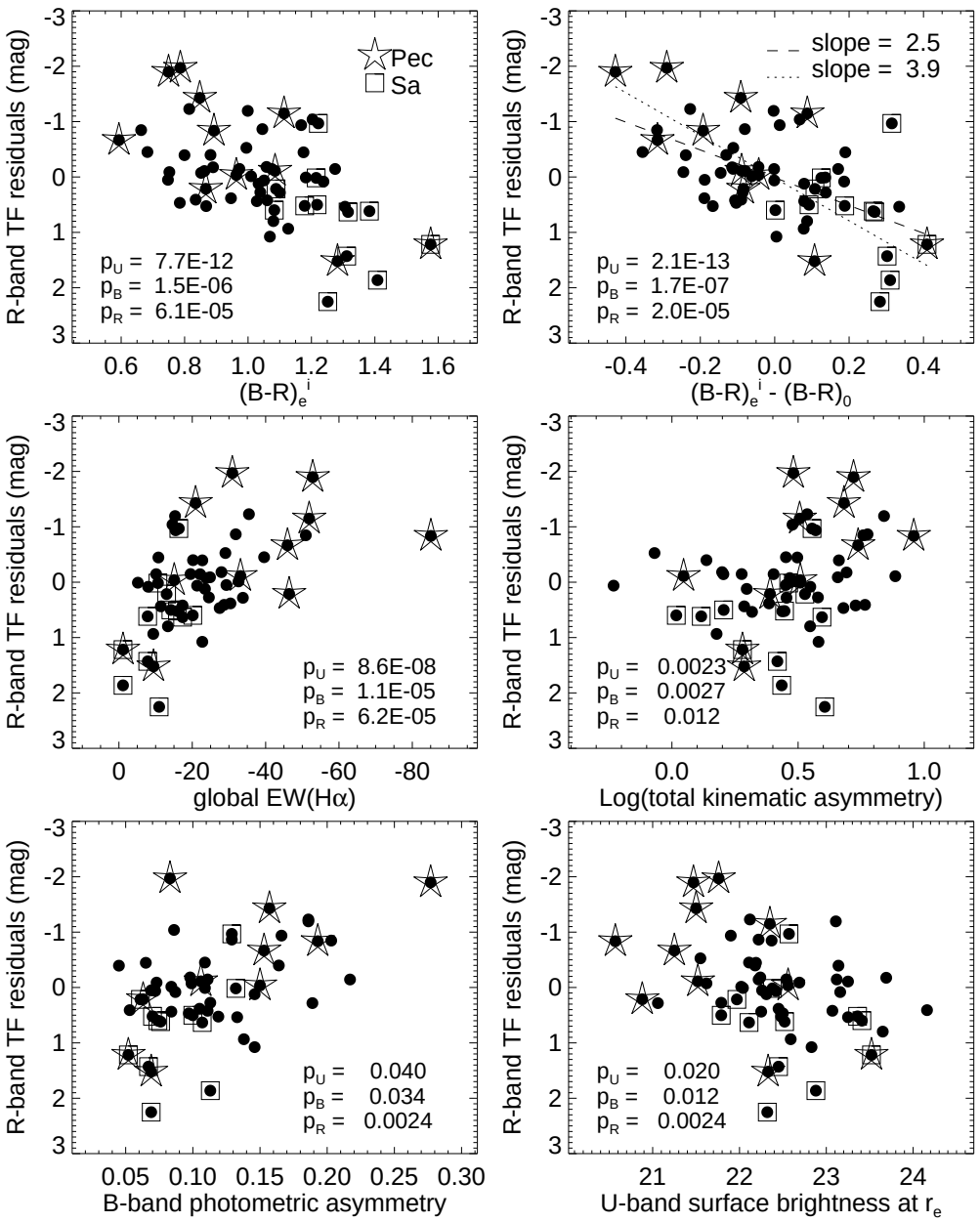

Figure 4.15.— TF residuals vs. physical properties of the Sa–Sd $i > 40$ $-18 < M_R^i < -22.5$ sample (see also Figure 4.13). Squares indicate Sa galaxies and stars indicate galaxies with morphological peculiarities (§4.7.2). The Spearman rank probability of no correlation between the parameter and TF residuals in each optical band is given as p_{band}. Only R-band TF residuals are shown. Top right panel: Colors have been defined relative to the color–magnitude relation (Figure 4.14). Dashed and dotted lines show forward least-squares and least-squares bisector fits (Isobe et al., 1990, see §4.8.3.1).

correlations strengthen from R to B to U, as blue peculiar galaxies and red Sa galaxies move further apart in the TFR. Although we correct colors for internal extinction (see §4.4.2), omitting the extinction correction does not significantly affect the correlation strength.

For our sample, effective colors produce much tighter correlations than total colors. In the R band, Spearman tests yield $p = 6.1 \times 10^{-5}$ for the $(B-R)^i_e$ correlation, or $\sim 4\sigma$, but only $p = 0.034$ for the total $(B-R)^i$ correlation, or just over 2σ. Total colors dilute the correlation signal with observational scatter from profile extrapolation and background subtraction (R. Jansen, private communication). However, we see no strong systematic differences between $B-R$ and $(B-R)_e$: on average the two track closely, with $(B-R)_e$ slightly redder, by at most $\sim$0.1 mag for the reddest galaxies.

Comparing Figures 4.14 and 4.15, we see that the color–TF residual correlation appears tighter than the color–magnitude relation for the spiral sample of Figure 4.13, and Spearman tests confirm this impression. As a consequence, if we use the fit shown in Figure 4.14 to subtract a color zero point at each luminosity, following Courteau & Rix (1999), the resulting color residual–TF residual correlation has only marginally greater significance than the raw color–TF residual correlation (Figure 4.15). However the corrected correlation has a more direct physical interpretation; see §4.8.3.

For the moment we focus on reducing TF scatter rather than on understanding the physics of the correlation. If we restore spirals brighter than $\mathrm{M}^i_\mathrm{R} = -22.5$ to the sample (they were not used in Figure 4.15, see Figure 4.13), then fitting the raw color–TF residual correlation provides a color-correction formula to go with the TF fit in Table 1. A least-squares forward fit to ΔM vs. $(B-R)^i_e$ yields

$$\Delta \mathrm{M}^\mathrm{i}_\mathrm{R} = -2.0 + 1.8(\mathrm{B}-\mathrm{R})^\mathrm{i}_\mathrm{e}. \tag{4.14}$$

If we correct our R-band magnitudes with equation 4.14 and recompute the residuals with respect to the original TF fit, the biweight scatter falls from 0.74 mag to 0.66 mag. An analogous procedure reduces scatter to 0.64 mag in both the B and U bands, from 0.82 and 1.02 mag respectively, essentially eliminating the differences between wavelength bands (Figure 4.16). The corrected scatter values come quite close to the scatter expected from measurement errors (Table 1). Determining whether these errors hide further non-random behavior in TF scatter would require smaller measurement errors. Full two-dimensional velocity fields, with kinematic inclinations and modeling of disk warps and asymmetries, offer the best hope of progress (cf. Bershady & Andersen, 2000).

The existence of a color–TF residual correlation is not entirely unexpected. Bershady et al. (1999) present initial evidence for such a correlation in their intermediate-

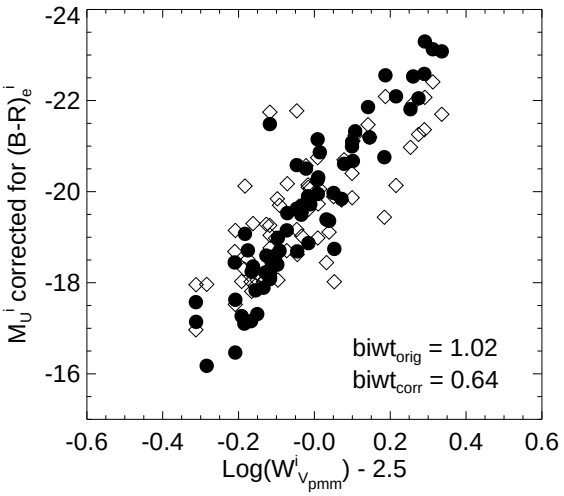

Figure 4.16.— Scatter reduction in the U-band TFR using a fit to the effective color–TF residual correlation (§4.8.2.1). Diamonds show the original points and dots show the color-corrected points. Note that the corrected points define a steeper slope due to the color-magnitude relation. The biweight scatter for the original and color-corrected magnitudes is given in mag.

redshift sample, which spans a wide range of galaxy types. Pierce & Tully (1992) find that the B-band TFR for a mixed cluster-field sample shows environmental shifts linked to galaxy colors, which suggests the possibility of a color–TF residual correlation. Giraud (1986) demonstrates reduced TF scatter in a two-color Tully-Fisher relation (essentially equivalent to our color-corrected TFR, as in Figure 4.16, but with the slope of the color–TF residual correlation assumed rather than measured). Our own analysis of Sa–Sd galaxies in the Ursa Major sample of Verheijen & Sancisi (2001) indicates that total $B-R$ colors correlate with B-band TF residuals at $\sim$3–3.5σ confidence for that sample (using unweighted inverse fits, our standard luminosity cuts, their W_{50}, and their M_B^i). The R-band correlation registers at only $\sim 2\sigma$, but we expect no better since only total rather than effective colors are available.

Most other low-redshift TF studies exclude Sa and peculiar galaxies and/or use red to near-infrared photometry, making it difficult to observe the color–TF residual correlation. For example, Courteau & Rix (1999) find only a slight, statistically insignificant color–TF residual correlation in a sample of undisturbed Sb–Sc galaxies observed in the R band. The close galaxy pairs sample of Barton et al. (2000a) includes disturbed galaxies but was not designed to evenly sample the range of spiral morphologies; again no correlation emerges using total colors and R-band TF residuals (E. Barton, private communication).

In retrospect, the color–TF residual correlation provides a natural explanation for the Sa offset discussed in §4.7.1. Unlike later type spirals in the NFGS, Sa galaxies show little dispersion in color (Jansen et al., 2000b), so they deviate from the TFR as a group, with larger offsets in bluer bands. Verheijen (1997) observes a similar phenomenon in an analysis of TF residuals for unperturbed spirals: Sa and Sab galaxies are underluminous at B by $\sim$0.5 mag (consistent with our result when normalized for slope differences, -6.7 vs. -10). The same galaxies have normal luminosities at K however, suggesting a color effect. Later types display a much wider range of TF residuals in both Verheijen's sample and our own, consistent with the much greater color dispersion observed for types Sb and later in the NFGS (Jansen et al., 2000b). We discuss a physical interpretation of the color–TF residual correlation in terms of stellar populations in §4.8.3.

4.8.2.2 Emission Line Strength

Global Hα equivalent width Jansen et al. (integrated over the entire galaxy, see 2000a) predicts TF scatter for the Sa–Sd subsample almost as well as $(B-R)_e$ (Figure 4.15). This result should not be too surprising: the two parameters are highly correlated. EW(Hα) indicates the ratio of current to past star formation, while $(B-R)_e$ reflects the balance of young vs. older stellar populations (e.g. Kennicutt et al., 1994). Substituting narrow-slit Hα or global [OII] 3727 measurements weakens the correlation.[14] The EW(Hα)–TF residual correlation intensifies in bluer TF bands, although not quite so dramatically as the color correlation. Within the luminosity-restricted spiral sample analyzed here (Figure 4.13), EW(Hα) correlates negligibly with luminosity, so no correction for luminosity dependence is necessary.[15]

Restoring spirals brighter than $M^i_R = -22.5$ to the sample, we can fit an EW(Hα)-correction formula analogous to the color-correction formula in equation 4.14:

$$\Delta M^i_R = 0.5 + 0.026 EW(H\alpha). \tag{4.15}$$

For the unweighted inverse fits in Table 1, this formula and its B and U analogues reduce scatter to 0.66, 0.67, and 0.78 mag in the R, B, and U bands respectively. The EW(Hα) correction thus performs nearly as well as the color correction in both B and R, although it underperforms in U.

To our knowledge, this paper is the first to report a correlation between TF

[14] With either substitution the correlation strength drops to borderline significance in the R band, especially using weighted fits.

[15] Of course a luminosity dependence does emerge when bright, faint, or non-spiral galaxies are included.

residuals and EW(Hα). Barton et al. (2000a) search unsuccessfully for such a correlation using narrow-slit (nuclear) Hα measurements and R-band TF residuals. These results are consistent, given that (a) our sample yields only a 2.9σ correlation between R-band TF residuals and *nuclear* EW(Hα), and (b) the Barton et al. survey targets a specific population (galaxies in close pairs) rather than a broad cross-section of galaxies.

4.8.2.3 Rotation Curve Asymmetry

Rotation curve asymmetry (defined in §4.3.2) correlates weakly with TF residuals, with 3σ significance in the B and U bands (Figure 4.15).[16]. Correcting for the RC asymmetry–luminosity correlation found in Figure 4.14 has little effect on these results.

The RC asymmetry vs. TF residual plot (Figure 4.15) may indicate a discrete effect: galaxies with asymmetry less than $\sim$2.5% show significantly lower scatter and a slight offset relative to those with higher asymmetry. This result agrees with our previous observation that pruning galaxies with high RC asymmetry reduces scatter (§4.7.2). Barton et al. (2000a) find a similar discrete effect in their close pairs sample: the R-band TF residuals of galaxies identified as severely kinematically distorted differ from the residuals for the remaining galaxies by 3σ in a K-S test. We return to the possible link between kinematic distortions and TF offsets in §4.8.3.2.

4.8.2.4 Photometric Asymmetry

The existence of a correlation between TF residuals and photometric asymmetry has not been firmly established. Zaritsky & Rix (1997) argue that I-band asymmetry and B-band TF residuals are correlated, but Barton et al. (2000a) suggest that the bulk of this correlation arises from a systematic error in TF calibration. We measure no significant correlation of R-band asymmetry with TF residuals in any passband, but we do see a 3σ correlation between B-band asymmetry and R-band TF residuals, which weakens at B and U.[17] We conclude that photometric asymmetry is a weak third parameter at best. Since asymmetry arises from multiple causes that may move TF residuals in different directions (knottiness from dust, unevenness from recent starbursts or accretion, etc.), sample selection may partly determine whether or not a correlation is detected.

[16] These correlations drop just below 3σ when we use weighted fits.

[17] On top of this odd behavior, the correlation is weaker with luminosity-independent extinction corrections.

4.8.2.5 Surface Brightness

Courteau & Rix (1999) argue against any surface brightness dependence in the TF residuals of high surface brightness spirals, while O'Neil et al. (2000) demonstrate that extreme low surface brightness (LSB) galaxies can lie well off the TFR. In our sample we detect marginal correlations between TF residuals and two measures of surface brightness. R-band central surface brightness correlates with U and B-band TF residuals at $>3\sigma$,[18] but the detection has high uncertainty due to a strong central surface brightness–luminosity correlation, and it disappears for the full sample. U-band effective surface brightness (μ_e^U, the surface brightness measured *at* r_e) displays a 3σ correlation with R-band TF residuals, but it fades in the B and U bands (Figure 4.15). However, this correlation strengthens for the full sample (§4.9.2.2).

4.8.2.6 Neutral Gas Properties

The spiral sample shows no correlation between TF residuals and neutral gas properties such as $M_{\rm HI}$, gas consumption timescale[19], and $M_{\rm HI}/L$, where we determine L in the same passband as the TF residuals to eliminate any correlation due to color. However, we compute gas masses from the catalogs of Bottinelli et al. (1990) and Theureau et al. (1998), and these catalogs do not provide HI masses for $\sim$25% of the Sa–Sd subsample. The incompleteness preferentially affects Sa and peculiar galaxies, which have the largest TF offsets, so our results should be treated with caution.

Nonetheless, our failure to detect an $M_{\rm HI}$–TF residual correlation is interesting in light of the strength of the $M_{\rm HI}$–luminosity correlation. For the Sa–Sd subsample, the $M_{\rm HI}$–luminosity correlation rivals the TFR itself in correlation strength: although weaker at B and R, it is actually stronger at U, with a Spearman rank probability of no correlation of 10^{-11}. Therefore even a small TF slope error could easily generate a false correlation between TF residuals and HI mass in this sample. The fact that we detect nothing validates our fitting and analysis procedures, as HI masses and TF velocity widths are measured completely independently. Furthermore, since the color–luminosity correlation is much weaker than the HI mass–luminosity correlation in our data, this argument supports our claim that slope errors do not drive the strong correlation we observe between color and TF residuals.

[18]The R-band correlation falls just short of 3σ. Using weighted fits, the correlation weakens in all passbands, with only the U-band correlation still reaching 3σ confidence.

[19]Gas consumption timescales are calculated by dividing the HI gas mass by the star formation rate, where gas masses are derived from the catalog HI fluxes of Bottinelli et al. (1990) and Theureau et al. (1998), and star formation rates are computed from Hα fluxes (R. Jansen, private communication) using the calibration of Kennicutt (1998) with no correction for recycling.

4.8.3 What Causes Offsets from the Spiral TFR?

The existence of a well-defined Tully-Fisher relation for spiral galaxies suggests that in large disk galaxies, the total mass of the system (traced by rotation velocity) closely couples to the mass of the stars (traced by luminosity). TF residuals may arise from any of three basic relations underlying the overall relation: (1) the observational relation between rotation velocity and total mass, (2) the fundamental structural relation between total mass and stellar mass, or (3) the observational relation between stellar mass and luminosity. For example, the Sa offset has been interpreted as evidence for a higher dark matter fraction in Sa galaxies than in other spirals, emphasizing relation (2) above. However, we have seen that the Sa offset follows a general correlation between color and TF residuals (§4.8.2.1), which may arise from stellar population variations that influence stellar M/L, emphasizing relation (3) above. Below, we examine the possibility that variations in star formation can fully explain the color–TF residual correlation, with TF offsets interpreted as luminosity offsets. We then discuss alternative explanations for the color–TF residual correlation that interpret TF offsets as velocity width offsets that correlate with color.

4.8.3.1 Luminosity Offsets

Variations in stellar M/L due to differences in stellar populations provide the simplest explanation of TF scatter. Such scatter should be higher in bluer passbands, where variations in M/L are greater, and indeed TF scatter increases from R to B to U. If stellar population differences dominate TF scatter, then the color–TF residual correlation follows naturally, provided the color–magnitude relation is relatively weak (as observed, §4.8.2.1). The only caveat is that different star formation histories yield different ratios of luminosity evolution to color evolution (LE/CE), producing different TF offsets for a given color change.[20] Therefore star formation cannot explain the color–TF residual correlation for spiral galaxies unless a broad range of disk galaxy star formation histories lead to LE/CE ratios within the range we observe.

To check the behavior of LE/CE, we examine the color *residual*–TF residual correlation, where color residuals are defined relative to the color–magnitude relation. This relation is plotted in the top right panel of Figure 4.15. If TF offsets are fundamentally luminosity offsets, then the slope of this correlation directly measures LE/CE, permitting us to compare with the predictions of population synthesis models of disk galaxy evolution. A range of slopes are consistent with the scatter in the

[20]Note that "pure" color effects such as metallicity differences must be of secondary importance given the strength of the EW(Hα) correlation.

data: in the R band, a forward fit yields 2.5, while a least-squares bisector fit (Isobe et al., 1990) yields 3.9.[21]

Bell & de Jong (2001) have used population synthesis models to predict the slope of the color vs. stellar M/L correlation for passively evolving disk galaxies with a variety of star formation histories. (here by passive evolution we mean normal star formation in a quiescent scenario, possibly with small bursts but no major bursts or external interactions). For a wide range of models, they find a slope of $\sim$2.1 in units of R magnitude vs. $B-R$. We interpret this slope as a prediction of the LE/CE ratio for two reasons. First, it holds for their single-mass (or mass-independent) models, in which M is constant and the color–luminosity relation is the same as the color residual–luminosity residual relation. Second, breaking down their mass-dependent models into mass slices (narrow ranges in model-galaxy mass) yields a similar slope of $\sim$1.9, which is invariant between slices (E. Bell, private communication). In the B band, Bell & de Jong predict a slope of $\sim$3, while we measure a value between 3.2 and 4.4 using forward and least-squares bisector fits, respectively.

To first order, the agreement between Bell & de Jong's predictions and our data clearly supports our basic interpretation of the data in terms of stellar populations. However, the exact numbers are only marginally consistent, with the data suggesting steeper slopes. This result is highly insensitive to extinction corrections, even when we omit such corrections altogether.[22] Variations in stellar-to-dark matter ratio as a function of color or luminosity could create the slope discrepancy, because the Bell & de Jong slope applies for constant stellar mass slices, whereas our slope applies for constant *total* mass slices,[23] all stacked into one relation. The sense of the discrepancy would imply that relatively bluer and brighter galaxies have higher dark matter fractions. Alternatively, our slope may be steepened by velocity width offsets that vary with color in the same sense as the luminosity offsets. This hypothesis is considered in the next section.

We prefer a third explanation, which is consistent with the interpretation of TF

[21] As discussed in §4.8.2.1, effective colors have smaller scatter than total colors, yielding more reliable slopes. However, we derive very similar slopes using total colors when we permit outlier rejection: 2.3 and 3.8 for the forward and least-squares bisector methods respectively.

[22] Specifically, we have tested extinction corrections in the style of Tully et al. (1998), Courteau (1997), and Verheijen (1997, based on the corrections in Tully & Fouque 1985), as well as testing uncorrected data. The choice of correction changes the slope by at most 0.2 compared to our standard correction (Tully et al., 1998). A larger change is possible if we adope the type-dependent q_0 described in §4.7.1 and use colors uncorrected for the color–magnitude relation; in this somewhat extreme scenario the R-band slope still falls between 1.8 and 3.0.

[23] Here we ignore variations in galaxy radius at constant velocity width, as we find no correlation between TF residuals and either effective or isophotal radii.

offsets as luminosity offsets: passively evolving disk galaxy models may simply be inadequate to describe the variety of star formation histories in a broad spiral sample. Many NFGS galaxies show morphological and kinematic evidence of disturbance, suggesting the possibility of starbursts driven by interactions, mergers, or global instabilities. Although Bell & de Jong focus on undisturbed evolutionary scenarios, they also calculate the impact of large (10% mass) starbursts on the color–M/L relation. Their Figure 5 shows that for recent starbursts ($\sim$1 Gyr old), B-band LE/CE ratios $\gtrsim$5 may not be unreasonable. The variety of evolutionary histories in our sample distinguishes it from the Ursa Major sample of Verheijen & Sancisi (2001), which represents a uniform moderate-density environment (see also §4.9.3.2). Interestingly, the Verheijen & Sancisi sample yields very shallow slopes for the TF residual vs. color residual relation, $\sim$1 in R and $\sim$2 in B (i.e., even shallower than the Bell & de Jong predictions).

4.8.3.2 Velocity Width Offsets

The steep slope of the TFR amplifies even small velocity width offsets or scatter, so any systematic velocity width trends in our data must correlate tightly with color, given the success of the color correction in reducing scatter to near measurement-error levels in all bands (§4.8.2.1). Possible sources of velocity width residuals include systematic errors in photometric inclination and symmetric or asymmetric rotation curve distortions.

If photometric inclination errors correlate with color, then velocity width offsets might drive the color–TF residual correlation. A color–inclination correlation could arise indirectly, via a color-morphology connection involving either bulge-to-disk ratios or morphological peculiarities, both of which can affect photometric inclination estimates. We cannot directly test this possibility without kinematic inclinations. However, simply raising the inclination cut from $i > 40$ to $i > 60$ tightens the color–TF residual correlation by reducing scatter without significantly changing its slope: in the R band, the range of acceptable slopes narrows to 2.5–3.4. Furthermore, we have argued that inclination errors cannot explain the Sa galaxy offset, although they may contribute to it (§4.7.1), and the high color dispersion for later types (Jansen et al., 2000b) suggests a weak link between colors and bulge-to-disk ratios. Likewise, it is hard to imagine how a heterogeneous population of peculiar galaxies could yield consistently high inclinations, as required to explain their high L/low W^i offsets.[24]

[24]Inclination errors probably do explain a few individual outliers: for example, tidal elongation may have led to an incorrect inclination for NGC 5993, the extreme outlier at -21.5 in the color-corrected U-band TFR, Figure 4.16 (also shown in the top panel of Figure 4.12). Its nominal

Systematically high inclination *errors* for peculiar galaxies would produce a net offset in the wrong direction, due to the nonlinearity of the sine function.

Rotation curve asymmetries cannot explain the color correlation either, although these asymmetries do correlate weakly with both TF residuals and $(B-R)_e$ (§4.8.2.3). Even supposing that a 5% asymmetry produces a 5% offset in rotation velocity (certainly an overestimate), that velocity offset will in turn generate a TF residual of only ∼0.2 mag. Relatively few galaxies have asymmetries that large (see Figures 4.10 and 4.15).[25]

Symmetric rotation curve distortions could be more important, if these distortions correlate with color. 2D velocity fields would be required to evaluate their role. Franx & de Zeeuw (1992) have shown that intrinsically elongated disks can produce symmetric kinematic distortions, but random orientations to the line of sight will lead primarily to scatter rather than to a systematic correlation. Galaxy interactions could create distortions that correlate with blue color, but a mechanism for shifting both radio and optical velocity widths in the same direction is not obvious. Tutui & Sofue (1997) argue that tidal interactions broaden HI linewidths, which would actually weaken the color–TF residual correlation for the HI TFR, as would HI confusion. Technically, these authors' observations do not distinguish between broadening of HI linewidths and narrowing of CO linewidths, which is likely to occur as molecular gas concentrates at the center of a galaxy where it does not sample the full velocity field (Mihos & Hernquist, 1996). Ionized gas is also likely to concentrate at the center for starburst galaxies, yielding low velocity width TF outliers due to rotation curve truncation (Barton et al., 2000a, see also §4.9.1). While this effect may create offsets for a few galaxies, it does not contribute to systematic trends: TF residuals show no significant correlation with rotation curve extent.

4.9 The TFR for the General Galaxy Population

We now turn to the full sample of NFGS emission-line galaxies, with no restrictions on luminosity or morphology, but still requiring $i > 40$. Table 2 gives fitted TF

photometric inclination is 42 degrees, but its inner parts appear closer to face on. If its true inclination were 20 degrees it would shift by ∼2.8 mag, bringing it much more in line with the TFR. However, NGC 5993 is not at all typical: its offset does *not* follow the color–TF residual correlation. In fact, on average, spirals with peculiarities have slightly lower apparent inclination than the rest of the spiral sample (63° vs. 66°).

[25]The fact that galaxies with low RC asymmetry have low TF scatter (§4.8.2.3) thus seems to reflect not the low asymmetries *per se* but rather the tendency for galaxies with low TF scatter to *also* have low RC asymmetry.

Table 2. Tully-Fisher Fits to the Full Sample [a]

Band	Wtd Inv	Bivariate	Unwtd Inv	Unwtd Inv HI
		Slope		
U	-9.43±0.21	-7.88±0.25	-8.89±0.21	-8.42±0.16
B	-9.62±0.21	-8.27±0.24	-9.01±0.21	-8.43±0.16
R	-9.90±0.21	-8.75±0.23	-9.20±0.22	-8.55±0.16
		Zero Point		
U	-19.69±0.04	-19.80±0.04	-20.00±0.04	-19.88±0.03
B	-19.76±0.04	-19.86±0.04	-20.03±0.04	-19.86±0.03
R	-20.73±0.04	-20.83±0.04	-21.00±0.04	-20.81±0.03
		Scatter [b]		
U	1.24(0.78)	1.04(0.68)	1.17(0.75)	1.07(0.53)
B	1.18(0.79)	1.01(0.70)	1.10(0.75)	1.02(0.53)
R	1.15(0.81)	1.01(0.73)	1.07(0.76)	0.99(0.53)

[a]Fit results from weighted inverse, bivariate, and unweighted inverse fitting techniques for optical ($W_{V_{pmm}}$) and radio (W_{HI}) T-F calibrations (see §4.5). Errors given are the formal statistical errors from a two-step fit, see §4.5. We require $i > 40$.

[b]Measured biweight scatter and predicted scatter (in parentheses) from measurement errors.

parameters for this sample in the U, B, and R bands, with optical RC results based on 108 galaxies (107 at U) and HI linewidth results based on 76 galaxies (75 at U). The R-band TFR is shown in Figure 4.17.

As illustrated in Figure 4.18, scatter is dramatically higher for the full sample than for the spiral sample of §4.6–4.8. Including non-spiral and dwarf galaxies adds 0.77 mag of scatter in quadrature, yielding a total scatter of 1.07 mag.[26] Faint non-spiral galaxies are responsible for most of the new scatter, so the relative importance of the morphology and luminosity extensions is unclear. E/S0's brighter than $M_R^i = -20$ behave much like Sa galaxies, with a slight low L/high W^i offset. Neistein et al. (1999) observe a similar TF offset for S0 galaxies using stellar kinematics.

[26]Two of the emission-line galaxies in the full sample are classified as type E. One might question the wisdom of assigning any inclination to these. We include them for completeness, noting also that one is a very disky elliptical.

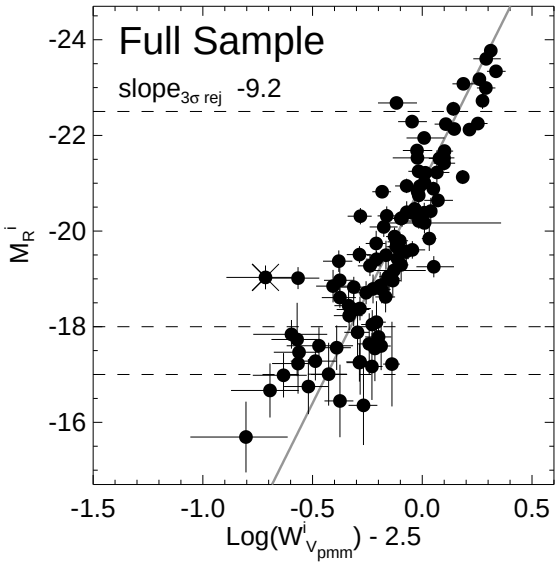

Figure 4.17.— TFR for the full sample, including all morphologies and luminosities but restricted to $i > 40$. Dashed lines indicate luminosity cuts used for Spearman rank tests (§4.9.1–4.9.2, see also §4.8.1). The gray line shows an unweighted inverse fit to all points, and the X marks a point automatically rejected by that fit as a $>3\sigma$ outlier.

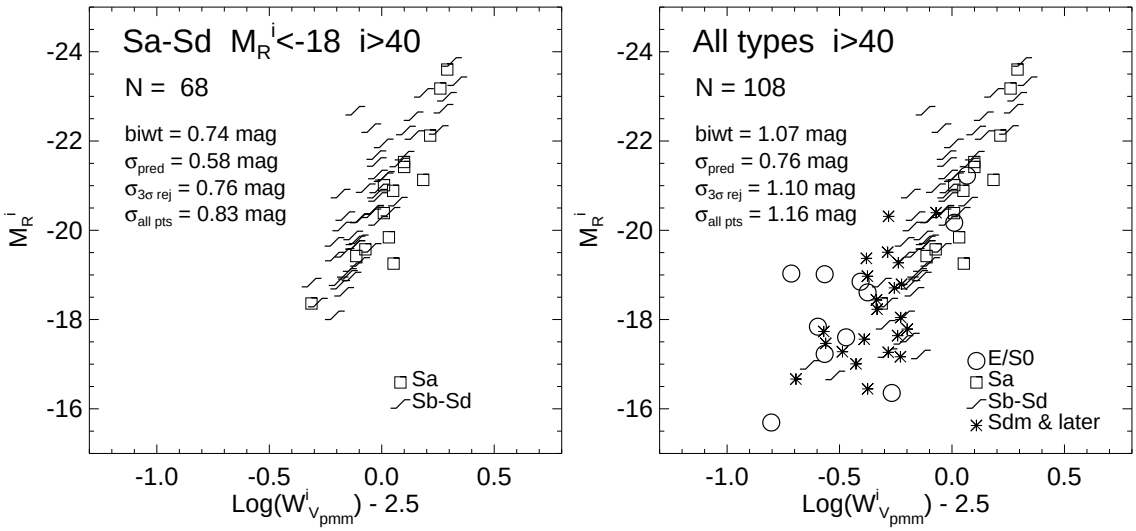

Figure 4.18.— Increase in TF scatter caused by extending the sample in morphology and luminosity. Scatter measurements are relative to an unweighted inverse fit.

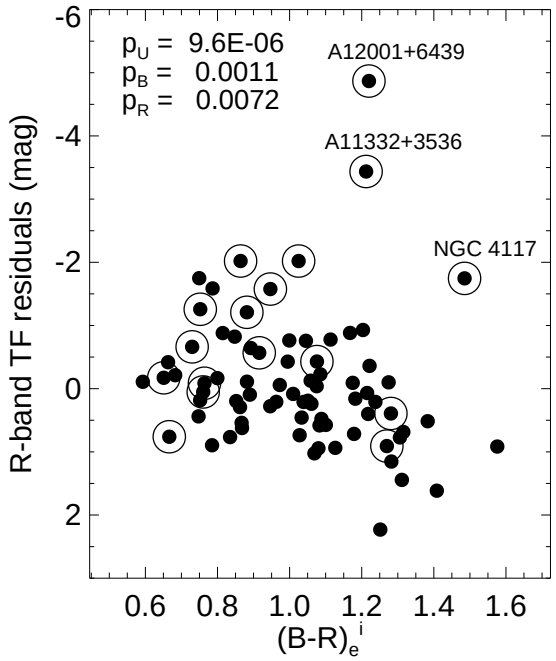

Figure 4.19.— The correlation between TF residuals and $(B-R)^i_e$ color for moderately bright galaxies of all morphologies. As in §4.8 we require $-18 < \mathrm{M}^{\mathrm{i}}_{\mathrm{R}} < -22.5$ and $i > 40$; see Figure 4.15. Circled points represent galaxies with morphological type later than Sd or earlier than Sa. Most circled galaxies follow the spiral correlation well, except for three clear outliers (discussed in §4.9.1). The Spearman rank probability of no correlation between the $(B-R)^i_e$ and TF residuals in each optical band is given as p_{band}. Only R-band TF residuals are shown.

4.9.1 Physical Sources of Scatter in a Morphology-Blind TFR: The Trouble with Emission-Line S0's

Here we broaden the spiral sample of §4.8 to include all morphologies, staying within the luminosity limits used in §4.8 (Table 3 and Figure 4.17) and requiring $i > 40$. We extend the luminosity range 1 mag fainter to include dwarfs in the next section.

Surprisingly, adding non-spirals to the sample weakens the effective color and global EW(Hα) correlations significantly — in fact the $(B-R)_e$ correlation falls below 3σ at R. Yet the rotation curve asymmetry and *nuclear* EW(Hα) correlations grow, the μ^U_e correlation stays about the same, and we see a hint of a new correlation with gas consumption timescale.

However, these patterns should not be taken at face value. Figure 4.19 plots TF residuals against $(B-R)_e$ for the expanded sample. Most non-spiral galaxies

(circled in the figure) follow the correlation established by spiral galaxies quite well, albeit with slightly larger scatter. Just three emission-line S0 galaxies (labeled by name) deviate sharply, falling so far off the correlation that they partly mask its statistical signal, showing red colors $\gtrsim$1.2 together with overluminosities of $\sim$2-5 mag (or too-slow rotation speeds).[27]

Inclination errors cannot explain the odd behavior of these galaxies, as all show disky morphologies and inclinations of $\sim$60-70 degrees. Rather, we suggest that the kinematics we measure for these galaxies do not trace the rotation of the galaxy disk, based on a review of their properties. Two of the three galaxies show very bright nuclei, one of which is classified as a Seyfert II (NGC 4117); the third galaxy is a known starburst galaxy. This central activity contributes to the TF residual–nuclear EW(Hα) correlation noted above. We calculate rapid gas consumption timescales of $\sim$2 Gyr for the two galaxies for which we have HI masses. One of the galaxies probably has an inclined counterrotating gas disk (A11332+3556, Kannappan & Fabricant, 2001a). Two of the galaxies have truncated rotation curves with extent much less than $1.3r_e$, although one RC turns over and appears to be normal (NGC 4117). The third galaxy's RC displays velocity reversals and reaches only to $1.31r_e$ (A12001+6439).

The truncated RCs and disturbed gas dynamics found in the S0 outliers suggest that their deviant velocity widths may be related to their central activity. These phenomena are consistent with recent interaction or merger/accretion events. As discussed by Barton et al. (2000a), interacting galaxies may display radially truncated emission due to centrally concentrated starbursts, leading to artificially low velocity widths. Interactions and mergers may also generate non-coplanar gas and stellar rotation in early-type galaxies (Kannappan & Fabricant, 2001a; Haynes et al., 2000), in which case low gas velocities will be measured because the spectrograph slit P.A. is aligned to the stellar major axis rather than the gas major axis. We have already commented on the inclined gas disk in A11332+3556. NGC 4795 (the one Sa galaxy that falls on the high L/low W^i side of the TFR in the lower right panel of Figure 4.18) also shows evidence of decoupled gas (Kannappan & Fabricant, 2000b).[28] Such galaxies may be flagged and pruned from a TF sample by virtue of their failure to follow the color–TF residual correlation.

[27] HI linewidths are available for two of the three S0 outliers; these two galaxies are clear outliers from the HI TFR as well, although the HI residuals are smaller than the optical RC residuals.

[28] Our sample also contains a few counterrotators whose gas has already settled into the plane of the disk, so that they are not TF outliers. Presumably they once were.

4.9.2 Physical Sources of Scatter in the Dwarf Extension of the TFR

Figure 4.20 plots third parameter–TF residual correlations for the full sample, with luminosity cuts extended to include dwarf galaxies brighter than $M_R^i = -17$ (see Table 3). Adding dwarfs dilutes the correlations of TF residuals with $(B-R)_e$ and EW(Hα) severely; for R-band TF residuals they become scatterplots. The only third-parameter correlations that reach 3σ significance in the R band involve parameters that showed weak or nonexistent correlations for the spiral sample: rotation curve asymmetry, U-band effective surface brightness, and gas consumption timescale.

4.9.2.1 Rotation Curve Asymmetry

Asymmetries in rotation curves arise from multiple sources including turbulence, bars, tidal distortions, early or late-stage infall, and satellite accretion. Most of these underlying phenomena are likely to enhance star formation, qualitatively explaining the sense of the correlation in Figure 4.20 as well as its stronger statistical signal in bluer passbands. However, the scatter and substructure in the correlation suggest that the RC asymmetry–star formation connection may be complex. As we saw in §4.8.2.3, TF scatter stays very low for RC asymmetries less than $\sim$2.5%, then increases abruptly. Also, faint-galaxy asymmetries exhibit an interesting split. On the the high L/low W^i side of the TFR, several dwarf galaxies show extreme RC asymmetries $\gtrsim$10% (higher than expected from the luminosity–RC asymmetry relation, Figure 4.14), while on the other side of the TFR, RC asymmetries are more modest (Figure 4.21; see also §4.9.2.4).[29]

4.9.2.2 U-Band Effective Surface Brightness

If U-band effective surface brightness (μ_e^U) measures the surface density of recent star formation in galaxy disks, then high μ_e^U (numerically small values) should correlate with high global star formation activity, consistent with the observed TF residual–μ_e^U correlation. However this view may be too simplistic, because galaxies ranging from undisturbed spirals to emission-line S0's with kinematically decoupled gas all seem to follow the same correlation, albeit with very large scatter. Given the constancy

[29]The RC asymmetry–luminosity relation is stronger than the color–magnitude relation for the full sample (Figure 4.14). If we use a linear fit to the RC asymmetry–luminosity relation to subtract out a luminosity-dependent RC asymmetry zero point and define "RC asymmetry residuals," the correction boosts the significance of the TF residual–RC asymmetry correlation to $\sim 3.5\sigma$ in R.

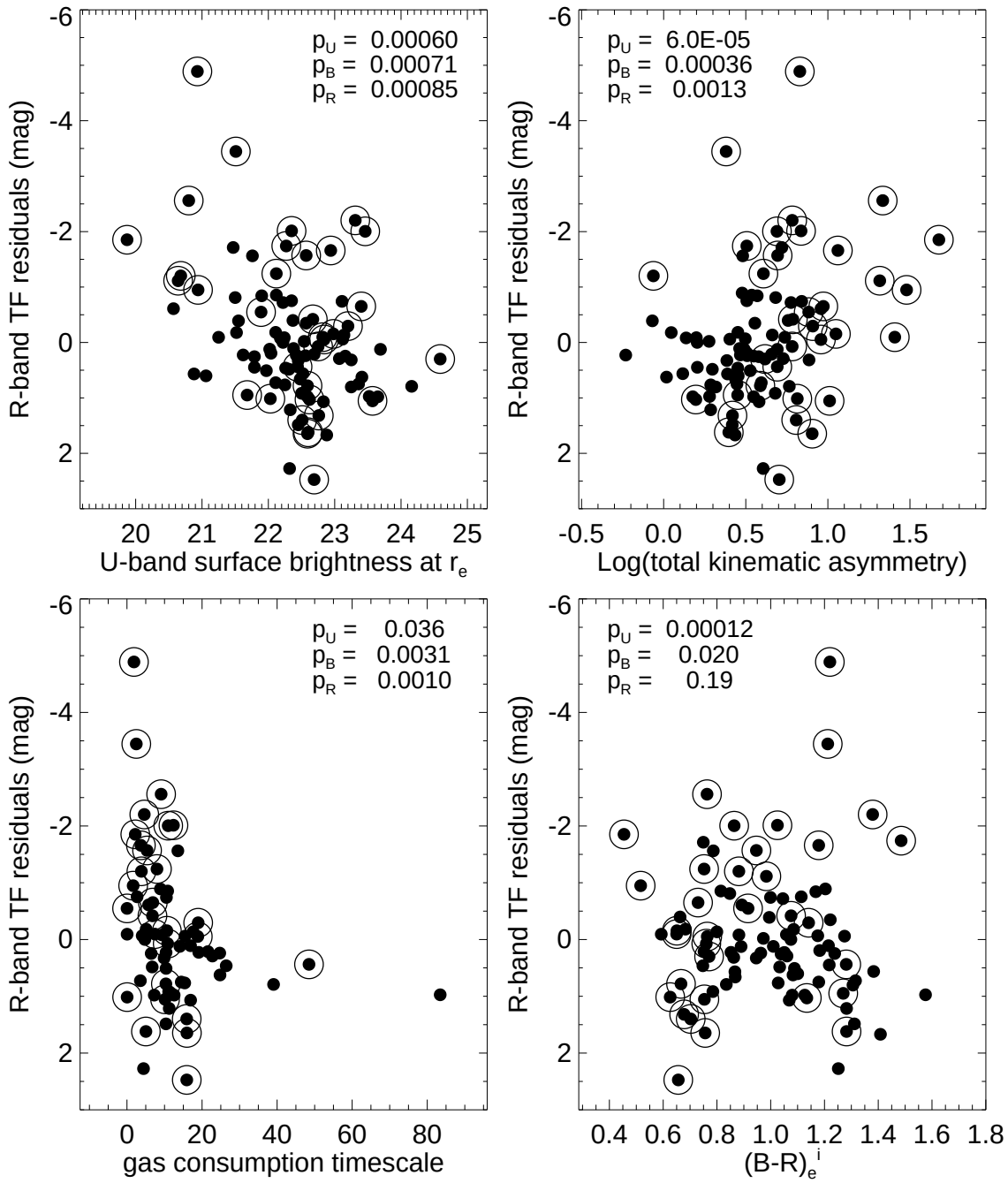

Figure 4.20.— TF residuals vs. physical properties of the full sample (all morphologies, $i > 40$, $-17 < M_R^i < -22.5$, see §4.9.2 and Figure 4.17). Circled points represent galaxies not included in the normal-luminosity spiral sample of §4.8. The Spearman rank probability of no correlation between the parameter and TF residuals in each optical band is given as p_{band}. Only R-band TF residuals are shown.

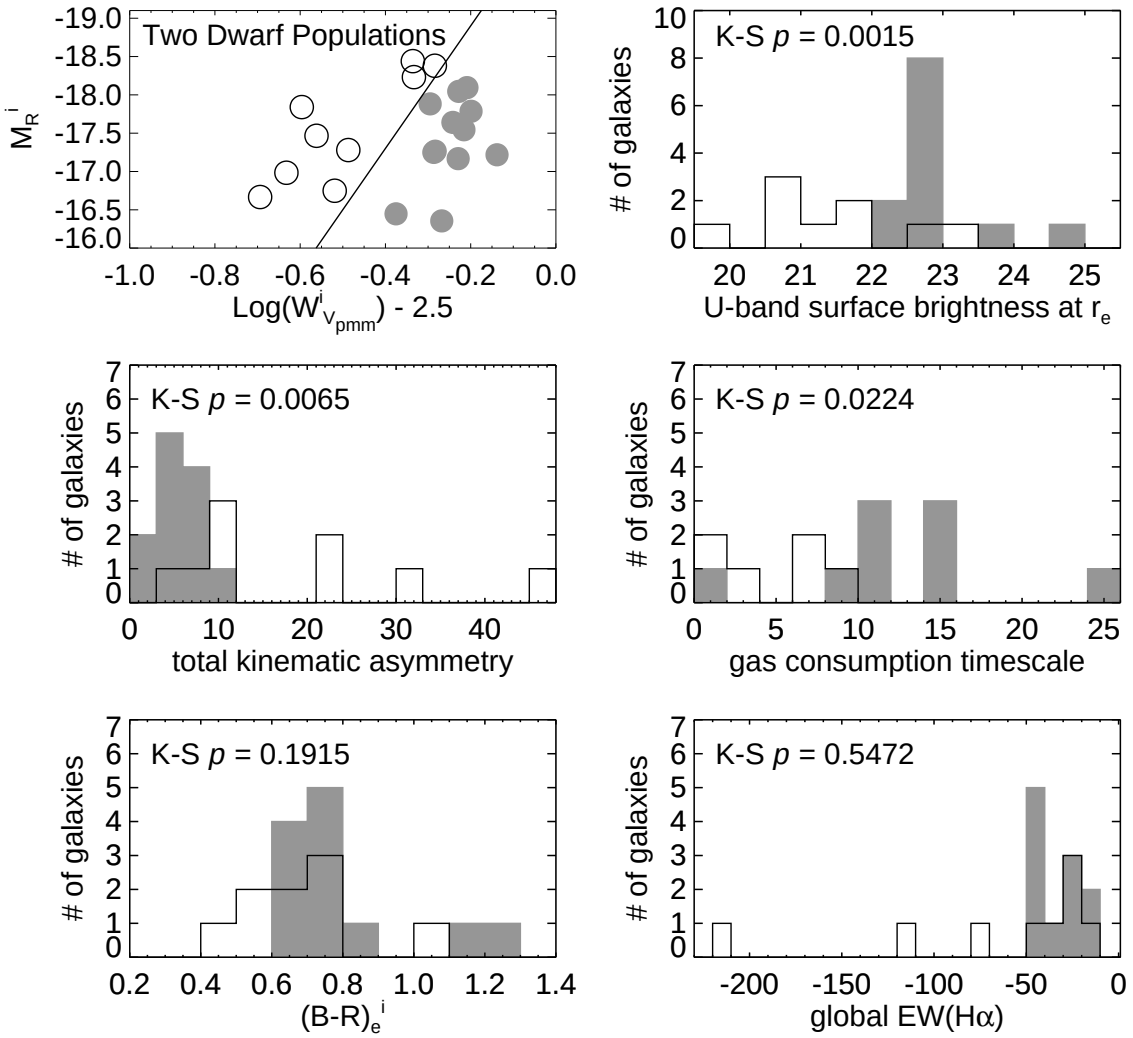

Figure 4.21.— Physical properties of dwarf galaxies on either side of the TFR. Dwarfs with large W^i (or low L) are shown in gray, while those with small W^i are outlined in black. Each panel lists the Kolmogorov-Smirnov probability that the two sets of dwarfs were drawn from the same parent population with respect to the property shown. Here "dwarf" means anything fainter than $M_R^i = -18.5$; the luminosity cuts used for the third-parameter tests are *not* applied. Galaxies with truncated RCs ($<1.3r_e$) have been excluded from the figure because of uncertain location with respect to the TFR (however they do appear in Figure 4.22). Restoring these galaxies only slightly weakens the K-S test results, as the excluded galaxies include most of our centrally active dwarf S0 galaxies, whose properties generally reinforce the results shown here except the color histograms (§4.9.1). The reference TFR is the dwarf TFR shown in the top left panel of Figure 4.22.

of the Spearman test significance for this correlation whether using U, B, or R-band TF residuals (Figure 4.20), we suggest that variations in μ_e^U may track not only star formation but also structural differences between classes of galaxies located in different parts of the L–W^i plane, such as differences in the concentration of light or the velocity width at a given luminosity. Dwarfs on opposite sides of the TFR have different μ_e^U distributions (Figure 4.21), analogous to the different rotation curve asymmetry distributions discussed in the previous section. While low to moderate surface brightnesses occur on both sides of the TFR, high surface brightnesses occur only on the high L/low W^i side.

4.9.2.3 Gas Consumption Timescale

Typical gas consumption timescales also appear to differ for dwarfs on the two sides the TFR, although this result relies on incomplete HI data (§4.8.2.6). Dividing the correlation plot (Figure 4.20) with an imaginary horizontal line at zero, one sees only a few points with low L/high W^i (positive) residuals and extremely short gas consumption timescales. By contrast, short gas consumption timescales are the norm for galaxies with negative residuals. Most of the latter set are low-luminosity non-spirals, which explains the emergence of a gas consumption timescale correlation in the full sample, where there was no correlation in the spiral sample of §4.8.

4.9.2.4 Is the Dwarf Split Real?

We have argued that if we divide the dwarf population into two groups with positive and negative offsets from the TFR, the groups have distinct physical properties (summarized in Figure 4.21). Although K-S tests of the significance of the differences between the groups yield only 2–3σ for any given property, the same behavior is seen for three completely independent parameters: rotation curve asymmetry (based on high-resolution spectra), μ_e^U (based on surface photometry), and gas consumption timescale (based on catalog HI data and NFGS spectrophotometry). Furthermore, replacing optical velocity widths with HI linewidths preserves the division. Similar results have also been reported by Stil & Israel (1998) and Pierini (1999), considering only kinematic properties. These authors identify a rotationally supported dwarf population on the faint side of the TFR and a population with comparable rotational and random velocities on the bright side (where we measure high rotation curve asymmetries).

For the NFGS, the two dwarf populations are separated by $\sim$2 mag in the mean. We have considered whether systematic effects might create such a split. Because the

two sets of dwarfs show similar distributions in inclination and morphology, correlated inclination errors are unlikely.[30] The rotation curve asymmetries we measure are too small to produce such a large offset.

Correlated distance errors might be a concern. Both dwarf populations show broad distributions in R.A.-Dec.-redshift space, but due to the NFGS selection procedure, the two sets of dwarfs in Figure 4.21 have systematically different recession velocities: 500–1300 and 700–1600 km s^{-1} for underluminous and overluminous dwarfs respectively, with over half the underluminous set in the range 500–700 km s^{-1} (measured with respect to the Local Group). To test whether peculiar velocities or local flows may have affected our distance estimates and produced a spurious bifurcation in luminosities, we have substituted distances estimated by a number of techniques. These include: (1) Hubble-law distances assigned using group recession velocities rather than individual galaxy recession velocities (see Tully, 1988; Tully et al., 1992);[31] (2) absolute distances derived from the light-to-mass model of Tully et al. (1992); (3) Hubble-law distances with and without corrections for Virgocentric infall (§4.4.1 and/or for the Local Anomaly Han & Mould (1990). The segregation of the two dwarf populations is robust under all of these substitutions, with the caveat that many of the overluminous (low velocity width) dwarf galaxies lack distances from methods (1) and (2).

The physical mechanisms behind the rapid gas consumption and disturbed kinematics of the overluminous dwarfs are uncertain. Interactions are an obvious possibility; however, without deep wide-field images we cannot evaluate the frequency of close companions for the two populations, particularly given the possibility of relatively faint neighbors. However, it is intriguing to note that deep survey work by Taylor et al. (1996) has demonstrated a statistically higher rate of companions near starbursting dwarfs than near LSB dwarfs (see also Pustilnik et al., 2001). The analogy is suggestive rather than exact, as our two dwarf populations do not show a definitive split in EW(Hα), although the three most extreme starbursting dwarfs do fall on the bright side of the TFR (Figure 4.21).

[30]This statement applies to the two groups of dwarfs shown in Figure 4.21. The figure excludes galaxies with truncated rotation curves, as their location in the L–W^i plane is uncertain. Had these been allowed, an excess of emission-line S0 galaxies would have appeared on the bright side of the TFR.

[31]This substitution yields one large shift (0.6 mag toward higher luminosity), for a galaxy assigned to the Ursa Major Cluster on somewhat shaky grounds (UGC 6446). Its projected location lies near the cluster outskirts and its velocity approaches the cluster lower limit.

4.9.3 Two Dwarf Galaxy Populations and the Slope of the TFR

As noted by Pierini (1999), the existence of two dwarf populations complicates TF slope measurements. For the full sample, we find a linear TF slope with no break at low luminosities (top left panel of Figure 4.22). However, different sample selection criteria may favor one dwarf population over the other, with consequences for the faint-end slope.

4.9.3.1 Physical Continuity of the TFR at Low Luminosities

If we interpret the TFR as a physical relation between luminosity and rotation velocity for passively evolving disk galaxies, then it should apply only to undisturbed rotationally supported systems. Dwarf galaxies on the low L/high W^i side of the TFR best meet this description. These galaxies show moderate rotation curve asymmetries, indicating that they are probably rotationally supported. In addition, their long gas consumption timescales and low U-band effective surface brightnesses appear consistent with quiescent evolution.[32]

Figure 4.22 demonstrates the effect of selecting TF samples from the full NFGS according to the properties of this group of dwarfs, i.e. low kinematic asymmetry, long gas consumption timescale, or low U-band effective surface brightness. Each panel shows separate TF fits for galaxies above and below $M_R^i = -18.5$. We cannot tightly constrain the slope of the dwarf TFR, due to small number statistics and a short lever arm. Nonetheless, Figure 4.22 clearly suggests a faint-end discontinuity in the TF slope for undisturbed, rotationally supported galaxies: dwarf galaxies appear underluminous when compared to the extrapolated bright-galaxy TFR.

Breaks in the faint-end slope of the TFR have been previously observed for extremely late type spirals (Matthews et al., 1998) and LSB dwarfs (McGaugh et al., 2000). McGaugh et al. demonstrate that a straight TF slope (the "baryonic Tully-Fisher relation") can be restored for LSB dwarfs by mathematically converting their gas into stars and correcting the luminosity for these unformed stars. This procedure does not work very well for our faint galaxies, but McGaugh et al. see significant effects primarily for galaxies fainter than our cutoff of $M_R^i \sim -16$.

[32]Note that photometric "normalcy" is not a useful criterion for dwarfs, as almost all are lumpy and asymmetric, so defining what is "peculiar" becomes extremely difficult.

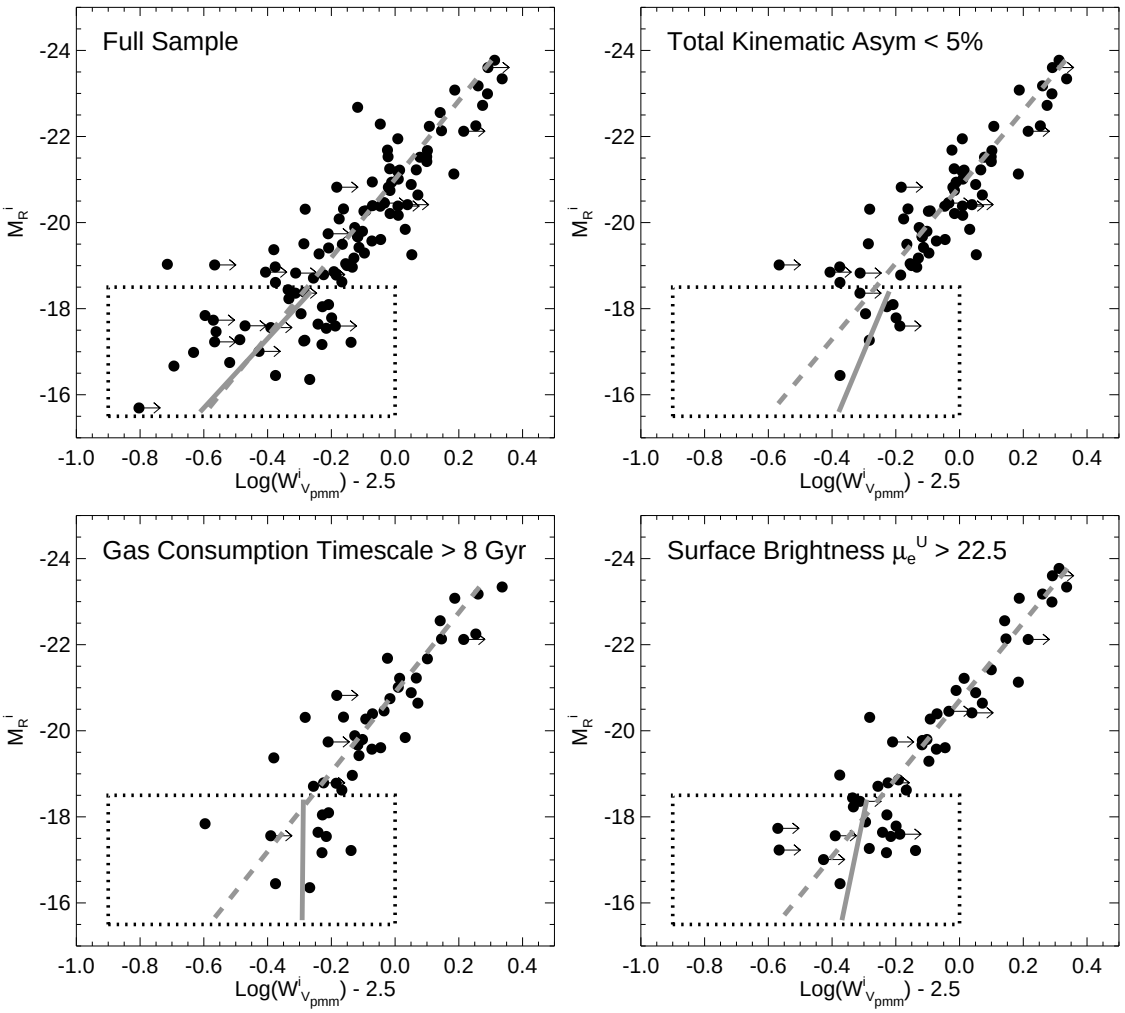

Figure 4.22.— Effects of sample selection on the faint-end slope of the TFR. Each panel shows galaxies that meet the selection criterion indicated and have inclinations $i > 40$. Arrows mark galaxies whose rotation curves are truncated at less than $1.3r_e$; these galaxies may have velocity widths larger than we measure. The dashed and solid gray lines show the TFR for galaxies brighter and fainter than -18.5, respectively; the fainter set of galaxies fall within the box and the rest lie above it. The dashed line determined by the brighter galaxies extends into the box for reference only. Gas consumption timescales are calculated by dividing the HI gas mass by the star formation rate, where gas masses are derived from the catalog HI fluxes of Bottinelli et al. (1990) and Theureau et al. (1998), and star formation rates are computed from Hα fluxes (R. Jansen, private communication) using the calibration of Kennicutt (1998) with no correction for recycling.

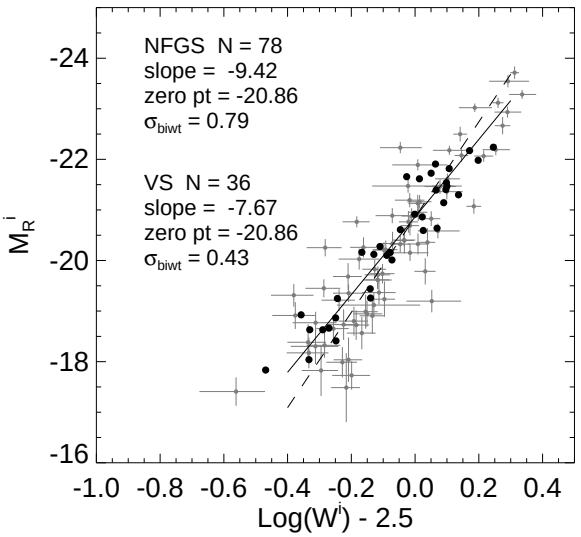

Figure 4.23.— Comparison of TFRs for the NFGS (gray) and for the Ursa Major sample of Verheijen & Sancisi (2001, black), with both samples restricted to types Sa and later, $M_B < -16.8$, and $i > 45$. Three of VS's galaxies have obviously discrepant W_{50} values (NGC 3985, UGC 7089, and NGC 4218), so for these we substitute W_{20} − 20 km s^{-1} (§4.3.3). See also caption to Figure 4.8.

4.9.3.2 Environmental Dependence in the Dwarf TFR

Except for its restriction to a single environment, the Ursa Major HI sample of Verheijen & Sancisi (2001, hereafter VS) is almost as broadly representative as the NFGS. Figure 4.23 directly compares our TFR with theirs, restricting both data sets to $M_B < -16.8$, $i > 45$, and type Sa or later. Within these limits the HI sample is nearly complete, with only one Sa and two Sm galaxies missing.

Although the zero points for the two samples agree to within <0.01 mag, the slopes differ visibly, with a discrepancy of ∼0.5 mag at the faint end. At the bright end, the fits disagree but the data do not: we have already noted the asymmetric TF scatter of bright NFGS galaxies (§4.8.1). In light of the color–TF residual correlation for spiral galaxies (§4.8.2.1), this asymmetric scatter may simply reflect the rarity of very luminous blue galaxies.

Below $M_R^i = -19$, however, the slope difference traces a real divergence between the two data sets, and this difference cannot be attributed to systematic errors. Extinction corrections, distance calibrations, and linewidth definitions have been applied

consistently to both samples (Figure 4.23).[33] Distance errors cannot easily account for the faint-end structure of the NFGS TFR (§4.9.2.4), and such errors should be tiny for the Ursa Major sample, except in cases of mistaken membership assignments. It is possible that significant cluster depth can lead to an artificially shallow TF slope, as intrinsically faint galaxies will be detected only on the near side of the cluster in an apparent-magnitude limited sample, but a deep survey for dwarfs in Ursa Major has uncovered few galaxies missed by the initial survey (Trentham et al., 2001).

We conclude that the slope offset between the Ursa Major and NFGS data sets reflects a real difference between the faint galaxy populations of the two surveys, most naturally attributed to environmental differences. Whereas the NFGS includes a wide range of field and cluster environments, the Ursa Major sample was drawn from a single, rather unusual cluster: a moderate overdensity of spiral galaxies that lacks any discernible core, contains no elliptical galaxies, and includes few dwarfs (Tully et al., 1996).

Trentham et al. (2001) infer from the scarcity of dwarf galaxies in Ursa Major that the cluster collapsed late, so that its dwarf halos formed after reionization when conditions were poor for star formation. The few dwarfs they do find are strongly clustered and often located near larger galaxies; Trentham et al. suggest that locally rapid collapse times may have enabled these dwarfs to form.

We would add that if the Ursa Major dwarfs have properties similar to the NFGS dwarfs that fall on the bright side of the TFR, consistent with the Ursa Major dwarfs' location in the L–W^i plane, then many of them may be kinematically disturbed and actively evolving (cf. §4.9.2.4).[34] Their clustering properties suggest that galaxy interactions have probably played a large role in their evolution; some of them may actually owe their existence to interactions between larger galaxies, as Trentham et al. recognize (Mirabel et al., 1992, cf.). Conversely, the NFGS–VS slope difference suggests that passively evolving, rotationally supported dwarfs like those found on the faint side of the NFGS TFR may be rare in the Ursa Major environment, perhaps due to the timing of reionization as suggested by Trentham et al.

[33]Substituting UGC-derived inclinations for VS's inclinations has little effect on slope or scatter for the Ursa Major sample. The finite precision of the UGC axial ratios creates quite a bit more scatter for the NFGS, because NFGS galaxies are much smaller on the sky than most Ursa Major galaxies.

[34]Our analysis in §4.9.2.4 focused on galaxies fainter than $M_R^i = -18.5$, but the exact luminosity break is not critical. Figure 4.18 shows that non-spiral morphologies typical of dwarfs are quite common below $M_R^i = -19$.

4.10 Conclusions

The Nearby Field Galaxy Survey offers an ideal sample for exploring the link between offsets from the Tully-Fisher relation and the evolutionary states of galaxies. Galaxies in the NFGS were selected from the CfA 1 redshift survey without preference for morphology or environment and span a wide range of luminosities, $-23 < \mathrm{M_B} < -15$. Using UBR photometry, optical rotation curve data, and HI linewidths, we have analyzed TF residuals for two subsamples of the NFGS, a sample of Sa–Sd spirals brighter than $\mathrm{M_R^i} = -18$ and an extended sample including dwarfs and non-spiral galaxies.

Within the spiral sample, we find strong third-parameter correlations between TF residuals and both $B-R$ color and EW(Hα). The cleanest correlations are achieved using effective colors (measured within the effective radius) and global equivalent widths (integrated over the entire galaxy). Using the color–TF residual correlation in each TF band to define a color-correction term to the TFR, we reduce scatter to a single constant value across the R, B, and U bands, eliminating the usual trend of increasing scatter with bluer passbands. The remaining scatter of $\sim$0.65 mag (at a slope of -10) approximately equals the scatter we expect from measurement errors. An EW(Hα)-correction term performs equally well for the R and B-band TFRs and almost as well for the U-band TFR.

The color and EW(Hα) correlations are continuous, but their statistical signal is strongly driven by two morphology classes: peculiar galaxies (by which we mean recognizable spirals with oddities such as warps, multiple nuclei, or interacting companions) located on the high luminosity/low velocity width side of the TFR, and Sa galaxies located on the low luminosity/high velocity width side of the TFR. This result offers a different perspective on the longstanding debate over the Sa offset: while we find a genuine offset that does not arise from Malmquist bias, its existence proves not that Sa galaxies rotate faster than other types, but that Sa galaxies are consistently red.

Differences in star formation history offer the simplest explanation for the color–TF residual correlation: luminosity and color evolution naturally go hand in hand. If we interpret TF residuals as luminosity residuals, then the slope of the color–TF residual correlation can be directly compared with the predictions of population synthesis models of disk galaxy evolution. The slopes we find using R and B band TF residuals are similar to, but somewhat steeper than would be predicted based on the passively evolving model galaxies of Bell & de Jong (2001). Our steeper slopes may mean that many spirals experience starbursts in addition to more gradual evolution,

perhaps triggered by interactions or minor mergers as suggested by the disturbed morphology and kinematics of many of the bluer galaxies. However, the present data cannot conclusively rule out systematic trends caused by kinematic distortions or inclination errors that correlate with galaxy color: such trends are unlikely to explain the entire color–TF residual correlation but may affect its slope. A systematic correlation between stellar-to-dark matter ratios and galaxy color could also steepen the correlation, if bluer galaxies have more dark matter at constant total mass.

Removing the spiral morphology restriction, we find that most non-spiral galaxies brighter than $M_R^i = -18$ follow the color–TF residual and EW(Hα)–TF residual correlations established by spiral galaxies, but with greater scatter. A few emission-line S0 galaxies at the faint end of the included range deviate strongly from both the TFR and the color–TF residual correlation; these galaxies all show starburst or AGN activity and anomalous gas kinematics.

Dwarf galaxies fainter than $\sim M_R^i = -18$ do not follow the color–TF residual correlation. However, dwarfs on the high luminosity/low velocity width side of the TFR have higher rotation curve asymmetries, higher U-band effective surface brightnesses, and shorter gas consumption timescales than dwarfs on the low luminosity/high velocity width side of the TFR. These properties suggest that many of the high L/low V dwarfs are "disturbed," while the low L/high V dwarfs are likely to be passively evolving, rotationally supported systems.

This split in dwarf properties implies that the faint-end slope of the TFR depends on the sample. We find no break in slope for dwarf galaxies in the full NFGS sample. If we select for rotationally supported, passively evolving galaxies at all luminosities, we find evidence for a break toward steeper slope at the faint end of the TFR. On the other hand, the dwarf galaxies in the Ursa Major cluster sample of Verheijen & Sancisi (2001) define a relatively shallow slope; these galaxies occupy the same part of the TF plane as the more disturbed class of NFGS dwarfs. The formation of dwarfs comparable to the more passively evolving class of NFGS dwarfs may have been inhibited in Ursa Major, if reionization preceded the cluster collapse and created conditions hostile to early dwarf galaxy formation, as recently proposed by Trentham et al. (2001).

We thank Eric Bell for performing additional model calculations to answer our questions, Betsy Barton for sharing information on technical aspects of Tully-Fisher analysis, Rolf Jansen for providing data and general expertise, and Margaret Geller, Douglas Mar, and Kristin Nelson-Patel for helpful discussions. We also thank John Huchra for a critical reading of the manuscript. This publication makes use of data

products from the Two Micron All Sky Survey, which is a joint project of the University of Massachusetts and the Infrared Processing and Analysis Center/California Institute of Technology, funded by the National Aeronautics and Space Administration and the National Science Foundation. This publication also makes use of the Digital Sky Survey (POSS plates), based on photographic data of the National Geographic Society – Palomar Geographic Society to the California Institute of Technology. The plates were processed into the present compressed digital form with their permission. The Digitized Sky Survey was produced at the Space Telescope Science Institute under US Government grant NAG W-2166. SJK acknowledges support from a NASA GSRP fellowship.

Chapter 5

Calibrating Evolution in the Tully-Fisher Relation†

†Kannappan, S. K., Fabricant, D. G., & Franx, M.

ABSTRACT

We reevaluate evidence for luminosity evolution in the intermediate-redshift Tully-Fisher relation (TFR), focusing on the spatially resolved kinematic data sets of Vogt et al. (1997) and Simard & Pritchet (1998). We use low-z data from the Nearby Field Galaxy Survey (NFGS) to match the intermediate-z studies' sample selection criteria, analysis techniques, and data quality. The passively evolving disk galaxy sample of Vogt et al. shows no luminosity evolution within the errors, approximately confirming these authors' results. The [OII]-selected sample of Simard & Pritchet shows $\lesssim$0.5 mag of luminosity evolution, substantially less than the 1.5–2 mag originally reported; we trace about half of the original offset to radial truncation in the S&P rotation curves. Looking toward future studies of evolution in the TFR, we also provide a new calibration of the low-z TFR designed for direct comparison with intermediate and high-z data, based on a morphology-blind sample of bright emission-line galaxies. Within this sample, TF residuals vary systematically as a function of color and Hα equivalent width.

5.1 Introduction

Two processes lie at the heart of galaxy evolution: mass assembly and star formation. For disk galaxies, the redshift-dependence of the correlation between rotation velocity and luminosity (a.k.a. the Tully-Fisher relation or TFR, Tully & Fisher, 1977) offers a powerful probe of the evolving relationship between total mass and stellar light.

In the absence of mergers or significant accretion, galaxy masses are fixed, and luminosity evolution simply shifts the zero point of the TFR (or both the zero point and the slope, if faint galaxies show differential luminosity evolution relative to bright galaxies). Several studies have sought to measure luminosity evolution in the intermediate-z TFR, motivated by the suggestion that the excess of faint blue galaxies in deep photometric surveys might indicate that galaxies were brighter in the past (Forbes et al., 1996; Rix et al., 1997; Simard & Pritchet, 1998; Vogt et al., 1997; Bershady et al., 1999).

Conflicting results have emerged. Both Rix et al. (1997) and Simard & Pritchet (1998) measure apparent luminosity enhancements of $\sim$1.5–2 mag at $z \sim 0.3$, using samples selected for strong [OII] emission. However, Vogt et al. (1997) and Bershady et al. (1999) find much smaller zero point shifts at $z \sim 0.5$ and 0.3, respectively, using samples selected by morphology and color criteria less likely to bias the sample toward actively star-forming galaxies.

Our recent work on third-parameter dependences in the residuals of the TFR for a morphology-blind low-z field galaxy sample (Kannappan et al., 2001b, hereafter KFF) motivates us to reexamine the intermediate-z results. Most intermediate-z TF studies have adopted the radio TF calibration of Pierce & Tully (1992) as a low-z benchmark, but one would prefer a low-z reference sample with optical rotation curves (like the higher z samples) and a directly comparable method of distance determination,[1] to avoid systematic offsets arising from different analysis techniques. The low-z data should also provide a statistically fair representation of the full range of field galaxy morphologies, colors, and emission-line equivalent widths, permitting one to simulate the selection criteria of intermediate-z studies and investigate how these criteria influence the TFR.

The recently completed Nearby Field Galaxy Survey offers exactly these features, along with B-band photometry suitable for comparison with intermediate-z analyses (Jansen et al., 2000a,b; Kannappan et al., 2001c). In §5.2 we use the NFGS to recalibrate two existing intermediate-z studies (Vogt et al., 1997; Simard & Pritchet, 1998), attempting to match analysis techniques, selection criteria, and data quality. The Vogt et al. and Simard & Pritchet studies represent the two extremes of the luminosity evolution debate, and both employ spatially resolved rotation curves, facilitating direct comparison with the NFGS. In §5.3 we present a reference TF calibration for use in future studies of evolution in the TFR, based on a morphology-blind sample of NFGS emission-line galaxies brighter than $M_B^i = -18$. We also provide calibrations of the dependence of TF residuals on effective $B-R$ color and global EW(Hα).

5.2 Recalibrating the Intermediate-Redshift TFR

Table 1 summarizes our recalibration of the evidence for luminosity evolution in the samples of Vogt et al. (1997, hereafter V97) and Simard & Pritchet (1998, hereafter S&P). Both samples were originally calibrated against Pierce & Tully (1992, hereafter PT92).

[1] Although Hubble-law distances suffer from high scatter at low-z, they offer the simplest choice if the goal is consistency. The Cepheid-calibrated TFR of Pierce & Tully (1992) has been compared with intermediate-z data assuming $H_0 = 75$, but the Cepheid calibration implies a higher H_0 ($\sim$85). In principle, this error could be avoided by adjusting the assumed H_0. However, uncertainties remain, because the zero point of a Cepheid-calibrated TFR depends primarily on the properties of the Cepheid-hosting galaxies, and these galaxies constitute neither a complete nor a statistically large sample.

Table 1. Recalibration of Offsets in the Intermediate-z TFR

	Vogt et al.[a]	Simard & Pritchet
redshift range	$0.15 < z < 0.99$	$0.26 < z < 0.43$
average redshift $<z>$	0.52	0.34
# of galaxies in sample/NFGS reference sample	11/27	12/18
offset from PT92 in author cosmology [b]	-0.07	-1.83
offset from PT92 in Λ-cosmology [b]	-0.21	-2.03
offset from NFGS in Λ-cosmology [b]	0.01	-1.24
calibration difference	0.22	0.79
explained by (see text):		
sample selection[c]	-0.22	0.20
systematic zero point offset TP92−NFGS	0.44[d]	0.44[d]
lack of inclination correction	N/A	0.30
lack of extinction correction	N/A	-0.41
P.A. misalignment	N/A	0.26
additional correction:		
rotation curve truncation	N/A	0.71
final offset	0.01	-0.53

[a]N. Vogt has kindly provided updated magnitudes for this sample, which differ from those in Vogt et al. (1996, 1997) due to improved k corrections and revised extinction corrections that more closely match those of Pierce & Tully (1992, PT92). Vogt et al. (1996, 1997) used the equations in Tully & Fouque (1985) to correct luminosities for all internal extinction, whereas PT92 used the same equations to correct luminosities for only the excess internal extinction beyond what would be observed at face-on inclination.

[b]Λ-cosmology: $H_0 = 75$, $\Omega_{\rm M} = 0.3$, $\Omega_\Lambda = 0.7$; Vogt et al.: $H_0 = 75$, $\Omega_{\rm M} = 0.1$, $\Omega_\Lambda = 0$; Simard & Pritchet: $H_0 = 75$, $\Omega_{\rm M} = 1$, $\Omega_\Lambda = 0$. NFGS data are corrected for Virgocentric infall as in KFF; typical corrections for the subsamples considered here are $\sim$0.1 mag.

[c]The sample selection offset is computed relative to an NFGS reference sample with the same luminosity, inclination, and PA restrictions as the customized reference sample but with no restriction on morphology or peculiarity (for V97) or on EW([OII]) (for S&P).

[d]The systematic zero point offset in each column is simply the remainder of the calibration difference after known differences are subtracted. About 0.3 mag of the total 0.44 mag discrepancy between the NFGS and PT92 probably arises from a systematic offset in the Cepheid calibration of PT92 (Tully & Pierce (2000) report an 0.3 mag discrepancy between the calibrators used in early studies and those added later, which they attribute to a statistical fluke); this offset implies that the Hubble constant appropriate for comparison with PT92 is $\sim$85. The small remaining offset probably reflects the mismatch between radio linewidths and optical rotation velocities, in this case specifically V_{pmm}. Barton et al. (2000a) have also reported discrepancies between calibrations in the style of PT92 and calibrations based on samples analogous to the NFGS (e.g. their own data or that of Courteau, 1997).

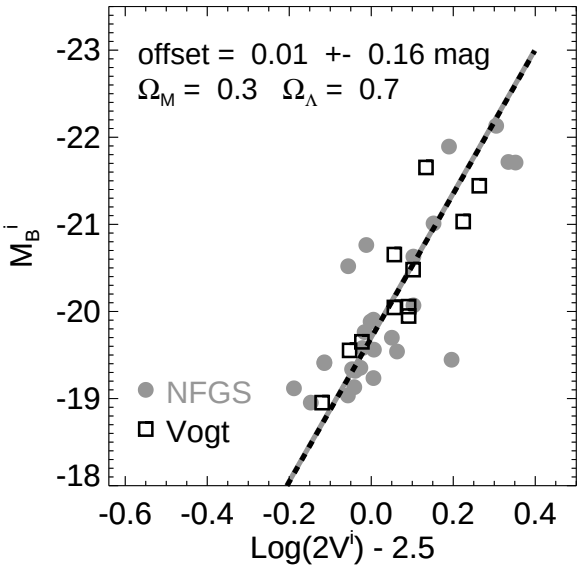

Figure 5.1.— Direct comparison of the intermediate-z sample of Vogt et al. (1997) and an NFGS subsample selected according to these authors' criteria. Intermediate-z data (open squares) were provided courtesy of N. Vogt, private communication, and include revised extinction and k-corrections. We use only the "high-quality" sample from V97 and restrict our own sample by analogy. The gray line shows an inverse fit to the NFGS data (i.e. minimizing residuals in $\log 2V^i_{pmm}$), while the black dotted line shows a fit to the V97 data with slope fixed to the NFGS value.

5.2.1 The Vogt et al. Sample

Figure 5.1 directly compares V97's 11-galaxy "high quality" sample (with revised magnitudes courtesy of N. Vogt, private communication) with a 27-galaxy low-z reference sample defined by similar criteria. V97 select "undisturbed spirals," which we interpret to mean all Sa–Sd spirals without strong bars or morphological peculiarities (warps, multiple nuclei, interacting companions, etc.; as identified in KFF). We exclude NFGS galaxies fainter than the faintest galaxy in the V97 sample ($\sim \mathrm{M}^i_\mathrm{B} = -19$). V97's "high quality" sample maintains slit P.A. misalignment ΔP.A. < 20 and inclination $i > 30$; we tighten the latter restriction to $i > 40$ for the NFGS (tightening the restriction eliminates one galaxy, a $>3\sigma$ outlier from the low-z TFR). Following V97, we calculate inclinations using $\cos i = b/a$ (N. Vogt, private communication) and adopt the extinction corrections of Tully & Fouque (1985). Both data sets are converted to the currently popular Λ-cosmology ($H_0 = 75$, $\Omega_\mathrm{M} = 0.3$, $\Omega_\Lambda = 0.7$).

V97 determine rotation velocities by fitting their observed data to emission lines simulated from a grid of exponential disk models with different terminal velocities,

convolved with model seeing and masked with a model slit. Rather than directly reproduce their methods, we explore the range of plausible rotation velocities consistent with the NFGS data using three different circular-velocity estimation techniques: the "probable min-max" velocity V_{pmm} (adapted from Raychaudhury et al., 1997, see KFF for details), the maximum velocity V_{max}, and the velocity determined from a fitted analytic rotation curve model V_{fit} (see KFF). Figure 5.1 and Table 1 show results using V_{pmm}; this parameter makes no *a priori* assumptions about rotation curve shape and produces the best match with HI linewidths for the NFGS. Fixing the intermediate-z slope to the value fitted to the low-z data, we measure V97-minus-NFGS luminosity offsets of $+0.01 \pm 0.16$, -0.21 ± 0.15 mag, and $+0.16 \pm 0.16$ mag using V_{pmm}, V_{max}, and V_{fit} respectively. Clearly the systematic uncertainties associated with mismatched rotation curve analysis techniques are at least as large as the formal statistical errors. Nonetheless, all techniques are consistent with a null offset.[2]

These results broadly confirm the conclusions of V97 using a more appropriate reference sample than PT92. Vogt et al.'s calibration against PT92 yields -0.21 mag of luminosity evolution in our standard Λ-cosmology (Table 1). While not large, the offset between the two calibrations underscores the importance of standardizing sample selection and analysis techniques. The 0.22 mag difference between Vogt et al.'s calibration and our recalibration (computing NFGS rotation velocities with the preferred V_{pmm} parameter) arises from a combination of partially canceling offsets due to both sample selection (the exclusion of barred, interacting, and non-spiral galaxies) and also a systematic zero point shift between PT92 and the NFGS.

5.2.2 The Simard & Pritchet Sample

Whereas Vogt et al. select galaxies primarily by morphology, Simard & Pritchet (1998, hereafter S&P) select bright galaxies with strong [OII] 3727 emission (EW([OII]) < -20) to make it easier to obtain kinematic measurements. For comparison with their 12-galaxy "kinematically normal" sample, we define a sample of 18 NFGS galaxies with EW([OII]) < -20, luminosity no fainter than the faintest S&P galaxy ($\sim M_B = -18.5$), and $i > 40$ ($b/a < 0.78$). Note that S&P do not measure or correct for galaxy inclination angles; our $i > 40$ cut is an attempt to quantify S&P's selection preference for galaxies with some sign of elongation. With the $i > 40$ cut, the NFGS subsample

[2]The V97 galaxies were selected for morphology, not color. However, the resulting sample is $\sim$0.2–0.3 mag bluer in $B-R$ color (using $(B-R) = 0.3 + 1.4(B-V)$) than the 27-galaxy NFGS comparison sample, implying a "reverse" luminosity offset in the R-band TFR. Such a reverse offset could indicate evolving stellar mass fraction (e.g. Buchalter et al., 2001b), but the color offset is too small to rule out systematic errors from band-shifting and k-corrections.

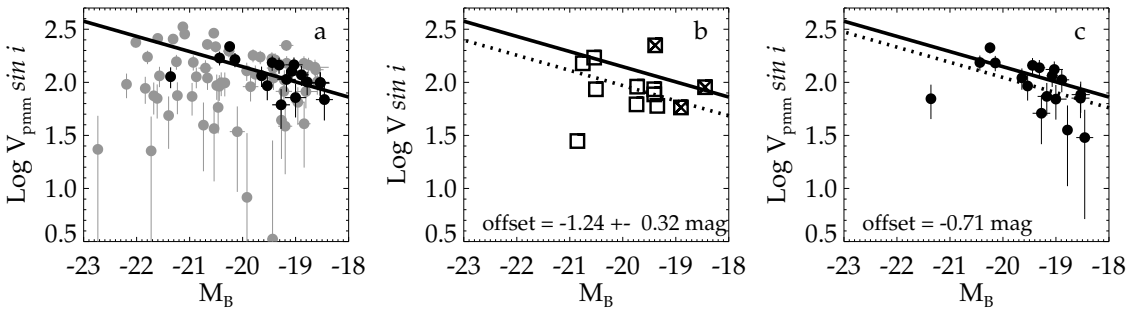

Figure 5.2.— Comparison of "kinematically normal" galaxy data from Simard & Pritchet (1998) and data for an equivalent NFGS subsample. Following S&P, we plot the TFR without inclination or extinction corrections. (a) : The NFGS subsample. Black/gray points represent NFGS galaxies included/rejected by analogy with S&P, within roughly the same luminosity range as their sample. The solid line shows the best fit to the black points with slope fixed to -7. This line is repeated in each panel. (b) : The Simard & Pritchet sample. X's mark galaxies corrected for severe P.A. misalignment. The dotted line shows the best fit with slope fixed to -7. (c) : The same NFGS galaxies as in the left panel, but with the data degraded to simulate the radial truncation of the S&P data. The dotted line shows the best fit with slope fixed to -7.

has average inclination $<i> = 68$.

Figures 5.2a and 5.2b show TF data for the NFGS and S&P samples, with magnitudes converted to $H_0 = 75$, $\Omega_{\rm M} = 0.3$, $\Omega_\Lambda = 0.7$. Following S&P, we plot the data without inclination or extinction corrections. Gray points in Figure 5.2a represent NFGS galaxies rejected from the comparison sample within the allowed luminosity range. X's in Figure 5.2b mark three S&P galaxies with severe slit P.A. misalignments; $V \sin i$ values for these galaxies have been boosted by 25 km s^{-1} to compensate.[3]

We determine the zero point of the TFR for both samples with the slope fixed to -7 in the $\rm M_B$, $\log(V \sin i)$ coordinate system (approximately the value S&P use, as measured from their Figure 4). Like V97, S&P model their rotation curves using exponential disk simulations convolved with seeing and instrumental blurring; for comparison, we use the three velocity parameters V_{pmm}, V_{fit}, and V_{max} (§5.2.1).

[3]The final S&P sample omits galaxies with ΔP.A. $\geq 45°$ but still contains three galaxies with severe misalignments of ~ 35–$40°$. To avoid discarding data from an already small sample, we retain these galaxies and attempt to compensate for their misalignments. S&P comment that misalignment probably reduces $V \sin i$ by about 25 km s^{-1} for one of the galaxies, based on a numerical simulation. In the absence of further information, we add this number to all three galaxies' $V \sin i$ values. All 18 galaxies in the NFGS comparison sample have ΔP.A. $< 5°$.

Respectively, these three parameters yield S&P-minus-NFGS luminosity offsets of -1.24 ± 0.32, -1.12 ± 0.32, and -1.54 ± 0.31; we show results using V_{pmm} in Figure 5.2.

S&P measure an average offset of -2.03 mag relative to PT92 (converted to our standard Λ-cosmology). Our measured offset differs from this value for several reasons, summarized in Table 1. First, our sample includes S&P's EW([OII]) restriction, which shifts the reference calibration toward higher luminosity by 0.20 mag. Unlike the PT92 calibration, the NFGS calibration omits inclination and extinction corrections to match S&P's analysis; these omissions shift the reference calibration toward higher and lower luminosity respectively, by 0.30 mag and -0.41 mag. Our P.A. misalignment correction on the S&P data reduces the apparent luminosity offset by 0.26 mag. Finally, we again see the systematic zero point shift between TP92 and the NFGS discussed in §5.2.1.

However, we have not yet addressed data quality. Figure 5.2c shows the effect of degrading the NFGS rotation curves to the average S/N level of the kinematically normal S&P data (8.16, using S&P's integrated S/N measurements computed within $\pm 3r_d$). To achieve roughly the same S/N, we add all the line signal from our Hα rotation curves within $\pm 3r_d$, then artificially increase the per-pixel rms noise σ_{pix} within a box bounded by $\pm 3r_d$ and the minimum and maximum measured velocities. Choosing σ_{pix} to give an overall S/N of 8.16 for the box, we next reevaluate the S/N of the individual points in the rotation curve, for each point summing the signal and the noise in the spectral line within the range of pixels where the signal exceeds the noise.

Finally, we truncate the rotation curve at the largest radius on each side with S/N equal to a fixed detection limit (Figure 5.3). As different rotation curve analysis algorithms differ in their detection efficiency, we vary this detection limit through a range of values: $\mathrm{S/N_{limit}} = 1.0,\ 1.5,\ 2.0,\ 2.5$. Applying these detection limits, we measure false luminosity offsets in the NFGS reference sample of -0.43, -0.67, -0.71, and -1.51 mag respectively (the $\mathrm{S/N_{limit}} = 2$ simulation result is shown in Figure 5.2c). As the 1.0σ limit seems optimistic, and the 2.5σ limit produces outliers more extreme than those seen in the S&P sample, we conclude that an offset of $\sim$0.7 mag is likely.[4] Figure 5.2c shows that this level of truncation may also contribute to

[4]Simard & Pritchet (1999) perform simulations in which they apply their rotation curve analysis techniques to model data of varying S/N, and they conclude that their techniques can recover a galaxy's full rotation velocity at the S/N levels of the real data in S&P. However, Simard & Pritchet (1999) do not test their techniques on degraded real data, and they assume that a galaxy's radial emission-line intensity profile can be modeled with the same exponential disk law that describes the continuum emission from the disk. For a given integrated S/N, adding a central intensity

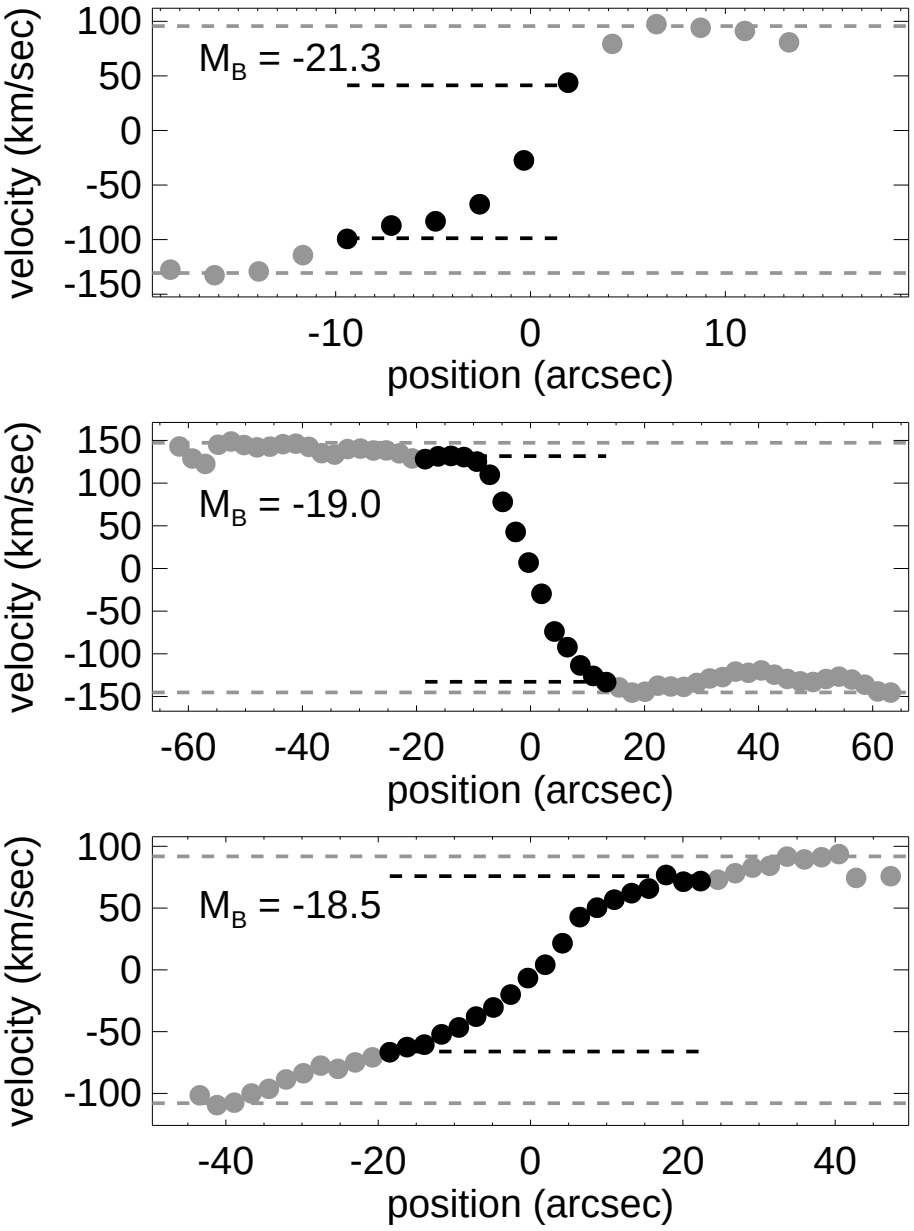

Figure 5.3.— Simulated radial truncation of NFGS rotation curves induced by artificially degrading the S/N. Gray dots indicate the full extent of the original NFGS rotation curves, while black dots indicate those points that retain local S/N>2 when the integrated S/N is degraded to a value of 8.16 (the average integrated S/N of the rotation curves in S&P). Dashed lines indicate the velocity width $2V_{pmm}$ with and without truncation, uncorrected for inclination.

S&P's observation of slightly higher offsets at the faint end of the TFR. The $\sim$0.7 mag offset corresponds to radial truncation at $\sim$1.7–1.8r_d, while a pure exponential disk first reaches peak velocity at 2.2r_d (Freeman, 1970). For comparison, V97's rotation curves have average radial extent $\sim$3.0r_d and all reach at least 2.2r_d (N. Vogt, private communication).

If we subtract $\sim$0.7 mag from our measured luminosity offset of -1.24 mag, we are left with an offset of only ~ -0.5 mag. Furthermore, two effects we cannot easily quantify may act to reduce the offset even more. First, the cloud of gray points in Figure 5.2a shows that any lapse in maintaining high inclination angles may produce substantial false luminosity evolution. Given S&P's low-resolution images and selection of actively star-forming galaxies, some of the elongation they observe may be caused by tidal tails or close companions rather than truly edge-on inclinations. Second, we have modeled rotation curve truncation using the customized NFGS reference sample, which may not reproduce the properties of the S&P sample despite similar selection criteria. If the S&P sample contains galaxies with more radially concentrated emission-line intensity profiles than are found in the NFGS, then additional truncation may occur (cf. Barton et al., 2000a). S&P partially address this issue by rejecting four anomalous galaxies with [OII] disk scale lengths $\sim$10–30 times smaller than their broadband scale lengths.[5][6] Such galaxies would be likely to give artificially low $V \sin i$ measurements, both because of rotation curve truncation and because of non-equilibrium gas motions associated with active nuclei (see the discussion of emission-line S0 galaxies in KFF). We conclude that the real luminosity offset in the S&P sample is probably $\lesssim$0.5 mag.

5.3 A Low-Redshift Reference Calibration

Here we provide a general-purpose low-z reference calibration for use by future studies of evolution in the TFR. Such a calibration cannot include sample-specific details such as the effects of low S/N, but it can match the general properties of higher z

enhancement to their model data would decrease the S/N in the outer parts of the model rotation curves.

[5]S&P also label three other galaxies as anomalous, but these appear to have been rejected for their P.A. misalignments rather than for centrally concentrated [OII] emission.

[6]With the caveat that our kinematics derive from Hα rather than [OII], we find no evidence for such centrally concentrated emission within the 18-galaxy NFGS comparison sample. S&P's four anomalous galaxies tend toward higher luminosity than the rest of their sample. Comparably bright galaxies with EW([OII]) < -20 are rare in the NFGS, which fairly represents the general galaxy population (see KFF). The high fraction of anomalous galaxies in the S&P sample may be an artifact of their target ranking system, which prioritizes the brightest galaxies with the highest EW([OII]).

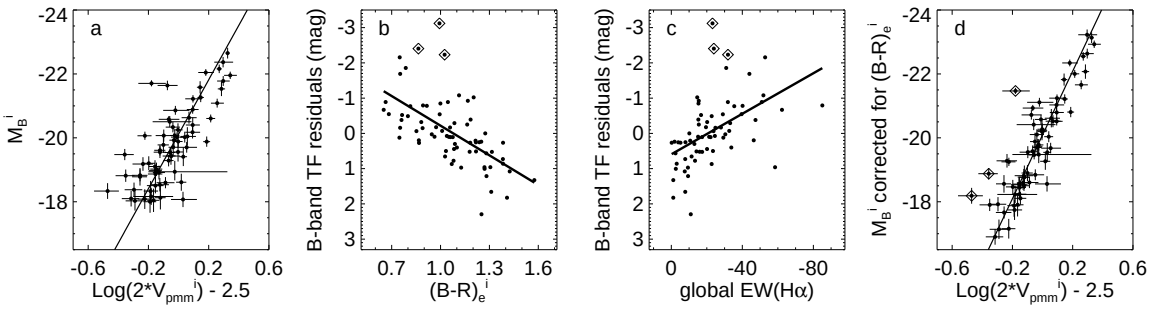

Figure 5.4.— *a*) The TFR for a morphology-blind sample of emission-line galaxies brighter than $M_B^i = -18$. An unweighted inverse fit (minimizing velocity residuals) yields $M_B^i = -20.11 - 8.52(2V_{pmm}^i - 2.5)$. *b*) The correlation between TF residuals (relative to the fit in panel *a*) and effective $B-R$ color, i.e. color within the B-band half-light radius. An unweighted forward fit (minimizing residuals in the residuals) yields $\Delta M_B^i = -3.0 + 2.8(B-R)_e^i$. *c*) The correlation between TF residuals and global EW(Hα). An unweighted forward fit yields $\Delta M_B^i = 0.59 + 0.029$EW(H$\alpha$). Global EW([OII]) generates a noisier correlation, $\Delta M_B^i = 0.55 + 0.031$EW([OII]). *d*) The color-corrected TFR, with magnitudes from panel *a* adjusted according to the fit in panel *b*. An unweighted inverse fit yields $M_{B,corr}^i = -20.09 - 9.97(2V_{pmm}^i - 2.5)$. Diamonds indicate outlier galaxies suspected of having large systematic inclination errors.

TF samples, which are nearly always field galaxy samples with optical emission-line rotation curves and Hubble-law distances.

Figure 5.4a shows the B-band TFR for a morphology-blind sample of 70 nearby galaxies. The sample includes all NFGS emission-line galaxies brighter than $M_B^i = -18$ and inclined by more than 40 degrees. As the NFGS provides a statistically representative sample of galaxies in the local universe, the subsample shown here provides a statistically representative sample of bright emission-line galaxies with $i > 40$. Full details of our parameter definitions, inclination and extinction corrections, error analysis, and fitting techniques are given in KFF. Distances are derived from a linear Hubble flow model with $H_0 = 75$, corrected for Virgocentric infall. The superscript i indicates corrections for inclination and internal extinction following the methods of Tully & Pierce (2000). For the extinction corrections, we convert the optical velocities to an equivalent radio linewidth scale as discussed in KFF.

Figures 5.4b & 5.4c display "third parameter" correlations between the residuals from the TFR in Figure 5.4a and both effective $(B-R)$ color and global EW(Hα); the caption also provides a fit to the much noisier TF residual–EW([OII]) correlation.[7] We

[7]Total colors and central-aperture equivalent widths do not predict TF residuals as well as ef-

discuss the physical drivers behind these correlations in KFF; here we present them simply as useful tools for evaluating the effect of selection biases on TF zero point (but one should bear in mind that the slopes or zero points of the correlations may themselves evolve with redshift). The color–TF residual correlation may also help to flag outlier galaxies that show apparent luminosity offsets for reasons unrelated to luminosity evolution, e.g. systematic errors or nuclear activity (Figure 5.4d).

5.4 Discussion

The recalibrations and analysis presented here largely reconcile the results of V97 and S&P. Sample selection effects influence both samples, but we find much larger systematic offsets in the S&P sample, arising from both sample selection and data analysis issues. Our analysis leaves room for a small discrepancy between the two studies ($\lesssim$0.5 mag), which if present may reflect differential evolution for different galaxy types: S&P selected for actively star-forming galaxies, while V97 selected for undisturbed spirals.

Clearly, if we hope to understand the overall luminosity evolution of the general galaxy population, then neither of these samples tells the whole story. Furthermore, our measurements of luminosity evolution are fundamentally flawed, in that we have compared low-z galaxies with intermediate-z galaxies that have similar properties, rather than comparing low-z galaxies with intermediate-z galaxies that *will evolve to have* similar properties (i.e. our analysis suffers from "progenitor bias," in the language of van Dokkum & Franx, 1996).

Without a full theory of galaxy evolution, the best way to address progenitor bias is to observe a broadly representative statistical sample. A survey equivalent to the full NFGS at higher redshift would allow us to evaluate the changing demographics of Tully-Fisher galaxies as well as their luminosity offsets. Future studies may also observe evolution in the slope or zero point of the color–TF residual correlation, another measure of global star formation history (see KFF). The reference calibrations presented here await such a study.

We thank Rolf Jansen and Nicole Vogt for providing data in electronic form, and Saurabh Jha, Warren Brown, and Betsy Barton for helpful discussions.

fective colors and global equivalent widths. Total colors behave much like effective colors but are subject to greater measurement uncertainty (see KFF).

Appendix A

Building a CCD Spectrograph for Educational or Amateur Astronomy†

†Kannappan, S. K., Fabricant, D. G., & Hughes, C. B.

ABSTRACT

We describe practical considerations involved in designing and building an affordable, high-quality CCD spectrograph for a small telescope. The requirements of low cost, simple design, high throughput, and minimal weight carried by the telescope can be met in an instrument similar to IntroSpec, the fiber-fed CCD spectrograph we recently built for educational use on the 16-inch Knowles Telescope at Harvard College.

A.1 Introduction

The widespread availability of affordable, high-quality commercial CCD cameras for astronomy now makes it possible for educators and amateur astronomers to conduct sophisticated observing programs with small telescopes and small budgets. In recent years the potential for building inexpensive CCD spectrographs around these cameras has been recognized by several companies and individuals (e.g. Glumac & Sivo, 1999). Observations of the spectra of stars, planets, and nebulae open up an exciting new realm of inquiry for beginning astronomers, and the design and construction of the spectrograph itself can provide students with a hands-on education in the principles of optics and engineering. In this article we describe the practical aspects of such a project, based on our experience with IntroSpec, the instructional spectrograph we recently built for the Harvard Astronomy Department.

IntroSpec had four design goals: sufficient spectral range and resolution for a range of projects in optical astronomy, high throughput to enable observations of nearby nebulae and variable stars, ease-of-use for students, and an acceptably low weight load on the telescope's drive. Low weight and high throughput would be important for any spectrograph built for a small telescope, because of the limits on light gathering power and weight bearing capacity. Our spectral range and resolution goals would also apply for most such projects: we aimed for $\sim$6 Å resolution with a spectral range of $\sim$4500–6800Å, which includes many of the key spectroscopic lines of optical astronomy (stellar metal absorption lines from Fe and Mg; planetary molecular absorption bands from CH_4 and NH_3; and nebular emission lines such as Hα and Hβ). While not sufficient for kinematic analyses, 6 Å resolution permits the separation of such features as the emission lines of Hα and [NII].

We were able to meet these goals on a budget of slightly under $5500, of which $\sim$$4000 went into buying a mid-range Meade CCD camera and paying for a skilled

machinist's time and materials (CBH).[1] Below we describe how IntroSpec's design was tailored to the specific challenges posed by our budget and performance requirements. §A.2 reviews the general optical design constraints on any similar spectrograph, while §A.3 examines the specific choices we made for IntroSpec, with special attention to the instrument's fiber-fed design.

A.2 Optimizing the Optical Design

We begin with a brief review of the layout of a generic spectrograph, then consider how to optimize its optical design.

A.2.1 Layout of a Generic Spectrograph

Figure A.1 shows the light path in a simple CCD spectrograph. The aperture accepts a small circle of light from the telescope focal plane – containing for example the image of a star or a portion of a nebula. This light then travels to the collimating lens of the spectrograph, which converts the light to a parallel beam. The parallel beam strikes the diffraction grating and is dispersed into a spectrum according to the grating equation (e.g. Schroeder, 2000):

$$m\lambda = d(\sin\theta_1 + \sin\theta_2), \tag{A.1}$$

where m is the order of the diffraction peak, λ is the wavelength of the light, d is the spacing between lines on the grating, and θ_1 and θ_2 are the incoming and outgoing angles of the light with respect to the normal to the grating surface (see Schroeder for sign conventions). Upon hitting the grating, the overall direction of the beam also changes, typically folding back at $\sim 45^\circ$ in the case of a blazed[2] reflection

[1] These numbers do not include an expensive but desirable accessory: a Hg-Ne lamp for wavelength calibration. We purchased one from Oriel for an additional $450.

[2] A problem with ordinary diffraction gratings is that much of the light is squandered on the central maximum and the higher orders, where it will never reach a detector. This problem is partially solved in a blazed grating, in which the mirror surface of the grating is arranged in a sawtooth structure so that the reflecting surface is inclined to the grating surface by an angle known as the blaze angle. The blaze angle is chosen such that simple geometrical reflection sends the light not toward the central maximum, but instead toward the first order maximum. For a transmission grating, a similar effect may be achieved by choosing the index of refraction of the material to refract the primary beam at the angle of the first order diffraction peak. In practice, a small amount of light will still go into the other orders, however the light-gathering efficiency in first order is dramatically improved.

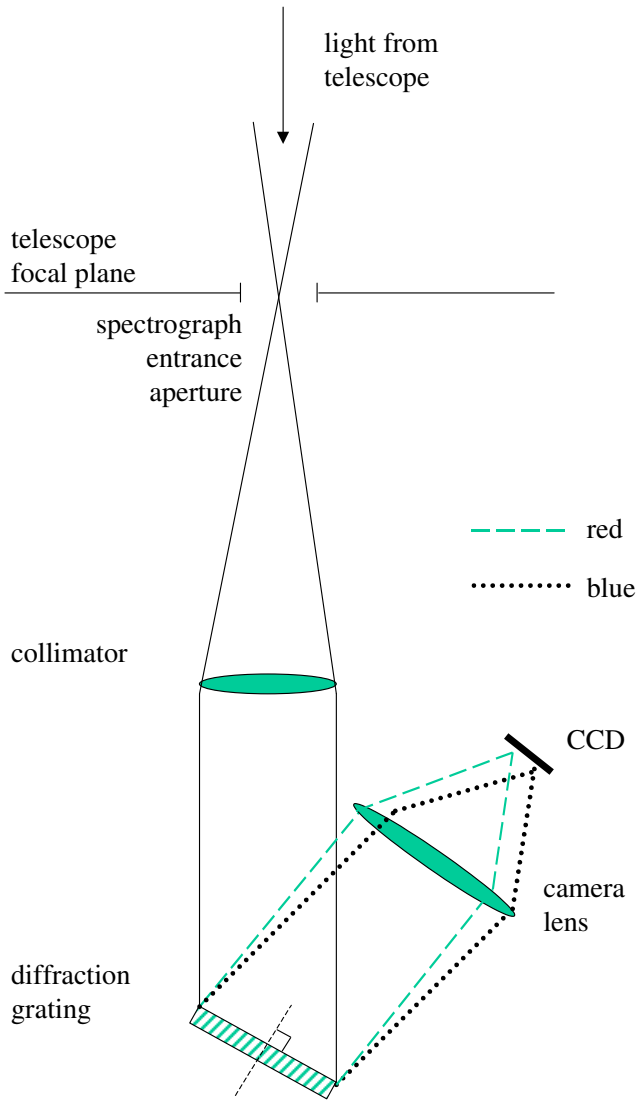

Figure A.1.— Schematic of the optics in a simple spectrograph with a reflection grating. Note that the normal to the diffraction grating (thin dashed line) does not bisect the angle between the camera and the collimator; as a result, the beam is wider leaving the grating than it was arriving (a.k.a. anamorphic magnification).

grating, as shown.[3] The dispersed beam is a superposition of collimated beams of different colors, each traveling at a slightly different angle. The camera lens focuses each color onto a location on the CCD chip determined by its incoming angle, thereby forming a spectrum. This focusing process is exactly analogous to the way a telescope focuses incoming parallel light beams from stars at different angles on the sky onto different positions on the telescope focal plane: in the spectrograph, each point along the spectrum is an image of the light from the spectrograph entrance aperture at a different wavelength. A higher dispersion grating spreads these different-wavelength images further apart, giving higher spectral resolution at the expense of reduced spectral range over the entire CCD.

A.2.2 Sampling and the Relative Scaling of the System

Regardless of the choice of grating or absolute scale of the system, the optimal optical design for this basic spectrograph occurs when the different-wavelength images of the spectrograph entrance aperture — the spectroscopic resolution elements — are neither undersampled nor oversampled on the CCD chip. Oversampling wastes CCD pixels without gaining information, as the Nyquist sampling rule specifies that only $\sim$2 pixels per resolution element are required to recover full information. Technically, the Nyquist sampling rule applies to sinusoidal signals; for point source images up to 3-4 pixels per resolution element can provide additional information, and professional instruments with large CCD chips may opt for better sampling. However, higher sampling reduces the total spectral range that can fit on the CCD chip, and a goal of slightly over 2 pixels per resolution element is sufficient for a non-professional instrument. Sampling with less than 2 pixels per resolution element effectively degrades the spectroscopic resolution to whatever value corresponds to $\sim$2 pixels on the CCD, regardless of any higher resolution designed into the optics. The only way to increase spectral range at a given optimally sampled resolution is to increase the CCD chip size: IntroSpec's design target of 6 Å resolution combined with spectral coverage of 2300 Å implies a CCD chip with approximately $2 \times 2300/6 = 767$ pixels (not accidentally, since the best CCD we could afford had 768 pixels in the long dimension).

Requiring optimal sampling sets the relative scales of the system, because the focal lengths of the collimator and camera lenses, $f_{\rm coll}$ and $f_{\rm cam}$, must be chosen in a

[3] Transmission gratings or prisms may be useful alternatives when a more linear optical design is desired. However, transmission gratings generally have either lower resolution or lower efficiency than reflection gratings, because only low-dispersion transmission gratings can be blazed. Prisms have even lower spectral resolution and their spectral dispersion varies strongly with λ.

ratio that will reduce the image of the spectrograph entrance aperture down to ∼2 CCD pixels, or ∼20 μm for a typical amateur CCD camera. The (unreduced) size of the spectrograph entrance aperture is set by the local seeing and the telescope optics: typically the instrument design matches the size of the spectrograph entrance aperture to the size of the seeing disk on the telescope focal plane, in order to maximize stellar light and minimize background sky light. For the 16-inch $f/10$ Knowles Telescope at Harvard, the local five-arcsecond seeing disk makes a 100 μm point source image on the telescope focal plane, implying that $f_{\rm coll}/f_{\rm cam}$ must equal ∼5 to reduce the image to ∼20 μm. Similar seeing would make a 50 μm point source image on an 8-inch $f/10$ telescope, requiring an $f_{\rm coll}/f_{\rm cam}$ ratio of ∼2.5. A larger entrance aperture (implying higher $f_{\rm coll}/f_{\rm cam}$ to achieve the same resolution) might be desirable for an 8-inch telescope, because of the technical difficulty of achieving a 50 μm aperture. Larger apertures also give more leeway for poor guiding.

Once $f_{\rm coll}/f_{\rm cam}$ is set, the slowest acceptable f/ratios for the two lenses are also determined. To avoid vignetting, the collimator diameter must at least match the collimated beam size, which implies that the collimator f/ratio must be at least as fast as the incoming $f/10$ light cone from the telescope. If the collimated beam were to travel directly to the camera lens (without hitting the diffraction grating and reflecting/dispersing), then the $f/10$ focal ratio of the telescope would imply a camera focal ratio at least as fast as $f/2$, to satisfy $f_{\rm coll}/f_{\rm cam} = 5$. Taking into account the diffraction grating places a further demand for speed on the camera lens, both because the beam is dispersing and because the angle of reflection causes the beam to expand: following the reflection from the grating, the beam diameter increases by a geometric "anamorphic magnification" factor AM $= \cos(\theta_{cam-coll} - |\theta_1|)/\cos\theta_1$, where $\theta_{cam-coll}$ is the angle between the camera and the collimator (see Figure A.1 and §A.2.2.1).

A.2.2.1 Money, Spectroscopic Performance, and the Absolute Scaling of the System

The fact that our design goals have thus far been expressed as ratios ($f_{\rm coll}/f_{\rm cam} = 5$ and $f/\#_{\rm cam} < 2$) gives us some flexibility in choosing the overall dimensions of the optics. Two constraints determine the absolute scale of the system: money and spectroscopic performance. Financial considerations enter in two ways. First, as a general rule, when things get large, they get expensive. Large optical elements imply large mounts and long focal lengths, increasing the weight and cost in materials of the entire system, and the cost of diffraction gratings goes roughly as the square of their diameter. Second, we have just seen that optimizing the optical design for a system similar to IntroSpec leads to the demand for a very fast camera lens with minimal

aberrations over a wide field of view (the CCD chip). Such lenses are difficult to make and therefore in principle expensive. However, the economics of mass production for the consumer economy comes to our rescue here: an ordinary photographic camera lens offers superior image quality, anti-reflection coatings, and wide-field imaging, all optimized for 35-mm format film (actually 24 $\times$ 36 mm). CCD chips in typical amateur cameras fit easily within this format. Furthermore, a high-quality photographic lens will produce images smaller than $\sim$20–25 μm over a large portion of its focal surface, conveniently matching the size of a 2–3 pixel resolution element for a CCD camera with $\sim$10 μm pixels.

Assuming, then, that we will choose a commonly available photographic lens to optimize our optical design within the budget constraints of a small instrument, the problem becomes one of selecting the best lens based on our goals for spectroscopic performance. Table 1 lists a number of commonly available photographic lenses by $f/\#$ and focal length. Specifying the camera lens determines every other optical scale in the system given the relative scaling rules determined earlier. When combined with our spectral range and resolution goals (4500–6800 Å range and 6 Å resolution), the camera focal length also sets the grating dispersion in lines/mm.

To determine the best lens, we begin by calculating the grating dispersion appropriate to each camera focal length. With $\sim$5% accuracy, the ideal grating ruling is simply $\Delta\theta/\Delta\lambda$, where $\Delta\theta$ is the angle subtended by the CCD chip at the specified focal length and $\Delta\lambda$ is the total spectral range (2300 Å). This relation follows from trigonometry and the grating equation (Schroeder, 2000) if we make some reasonable assumptions: the grating is used in first order, its dispersion may be approximated by the value at the center of the CCD chip, the camera-collimator angle is 45°, and the grating normal bisects this angle. (We will return to the reasons for these choices of angle in a moment.) Although nonstandard grating rulings are available, standard rulings will generally be cheapest, so the next column after the ideal grating ruling in Table 1 lists the nearest match out of five commonly available rulings: 150, 300, 600, 900, or 1200 lines/mm. Given these rulings, we then recompute the actual range and resolution of the lens-grating combination, assuming Nyquist sampling on a 768-pixel CCD chip as used in IntroSpec.

By design, all of the lens-grating combinations meet our range and resolution specifications reasonably well. However, the next three columns of Table 1 indicate the trade-offs required in each case. One issue is simply the size of the lens: we have already argued that all other things being equal, smaller lenses (and smaller spectrographs) will usually cost less, as long as we stay within the realm of standard inventory. The other concern is anamorphic magnification, i.e. the geometric magnification of the collimated beam in the spectral direction caused by the tilt of the grating.

Table 1. Setting the Absolute Scale of the System

$f/\#_{\rm cam}$	$f_{\rm cam}$ (mm)	$\Delta\theta$ (°)[a]	ideal disp[b]	grating disp[c]	$\Delta\lambda$ (Å)[d]	$\delta\lambda$ (Å)[e]	$d_{\rm cam}$ (mm)	AM[f]	$d_{\rm cam}/d_{f/2}$[g]
1.4	28	14.05	1066	1200	2043	5.3	20.00	1.39	1.43
1.4	28	14.05	1066	900	2724	7.1	20.00	1.27	1.43
1.4	35	11.26	854	900	2183	5.7	25.00	1.27	1.43
1.2	50	7.89	599	600	2296	6.0	41.67	1.17	1.67
1.4	50	7.89	599	600	2296	6.0	35.71	1.17	1.43
1.4	85	4.65	353	300	2704	7.0	60.71	1.17	1.43
2.8	100	3.95	300	300	2299	6.0	35.71	1.08	0.71
2.8	200	1.98	150	150	2300	6.0	71.43	1.08	0.71

[a]Angular diameter of CCD chip at $f_{\rm cam}$. We assume a 6.9 mm CCD as found in IntroSpec's Meade Pictor 416XT.

[b]Ideal grating ruling in lines/mm for obtaining the preferred resolution $\Delta\Lambda_{spec}$ with the indicated $f_{\rm cam}$. This value may be calculated to within ∼5% as ideal disp = ($\Delta\theta$ (in radians) / $\Delta\Lambda_{spec}$ (in mm)). We assume the grating is used in first order.

[c]Commonly available grating ruling closest to the ideal ruling.

[d]Approximate spectral range with the indicated grating ruling, estimated as $\Delta\theta$ (in radians) / grating ruling (in lines/Å).

[e]Spectral resolution corresponding to the indicated spectral range, assuming Nyquist sampling and a 768 pixel CCD chip.

[f]Anamorphic magnification, i.e. the geometric magnification of the collimated beam in the spectral direction caused by the tilt of the grating. AM = $\cos(45° - |\theta_1|)/\cos\theta_1$ given a camera-collimator angle of 45°. We solve the grating equation for θ_1 assuming a central wavelength of 5650 Å.

[g]Ratio of the true lens diameter with the indicated $f/\#$ to the lens diameter required for $f/2$ operation (the slowest $f/\#$ allowed for optimal performance with our CCD and telescope, see §A.2.2). Ideally this number should exceed the anamorphic magnification to avoid vignetting.

When we assumed earlier that the grating normal bisected the camera-collimator angle, we effectively assumed no anamorphic magnification: in that configuration, the grating projects the same diameter viewed from either the collimator or the camera. In reality however, the grating normal nearly always points closer to the camera axis (Schroeder, 2000). As a result, the grating (and the emerging beam) appears larger along the dispersion axis as viewed from the camera, by the geometric factor $\cos(\theta_{cam-coll} - |\theta_1|)/\cos\theta_1$ discussed earlier. Anamorphic magnification creates problems because the camera lens must now accept light over a larger diameter in one direction, so our $f/2$ specification will no longer be fast enough to avoid vignetting.

Quantifying this effect requires solving the full grating equation for the angle between the grating normal and the camera axis, making the approximation that the

wavelength λ at the middle of the spectral range (in our case 5650 Å) falls on the middle of the CCD chip. We continue to assume a camera-collimator angle of 45° for simplicity, which should be within ∼10–15° of the final choice: angles smaller than ∼30° make it difficult to keep the camera lens from vignetting the light traveling between the collimator and the grating, while angles larger than ∼60° generally lead to unacceptably high values of anamorphic magnification. In the final design stage, one would iterate the solution to determine the optimal camera-collimator angle more precisely.

The last two columns list the anamorphic magnification factor for each camera-grating combination and the anamorphic magnification the camera lens can tolerate. Most of the lenses are faster than $f/2$, permitting an unvignetted system if we treat them as $f/2$ lenses (the slowest permitted by our optical design) with some extra aperture along the dispersion axis set by the ratio $f/\#_{\rm cam}$ / $f/2$. This ratio is listed in the last column of Table 1. In the end, four options emerge as superior: an $f/1.4$ or $f/1.2$ 50 mm lens used with a 600 lines/mm grating, or an $f/1.4$ 28 mm or $f/1.4$ 35 mm lens used with a 900 lines/mm grating. The 50 mm lenses offer the greatest comfort margin for vignetting, with the disadvantage of requiring a slightly larger overall system. The 50 mm focal length corresponds to the most common standard consumer lens, so these lenses are likely to be available cheaply. We chose an $f/1.4$ 50 mm Nikon lens for IntroSpec after finding a secondhand lens with some exterior cosmetic imperfections for $50.

A.3 IntroSpec

Here we summarize the specific optical and mechanical design choices we made with IntroSpec and how they were implemented. A list of purchased parts is provided in Table 2.

A.3.1 General Overview of the Instrument

IntroSpec closely follows the optical layout of the generic CCD spectrograph in Figure A.1, with one key difference. A technical problem arose because the optical design constraints outlined in §A.2 led us to prefer moderately large optical elements — a 50 mm focal length camera lens and a 250 mm focal length collimator (to satisfy $f_{\rm coll}/f_{\rm cam} = 5$). However, a 16" telescope will support neither the size nor the weight of such an instrument. Instead of sacrificing optical performance, we opted for a bench-mounted, fiber-fed design. Light from the sky enters a set of optical fibers at

Table 2. Purchased Parts List[a]

Spectrograph
Newport PAC088 cemented achromat, 2" diameter, $f = 250$ mm
Newport LH-200 2" diameter lens mount
Richardson Grating Lab 588 lines/mm reflection grating, $50 \times 50 \times 6$ mm blazed at 561 nm
Newport 481-A Rotation Stage (English Model, Standard Micrometers)
Nikon $f/1.4$ $f = 50$ mm photographic lens
Meade Pictor 416 XT CCD camera
Meade 12 V DC to 115 AC adapter
1.25" CCD barrel from Meade Customer Service
junk bayonet mount (free from photography shop)
Guider
2 Newport PAC040 precision achromatic doublets, 25.4 mm diam, EFL = 50.8 mm
Sirius Plossl eyepiece 1.25" diameter, $f = 26$ mm
Meade 2" diagonal mirror #929
Fiber Train
Polymicro FVP series multimode step-index fiber, core diam 100 & 300 μm
Fiberguide SFS200 240T multimode step-index fiber, core diam 200 μm
M M Newman 20 gauge PTFE standard wall Teflon tubing
Bally Ribbon Mills Pattern 8444 0.5" Tubular Nylon Webbing

[a]All other parts were made in the machine shop or the lab.

the telescope focal plane, and from there the fibers reroute the light to the side of the dome, where IntroSpec sits on a table. With the weight taken off the telescope, we were able to house IntroSpec in a heavy metal box with an easy-to-remove lid, which protects the instrument while keeping it accessible to students. The bench-mounted design also has the advantage of eliminating flexure in the spectrograph, leading to very stable wavelength calibration.

Figure A.2 provides an overview of IntroSpec. The optical fibers are coupled to the telescope via a guider/telescope attachment, further discussed in §A.3.3. The fiber train consists of six fibers, each of which accepts light from a different position on the telescope focal plane; these are bundled in several layers of protective coverings. (§A.3.2 discusses the technical aspects of working with fibers in more detail.) Upon entering the spectrograph enclosure, the fiber train loops around a large black spool for strain relief, then the fibers are channeled into the fiber output, from which the bare fiber ends emerge in a vertical stack (Figure A.3). The base of the fiber output assembly slides forward and backward next to a small ruler and locks down, permitting precise positioning of the fiber ends at the focal plane of the collimator lens. Each

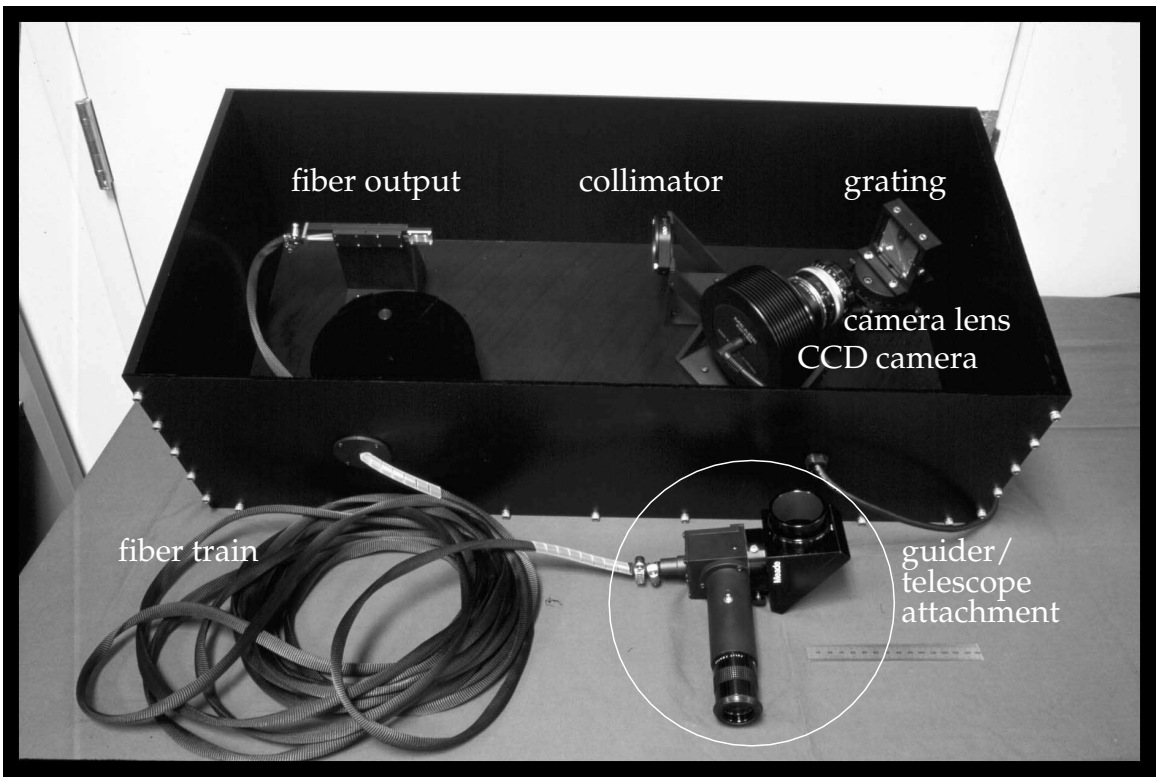

Figure A.2.— Overview of IntroSpec. See §A.3.1 and Table 2.

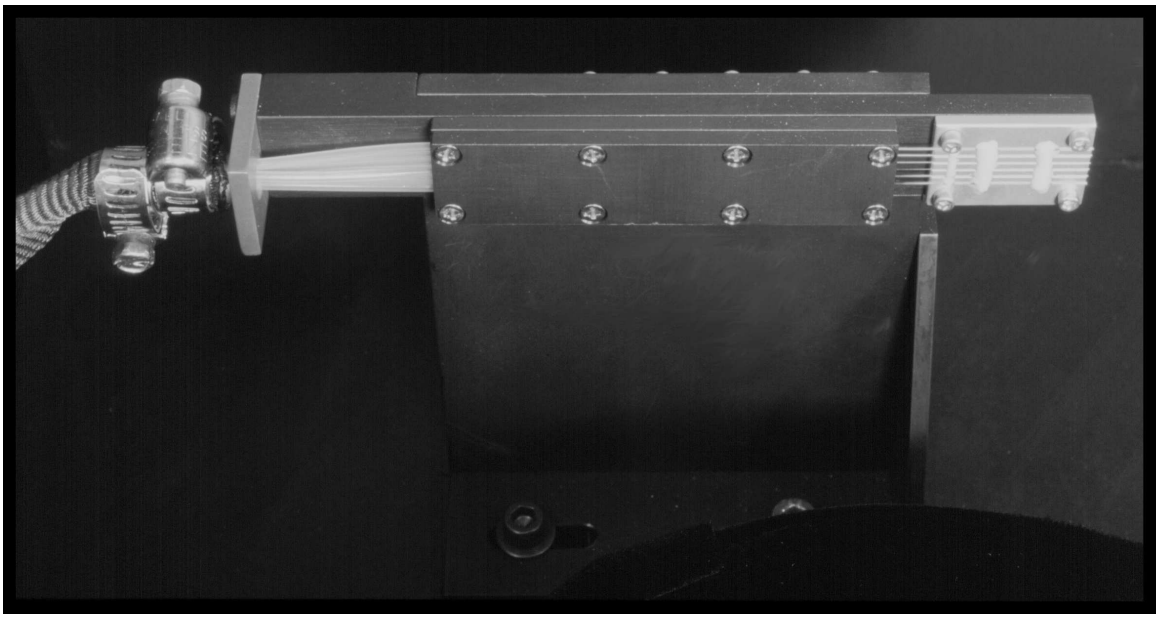

Figure A.3.— Fiber output assembly. Three pairs of fibers with diameters of 100, 200, and 300 μm are arranged vertically, with the smallest fibers at the center and the largest fibers at the top and bottom. The ends of the fibers are aligned precisely in six V-grooves; the V-grooves are not anodized to avoid compromising the alignment (see §A.3.2).

fiber end acts like a spectrograph entrance aperture; by stacking these apertures perpendicular to the dispersion axis, we obtain six parallel spectra on the CCD chip (Figure A.4).

IntroSpec's fibers come in three pairs of two, with diameters 100, 200, and 300 μm. The seeing disk at the Knowles telescope almost exactly matches the size of a 100 μm fiber, so this fiber diameter provides the highest spectral resolution at $\sim$6 Å. Larger fibers give the user the choice to degrade the spectral resolution for the sake of gathering more light from a faint extended source such as a nebula; larger fibers also provide more guiding leeway when high resolution is not important. The different fiber diameters allow students to explore the relationship between fiber size and spectral resolution as part of understanding the instrument. For point sources, we use one fiber in a pair to acquire the target spectrum and the second fiber in the pair to acquire the sky spectrum for background subtraction.

From the collimator on, IntroSpec looks much like the generic spectrograph of Figure A.1. For ease of mounting and good image quality, the collimator is an oversize 2-inch achromat with $f_{\rm coll} = 250$ mm, yielding a collimated beamsize of $\sim$1 inch with an incoming $f/10$ light cone. Rather than the standard 600 lines/mm grating blazed for peak efficiency at 5000 Å, we selected a 588 lines/mm grating blazed for peak efficiency at 5610 Å. Richardson Grating Laboratory offers this grating in sizes up to $\sim$50 mm square. The grating face is precisely aligned to the rotation axis of a Newport rotation stage, permitting micrometer adjustment of the grating angle to vary the spectral range. With a camera-collimator angle of 36°, IntroSpec's design range of 4500–6800Å corresponds to an 8° angle between the grating normal and the camera axis. At this rotation angle, the grating projects a diameter of 44 mm as viewed from the collimator and has an anamorphic magnification factor of 1.12, so the outgoing beam is oval in shape with dimensions $\sim 1 \times 1.12$ inches.

The dispersing colors in the beam spread slightly over the next $\sim$3.5 inches before reaching the camera lens, a 50 mm $f/1.4$ Nikon lens with full aperture $\sim$1.4 inches. Attaching the lens to the CCD camera required machining a special connector using a spare bayonet mount and an extra CCD camera mount from Meade. Our laboratory tests have shown that the Nikon lens produces point source images with full-width half-maximum diameters of $\sim$20–25 μm over most of the 6.9 mm CCD chip in our Meade Pictor 416 XT. The KAF-0400 chip in this camera offers 768×512 pixels, each 9 μm square. Readout data leaves the camera via the cord shown exiting the spectrograph enclosure to the front right in Figure A.2, which connects the CCD to the Meade Pictor control box (not shown). The cord also provides power to thermoelectrically cool the CCD.

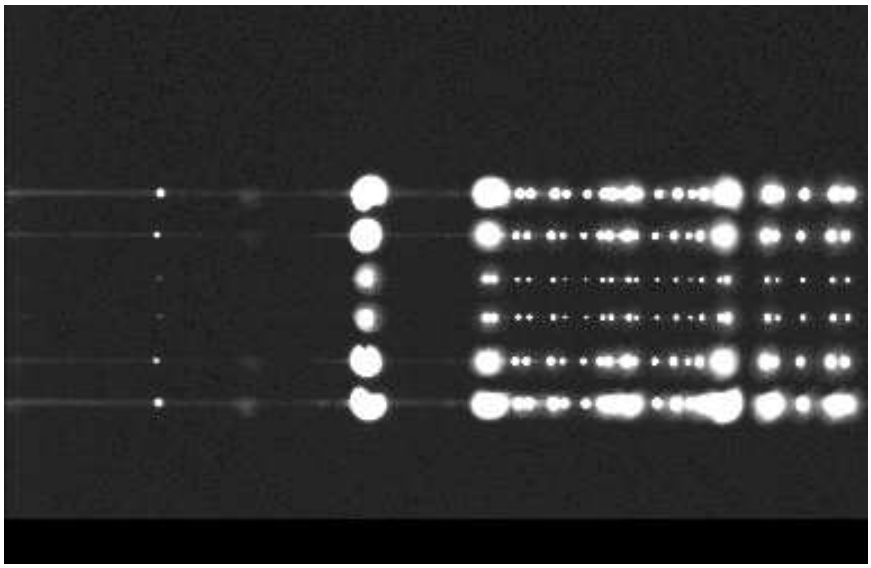

Figure A.4.— CCD image of six stacked spectra from Introspec's six optical fibers. The fibers have been illuminated with a mercury-neon calibration lamp, which creates narrow emission lines at specific wavelengths (there are relatively few bright lines between 4500–5500Å). Many of the lines are saturated and show CCD blooming effects; the fainter unsaturated lines show the true image quality. The image shown here was binned by two on readout.

A.3.2 Working With Fibers

In a fiber-fed spectrograph, each fiber acts like a flexible hole, allowing the light to enter the spectrograph almost as if directly from the telescope. If the fiber is not pinched or stressed, the light exits the fiber with approximately the same $f/\#$ with which it entered. However, small stresses can lead to focal ratio degradation (a faster exiting light cone). This degradation in turn leads to reduced system throughput, as the collimator fails to capture all of the rapidly diverging light. *For high-quality fibers in lengths of a few meters or less, the major light losses between 4000 and 9000 Å arise not from transmission losses, but from focal ratio degradation and reflection losses at the fiber ends.* Avoiding these losses requires both purchasing high-quality fibers and taking special care in handling them.

The many types and uses of optical fibers in astronomy have been discussed elsewhere (e.g. see Barden, 1988; Gray, 1993; Arribas et al., 1998). IntroSpec makes use of multimode, step-index fibers with a pure fused silica core and doped fused silica cladding, because such fibers provide the best transmission and best preservation of input focal ratio.[4] Several companies[5] offer high-quality silica core/silica cladding fibers with core diameters between 100 and 1000 μm (50 μm fibers are also available, but they are fragile and easily stressed). The silica cores come in high OH and low OH versions that transmit better in the blue and the red respectively; high OH fibers are most appropriate for an instrument like IntroSpec that will operate over a broad spectral range.

Distortion of the fiber caused by external stress is the most usual source of focal ratio degradation. To avoid mounting stresses, we align the ends of the fibers by laying them flat in precisely machined V-grooves, fixing them in place with 5-minute epoxy doped with fine silica powder to prevent contraction upon curing (Figure A.3). The V-grooves are machined using a 45° double-angle cutter as shown in Figure A.5. The cutter must have very sharp points because of the minimal depths required ($\sim$0.010"); cutters with large radii on the cutting teeth should be avoided. We have obtained good results with cutters from Dolfa. After the grooves are cut, we lightly bead blast them with medium (60-100) glass beads; this process slightly smoothes the groove but does an excellent job of removing burrs and also creates a good surface for bonding.

Stress along the length of the fiber can be minimized by enclosing each fiber in a

[4] The most common variety of silica core/silica cladding fibers accept a numerical aperture of 0.22, corresponding to a focal ratio of $\sim f/2.2$, so these fibers can accomodate virtually any telescope $f/\#$.

[5] We have had good experiences with Polymicro Technologies, CeramOptec Inc., and Fiberguide Industries.

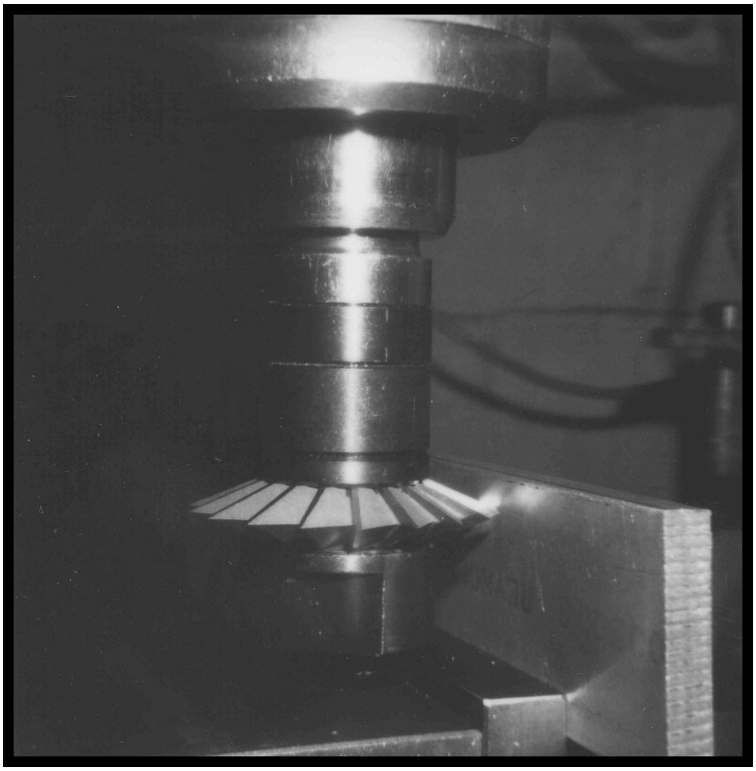

Figure A.5.— Machining V-grooves with a milling machine. We use a 45° double angle cutter in an R-8 or 3/4" straight shank stub milling machine arbor.

loosely fitting sleeve of teflon tubing;[6] for convenience and extra protection, we also bundle these tubes within a larger fabric sheath. Several stages of strain relief at both ends of the fiber train protect the fibers from accidental tugs and prevent sharp kinks from forming.

Accurate fiber alignment and polishing is also critical, both to avoid focal ratio degradation losses for the entering light cone and to avoid misdirection of the exiting light cone. Both the entrance and exit ends of the fibers must be polished flat to a good optical finish, and the polished ends must be perpendicular to the fiber axes (which are aligned perpendicular to the focal plane using the precisely machined V-grooves). We used a fiber polishing machine built for an earlier project; a similar machine could be constructed for ∼$300 in parts. The machine consists of a flat glass disk attached to an aluminum turntable rotating on a 72 rpm motor. A rigid arm holds a brass cylinder perpendicular to the glass disk. The brass cylinder has V-grooves cut along its length, and the fibers are temporarily attached to the V-grooves with Duco cement for polishing. A large drop of Duco cement covers the end of each fiber, which protrudes by ∼2 mm (most of this will be polished away). We attach disks of high quality self-adhesive abrasive paper in successively finer grades to the turntable, and the brass cylinder containing the fibers is swept across the abrasive paper. The sequence begins with 30 μm grit paper and ends with 0.3 μm grit paper. A thin solution of dish washing soap in water provides adequate lubrication; clean water is used to rinse off grit residue before moving to the next smaller grit (the motor is isolated from water spills). Finally, we inspect the fiber ends under a microscope to verify that no scratches remain. The entire process can be time-consuming and may require several iterations, but the results justify the investment of time.

A.3.3 The Manual Guider

Acquiring and tracking an astronomical target requires some mechanism for seeing the focal plane. Autoguiders are expensive and moreover lack the hands-on feel we wanted for IntroSpec. We therefore opted for a manual guider that allows the observer to continuously monitor and correct the telescope tracking while also viewing the sky surrounding the spectroscopic target within a 12 arcminute field of view.[7]

[6]The fibers are also supplied with a 5 to 10 micron thick plastic buffer to protect the them from scoring that would quickly result in breakage. This buffer need not be removed when mounting the fiber in the V-grooves.

[7]Glumac & Sivo (1999) suggest another alternative: an easily removed fiber attachment that can be swapped out for an eyepiece every time the observer searches for a new target. This unguided design requires that the telescope tracking be extremely accurate, or alternatively that the targets of interest be so bright or so extended that light losses caused by the target moving off the fiber

Figure A.6 illustrates the primary components within the guider. The optical design consist simply of a flat mirror that crosses the focal plane of the telescope at a 45° angle, with a split in the mirror to allow the fibers to poke through exactly where the mirror and focal plane intersect. All the light that does *not* go down the fibers is reflected by 90° and reimaged at the focal plane of a standard 26 mm Plossl eyepiece, using two matched relay lenses. The observer views everything in the telescope focal plane except whatever falls on the fibers; his or her job is to ensure that the target of interest "disappears" down one of the fibers.

The mechanical design of the guider was a little more complicated than the optical design, because the guider also serves as the interface between the telescope and the fibers. As such, it incorporates mechanisms for eyepiece rotation, strain relief, and fiber alignment. To minimize weight, nearly all of the parts were made from aluminum, including the mirror. We were able to get a satisfactory polish on the mirror by first removing the deep grooves left over from machining using a fine grit paste with polishing paper on a turntable (400–600 grit sandpaper mounted on a surface plate would also work), and then finishing the optical polish using white rouge buffing compound with a hard felt polishing wheel mounted on a lathe. The two halves of the mirror were tightly aligned with pins before polishing, so that we could take the mirror apart to insert the fibers and then reassemble the mirror exactly as before.

A.4 Conclusion

IntroSpec saw first light on March 17, 1999. Instrumental throughput easily matched expectations: our first ∼1-second exposure on Sirius saturated the CCD. Figure A.7 shows a few spectra taken with IntroSpec along with their exposure times. The instrument is now in regular use in Harvard astronomy courses for non-majors, who perform projects such as comparing the spectra of the two stars in Albireo. We have also used IntroSpec to demonstrate to students how a spectrograph works; the instrument's easy-to-remove top cover allows the students to peer directly inside. The potential for similar low-budget CCD spectrographs is only just beginning to be explored. Even under a bright urban sky, we have observed objects ranging from Main Sequence stars and planets to emission-line objects such as nebulae and stellar systems with variable accretion. We describe a number of fun astronomical spectroscopy projects, as well as how to reduce and analyze data from a CCD spectrograph, in another article (Kannappan & Fabricant, 2000a).

---

input are of no concern.

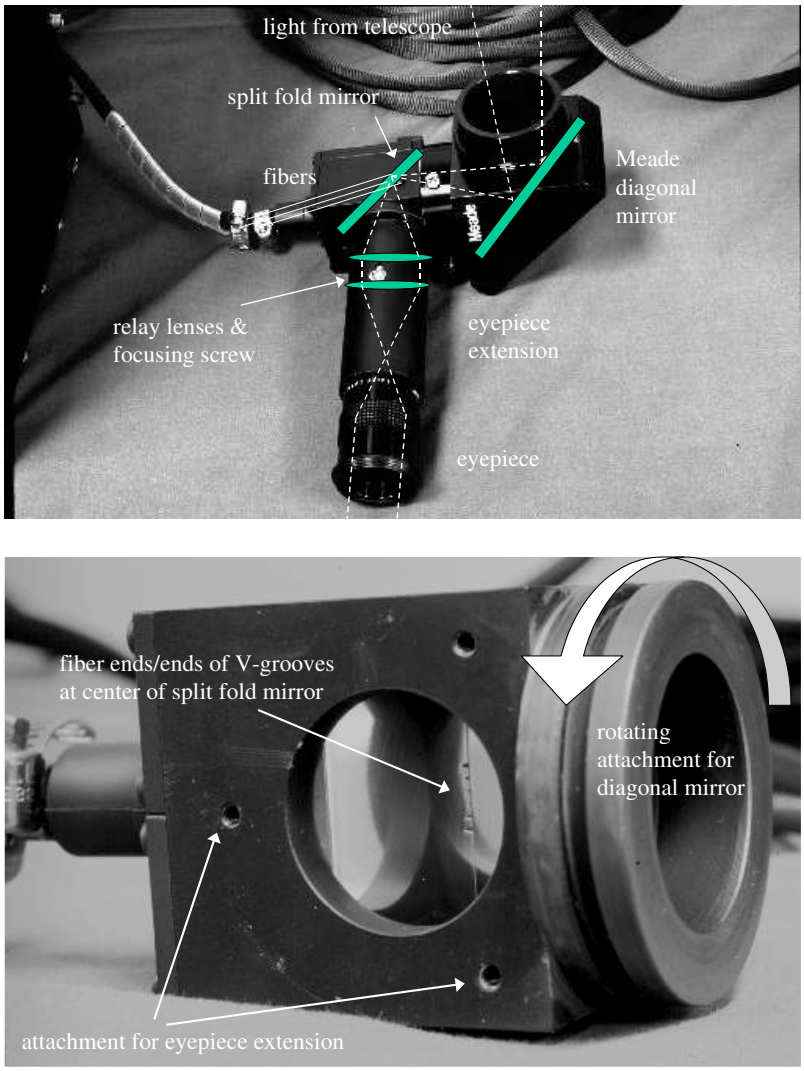

Figure A.6.— The guider/telescope attachment. *Upper Panel:* Lines drawn over the photo show the positions of the optical components and the path of the light. The small screw between the relay lenses allows them to slide forward or backward as a unit to focus. *Lower Panel:* Inner guider assembly, with the Meade diagonal mirror and the eyepiece extension removed to reveal the split mirror in the central piece. The fibers are not easily visible in the photo, but they protrude slightly from the V-grooves, with their polished surfaces flush to the focal plane of the telescope (i.e. at a 45° angle from the mirror surface).

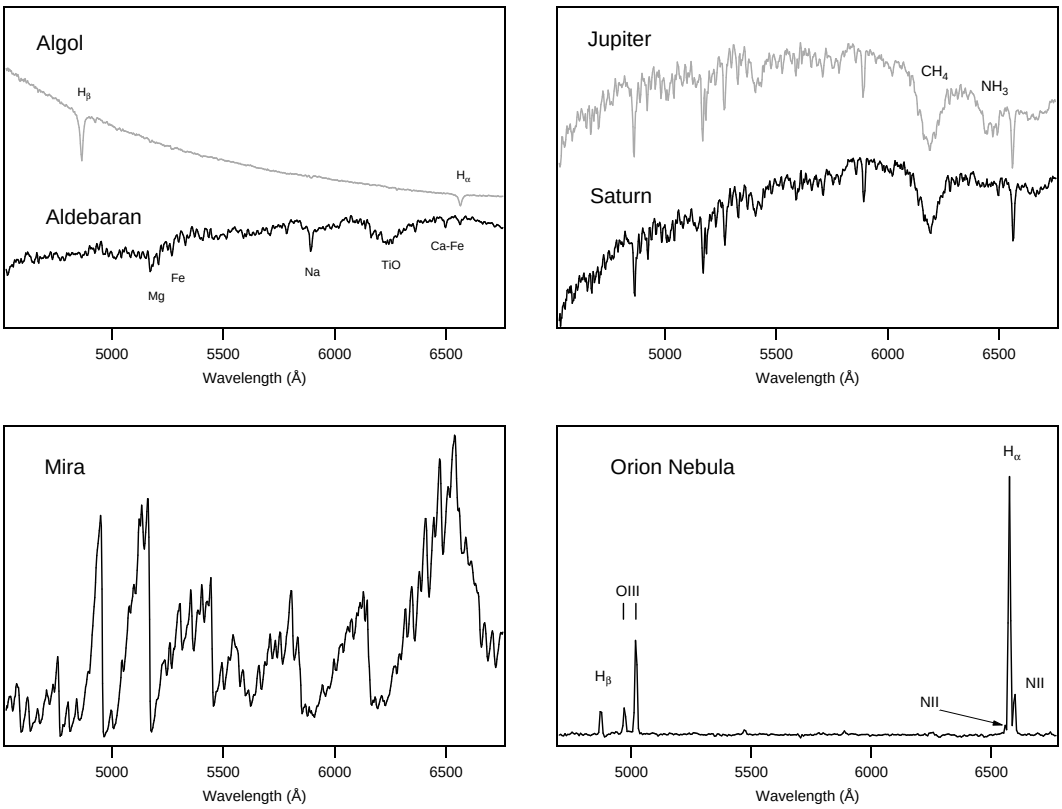

Figure A.7.— Spectra taken with IntroSpec at the Knowles Telescope. Approximate exposure times: Algol 30 sec; Aldebaran 3 sec; Jupiter 3 sec; Saturn 6 sec; Mira 30 sec; Orion Nebula 600 sec. Observations were taken on different nights with variable (but never photometric) sky conditions. All spectra except Orion were taken with the 100 μm fiber for maximum spectral resolution ($\sim$6 Å); for Orion we binned the CCD by two but still used the 100 μm fiber because of readout glitches in the 200 μm fiber spectrum. The resulting spectral resolution of $\sim$12 Å just suffices to distinguish the NII line at 6548 Å from Hα at 6563 Å. The sawtooth structure in Mira's spectrum is caused by absorption bands of TiO and other molecules in its outer envelope.

IntroSpec was designed and built at the Harvard-Smithsonian Center for Astrophysics, with financial support from Harvard College and the Harvard Astronomy Department arranged by Josh Grindlay and Ramesh Narayan. We thank Josh for his participation in planning and commissioning the instrument. The Knowles Telescope was generously given to Harvard by C. Harry and Janet Knowles. We are grateful to John Geary, Steve Amado, Joe Zajac, Douglas Mar, John Roll, Warren Brown, and Anita Bowles for advice, resources, and technical assistance during IntroSpec's construction phase. We also thank Tom Narita, John Raymond, Dimitar Sasselov, and all the students, friends, and family who helped with commissioning runs.

References

Aaronson, M., Huchra, J., Mould, J., Schechter, P. L., & Tully, R. B. 1982, ApJ, 258, 64

Abraham, R. G., Tanvir, N. R., Santiago, B. X., Ellis, R. S., Glazebrook, K., & van den Bergh, S. 1996, MNRAS, 279, L47

Arribas, S., Mediavilla, E., & Watson, F., eds. 1998, Fiber Optics in Astronomy III

Balzano, V. A. 1983, ApJ, 268, 602

Barden, S. C., ed. 1988, Fiber optics in astronomy; Proceedings of the Conference, Tucson, AZ, Apr. 11-14, 1988

Barton, E. J., Geller, M. J., Bromley, B. C., van Zee, L., & Kenyon, S. J. 2000a, in submitted

Barton, E. J., Geller, M. J., & Kenyon, S. J. 2000b, ApJ, 530, 660

Barton, E. J., Kannappan, S. J., Kurtz, M. J., & Geller, M. J. 2000c, PASP, 112, 367

Baugh, C. M., Cole, S., & Frenk, C. S. 1996, MNRAS, 283, 1361

Beers, T. C., Flynn, K., & Gebhardt, K. 1990, AJ, 100, 32

Bekki, K. 1998, ApJ, 502, L133

Bell, E. F. & de Jong, R. S. 2001, ApJ, 550, 212

Bershady, M. A. & Andersen, D. R. 2000, in ASP Conf. Ser. 197: Dynamics of Galaxies: from the Early Universe to the Present, 175

Bershady, M. A., Haynes, M. P., Giovanelli, R., & Andersen, D. R. 1999, in ASP Conf. Ser. 182: Galaxy Dynamics - A Rutgers Symposium, 499

Bertola, F., Buson, L. M., & Zeilinger, W. W. 1992, ApJ, 401, L79

Bettoni, D. 1989, AJ, 97, 79

Blitz, L., Spergel, D. N., Teuben, P. J., Hartmann, D., & Burton, W. B. 1999, ApJ, 514, 818

Bottinelli, L., Gouguenheim, L., Fouque, P., & Paturel, G. 1990, A&AS, 82, 391

Brocca, C., Bettoni, D., & Galletta, G. 1997, A&A, 326, 907

Buchalter, A., Jimenez, R., & Kamionkowski, M. 2001a, MNRAS, 322, 43

Buchalter, A., Jimenez, R., & Kamionkowski, M. 2001b, in astro-ph/0102025, submitted to MNRAS

Bureau, M., Mould, J. R., & Staveley-Smith, L. 1996, ApJ, 463, 60

Caldwell, N., Kirshner, R. P., & Richstone, D. O. 1986, ApJ, 305, 136

Caon, N., Macchetto, D., & Pastoriza, M. 2000, ApJS, 127, 39

Courteau, S. 1996, ApJS, 103, 363

—. 1997, AJ, 114, 2402

Courteau, S. . & Rix, H. 1999, ApJ, 513, 561

Cowie, L. L., Songaila, A., Hu, E. M., & Cohen, J. G. 1996, AJ, 112, 839

Davies, R. L., Burstein, D., Dressler, A., Faber, S. M., Lynden-Bell, D., Terlevich, R. J., & Wegner, G. 1987, ApJS, 64, 581

Doublier, V., Comte, G., Petrosian, A., Surace, C., & Turatto, M. 1997, A&AS, 124, 405

Dressler, A. 1980, ApJ, 236, 351

Eggen, O. J., Lynden-Bell, D., & Sandage, A. R. 1962, ApJ, 136, 748

Eisenstein, D. J. & Loeb, A. 1996, ApJ, 459, 432

Elizondo, D., Yepes, G., Kates, R., Müller, V., & Klypin, A. 1999, ApJ, 515, 525

Fabricant, D., Cheimets, P., Caldwell, N., & Geary, J. 1998, PASP, 110, 79

Falco, E. E., Kurtz, M. J., Geller, M. J., Huchra, J. P., Peters, J., Berlind, P., Mink, D. J., Tokarz, S. P., & Elwell, B. 1999, PASP, 111, 438

Forbes, D. A., Phillips, A. C., Koo, D. C., & Illingworth, G. D. 1996, ApJ, 462, 89

Franx, M. & de Zeeuw, T. 1992, ApJ, 392, L47

Franx, M., Illingworth, G., & Heckman, T. 1989, ApJ, 344, 613

Freeman, K. C. 1970, ApJ, 160, 811

Frei, Z. & Gunn, J. E. 1994, AJ, 108, 1476

Galletta, G. 1996, in ASP Conf. Ser. 91: IAU Colloq. 157: Barred Galaxies, 429

Garnier, R., Paturel, G., Petit, C., Marthinet, M. C., & Rousseau, J. 1996, A&AS, 117, 467

Giovanelli, R., Haynes, M. P., Herter, T., Vogt, N. P., da Costa, L. N., Freudling, W., Salzer, J. J., & Wegner, G. 1997a, AJ, 113, 53

Giovanelli, R., Haynes, M. P., Herter, T., Vogt, N. P., Wegner, G., Salzer, J. J., da Costa, L. N., & Freudling, W. 1997b, AJ, 113, 22

Giraud, E. 1986, A&A, 164, 17

Glumac, N. & Sivo, J. 1999, S&T, 97, 134

Gray, P. M., ed. 1993, Fiber Optics in Astronomy II

Grogin, N. A. & Geller, M. J. 1998, ApJ, 505, 506

Gunn, J. E. & Gott, J. R. I. 1972, ApJ, 176, 1

Han, M. & Mould, J. 1990, ApJ, 360, 448

Haynes, M. P., Giovanelli, R., Chamaraux, P., da Costa, L. N., Freudling, W., Salzer, J. J., & Wegner, G. 1999, AJ, 117, 2039

Haynes, M. P., Jore, K. P., Barrett, E. A., Broeils, A. H., & Murray, B. M. 2000, AJ, 120, 703

Haynes, M. P., van Zee, L., Hogg, D. E., Roberts, M. S., & Maddalena, R. J. 1998, AJ, 115, 62

Héraudeau, P. & Simien, F. 1998, A&AS, 133, 317

Héraudeau, P., Simien, F., Maubon, G., & Prugniel, P. 1999, A&AS, 136, 509

Hernquist, L. & Barnes, J. E. 1991, Nature, 354, 210

Huchra, J., Davis, M., Latham, D., & Tonry, J. 1983, ApJS, 52, 89

Hunter, D. A., Wilcots, E. M., van Woerden, H., Gallagher, J. S., & Kohle, S. 1998, ApJ, 495, L47

Isobe, T., Feigelson, E. D., Akritas, M. G., & Babu, G. J. 1990, ApJ, 364, 104

Jacoby, G. H., Branch, D., Clardullo, R., Davies, R. L., Harris, W. E., Pierce, M. J., Pritchet, C. J., Tonry, J. L., & Welch, D. L. 1992, PASP, 104, 599

Jansen, R. A. 2000, PhD thesis, Univ. Groningen, The Netherlands

Jansen, R. A., Fabricant, D., Franx, M., & Caldwell, N. 2000a, ApJS, 126, 331

Jansen, R. A., Franx, M., Fabricant, D., & Caldwell, N. 2000b, ApJS, 126, 271

Jore, K. P. 1997, PhD thesis, Cornell University

Jorgensen, I. 1994, PASP, 106, 967

Kamphuis, J. J., Sijbring, D., & van Albada, T. S. 1996, A&AS, 116, 15

Kannappan, S. & Fabricant, D. 2000a, S&T, 100, 125

Kannappan, S. J. & Fabricant, D. G. 2000b, in ASP Conf. Ser. 230: Galaxy Disks and Disk Galaxies, eds. J. G. Funes & E. M. Corsini, 449 (in press)

Kannappan, S. J. & Fabricant, D. G. 2001a, AJ, 121, 140

Kannappan, S. J. & Fabricant, D. G. 2001b, in ASP Conf. Ser. 230: Galaxy Disks and Disk Galaxies, eds. J. G. Funes & E. M. Corsini, 447 (in press)

Kannappan, S. J., Fabricant, D. G., & Franx, M. 2001a, in preparation

Kannappan, S. J., Fabricant, D. G., & Franx, M. 2001b, in preparation

Kannappan, S. J., Fabricant, D. G., Franx, M., Berlind, P., Balog, Z., Carter, B., Hough, L. E., Lepore, N., & Weinberg-Wolf, J. 2001c, in preparation

Kennicutt, R. C., J. 1998, ARA&A, 36, 189

Kennicutt, R. C., J., Tamblyn, P., & Congdon, C. E. 1994, ApJ, 435, 22

Knapp, G. R. & Raimond, E. 1984, A&A, 138, 77

Kodaira, K. & Watanabe, M. 1988, AJ, 96, 1593

Kraan-Korteweg, R. C., Sandage, A., & Tammann, G. A. 1984, ApJ, 283, 24

Kuijken, K., Fisher, D., & Merrifield, M. R. 1996, MNRAS, 283, 543

Kurtz, M. J., Mink, D. J., Wyatt, W. F., Fabricant, D. G., Torres, G., Kriss, G. A., & Tonry, J. L. 1992, in ASP Conf. Ser. 25: Astronomical Data Analysis Software and Systems I, Vol. 1, 432

Kuznetsov, O. A., Lovelace, R. V. E., Romanova, M. M., & Chechetkin, V. M. 1999, ApJ, 514, 691

Lacey, C. & Cole, S. 1993, MNRAS, 262, 627

Lin, C. C. & Shu, F. H. 1964, ApJ, 140, 646

Lovelace, R. V. E. & Chou, T. 1996, ApJ, 468, L25

Lynden-Bell, D. 1967, MNRAS, 136, 101

Marzke, R. O., Huchra, J. P., & Geller, M. J. 1994, ApJ, 428, 43

Mathewson, D. S., Ford, V. L., & Buchhorn, M. 1992, ApJS, 81, 413

Matthews, L. D., van Driel, W., & Gallagher, J. S. 1998, AJ, 116, 2196

McGaugh, S. S., Schombert, J. M., Bothun, G. D., & de Blok, W. J. G. 2000, ApJ, 533, L99

Mihos, C. 2001, in ASP Conf. Ser. 230: Galaxy Disks and Disk Galaxies, eds. J. G. Funes & E. M. Corsini (in press)

Mihos, J. C. & Hernquist, L. 1994, ApJ, 431, L9

—. 1996, ApJ, 464, 641

Mirabel, I. F., Dottori, H., & Lutz, D. 1992, A&A, 256, L19

Mo, H. J., McGaugh, S. S., & Bothun, G. D. 1994, MNRAS, 267, 129

Moore, B., Lake, G., & Katz, N. 1998, ApJ, 495, 139

Morse, J. A., Cecil, G., Wilson, A. S., & Tsvetanov, Z. I. 1998, ApJ, 505, 159

Naab, T., Burkert, A., & Hernquist, L. 1999, ApJ, 523, L133

Neistein, E., Maoz, D., Rix, H., & Tonry, J. L. 1999, AJ, 117, 2666

Nilson, P. 1973, Uppsala general catalogue of galaxies (Uppsala: Astronomiska Observatorium, 1973)

O'Neil, K., Bothun, G. D., & Schombert, J. 2000, AJ, 119, 136

Patton, D. R., Pritchet, C. J., Yee, H. K. C., Ellingson, E., & Carlberg, R. G. 1997, ApJ, 475, 29

Pfenniger, D. & Norman, C. 1990, ApJ, 363, 391

Pierce, M. J. & Tully, R. B. 1992, ApJ, 387, 47

Pierini, D. 1999, A&A, 352, 49

Pierini, D. & Tuffs, R. J. 1999, A&A, 343, 751

Prugniel, P., Zasov, A., Busarello, G., & Simien, F. 1998, A&AS, 127, 117

Pustilnik, S. A., Kniazev, A. Y., Lipovetsky, V. A., & Ugryumov, A. V. 2001, in A&A, accepted

Raychaudhury, S., von Braun, K., Bernstein, G. M., & Guhathakurta, P. 1997, AJ, 113, 2046

Rix, H., Guhathakurta, P., Colless, M., & Ing, K. 1997, MNRAS, 285, 779

Rix, H. W., Carollo, C. M., & Freeman, K. 1999, ApJ, 513, L25

Roberts, M. S. 1978, AJ, 83, 1026

Rubin, V. C. 1994, AJ, 108, 456

Rubin, V. C., Burstein, D., Ford, W. K., & Thonnard, N. 1985, ApJ, 289, 81

Rubin, V. C., Waterman, A. H., & Kenney, J. D. P. 1999, AJ, 118, 236

Sakai, S., Mould, J. R., Hughes, S. M. G., Huchra, J. P., Macri, L. M., Kennicutt, R. C., Gibson, B. K., Ferrarese, L., Freedman, W. L., Han, M., Ford, H. C., Graham, J. A., Illingworth, G. D., Kelson, D. D., Madore, B. F., Sebo, K., Silbermann, N. A., & Stetson, P. B. 2000, ApJ, 529, 698

Sandage, A., Binggeli, B., & Tammann, G. A. 1985, AJ, 90, 1759

Schechter, P. L. 1980, AJ, 85, 801

Schombert, J. M., Pildis, R. A., Eder, J., & Oemler, A., J. 1995, AJ, 110, 2067

Schroeder, D. J. 2000, Astronomical Optics (San Diego, Academic Press, 2000, 478 p.)

Schweizer, F. 1998, in Galaxies: Interactions and Induced Star Formation, Saas-Fee Advanced Course 26, 105

Schweizer, F. & Seitzer, P. 1992, AJ, 104, 1039

Scodeggio, M., Giovanelli, R., & Haynes, M. P. 1998, AJ, 116, 2738

Simard, L. & Pritchet, C. J. 1998, ApJ, 505, 96

—. 1999, PASP, 111, 453

Stil, J. M. & Israel, F. P. 1998, in astro-ph/9810151

Strauss, M. A. & Willick, J. A. 1995, Phys. Rep., 261, 271

Taylor, C. L., Thomas, D. L., Brinks, E., & Skillman, E. D. 1996, ApJS, 107, 143

Thakar, A. R., Ryden, B. S., Jore, K. P., & Broeils, A. H. 1997, ApJ, 479, 702

Theureau, G., Bottinelli, L., Coudreau-Durand, N., Gouguenheim, L., Hallet, N., Loulergue, M., Paturel, G., & Teerikorpi, P. 1998, A&AS, 130, 333

Toomre, A. & Toomre, J. 1972, ApJ, 178, 623

Trentham, N., Tully, R. B., & Verheijen, M. A. W. 2001, in MNRAS, in press

Tully, R. B. 1988, Nearby galaxies catalog (Cambridge and New York, Cambridge University Press)

Tully, R. B. & Fisher, J. R. 1977, A&A, 54, 661

Tully, R. B. & Fouque, P. 1985, ApJS, 58, 67

Tully, R. B. & Pierce, M. J. 2000, ApJ, 533, 744

Tully, R. B., Pierce, M. J., Huang, J., Saunders, W., Verheijen, M. A. W., & Witchalls, P. L. 1998, AJ, 115, 2264

Tully, R. B., Shaya, E. J., & Pierce, M. J. 1992, ApJS, 80, 479

Tully, R. B., Verheijen, M. A. W., Pierce, M. J., Huang, J., & Wainscoat, R. J. 1996, AJ, 112, 2471

Tutui, Y. & Sofue, Y. 1997, A&A, 326, 915

Vader, J. P. & Vigroux, L. 1991, A&A, 246, 32

van Dokkum, P. G. & Franx, M. 1996, MNRAS, 281, 985

Verheijen, M. A. W. 1997, PhD thesis, Univ. Groningen, The Netherlands

Verheijen, M. A. W. & Sancisi, R. 2001, in A&A, accepted

Vogt, N. P., Forbes, D. A., Phillips, A. C., Gronwall, C., Faber, S. M., Illingworth, G. D., & Koo, D. C. 1996, ApJ, 465, L15

Vogt, N. P., Phillips, A. C., Faber, S. M., Gallego, J., Gronwall, C., Guzman, R., Illingworth, G. D., Koo, D. C., & Lowenthal, J. D. 1997, ApJ, 479, L121

Whitmore, B. C., Kirshner, R. P., & Schechter, P. L. 1979, ApJ, 234, 68

Whitmore, B. C., Lucas, R. A., McElroy, D. B., Steiman-Cameron, T. Y., Sackett, P. D., & Olling, R. P. 1990, AJ, 100, 1489

Willick, J. A. 1994, ApJS, 92, 1

Willick, J. A., Courteau, S., Faber, S. M., Burstein, D., Dekel, A., & Kolatt, T. 1996, ApJ, 457, 460

Worthey, G. & Ottaviani, D. L. 1997, ApJS, 111, 377

Wyse, R. F. G. & Silk, J. 1985, ApJ, 296, L1

Yasuda, N., Fukugita, M., & Okamura, S. 1997, ApJS, 108, 417

Zaritsky, D. & Rix, H. 1997, ApJ, 477, 118

Zwaan, M. A. & Briggs, F. H. 2000, ApJ, 530, L61